INSTITUTO SUPERIOR DE ENGENHARIA DO PORTO
MESTRADO EM ENGENHARIA BIOMÉDICA



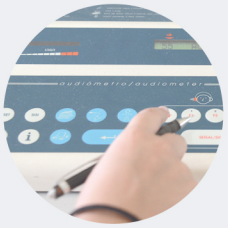


Development of computational techniques to explicitly simulate angiogenesis

TOMÁS ALMEIDA DE SOUSA
Julho de 2021

P.PORTO

Development of computational techniques to explicitly simulate angiogenesis

Tomás Almeida de Sousa

Engenheiro Biomédico pelo Instituto Superior de Engenharia do Porto

"Dissertação apresentada no Instituto Superior de Engenharia do Porto para a obtenção de grau de Mestre em Engenharia Biomédica"

Orientador: Professor Doutor Jorge Américo de Oliveira Pinto Belinha
Coorientador: Professora Ana Catarina Couto Soares Guerra

[julho de 2021]

Agradecimentos

Primeiramente, gostaria de agradecer ao Professor Doutor Jorge Belinha por toda a disponibilidade e ajuda prestada durante a elaboração desta dissertação e, especialmente, por me receber em todas as reuniões com um sorriso.

Em segundo lugar, gostaria de agradecer à Professora Ana Guerra por todo o acompanhamento feito e pela rapidez e qualidade com que respondeu a todas as minhas dúvidas.

Ao meu pai e à minha mãe, por me proporcionarem as melhores condições para os meus estudos e por sempre me motivarem a seguir os meus sonhos e dar o meu melhor.

À minha irmã Inês por todo o interesse que demonstrou pela minha dissertação e a vontade que tem de me ver a completá-la.

Ao meu irmão Duarte por ter feito as minhas tarefas domésticas enquanto eu trabalhava na dissertação.

À minha irmã Eva por compreender que eu não podia jogar futebol com ela porque estava a fazer um trabalho grande.

À minha Ana por toda a motivação, suporte, presença constante, aconselhamento e por ouvir sempre os meus desabafos durante as alturas mais difíceis.

Aos meus AMIGOS Alexandre, Miguel e Tiago pelo apoio, motivação e momentos de lazer que me proporcionaram.

Finalmente, à minha querida avó Gina, que há 20 anos atrás estava a redigir a sua tese de mestrado e não tinha tempo para brincar comigo aos dinossauros. Este ano foi a minha vez. Obrigado por sempre me inspirares para ser uma pessoa melhor e por me motivares a prosseguir sempre com os meus estudos.

Obrigado a todos por terem tornado este percurso possível. Sem vocês, não teria conseguido.

Resumo

A angiogénese é o processo pelo qual os novos capilares são formados a partir da vasculatura pré-existente e é um evento fulcral na cicatrização de feridas e no crescimento de tumores. Compreender os mecanismos pelos quais a angiogénese é regulada é fundamental para desenvolver novas terapias para tumores ou feridas crónicas. Os biomateriais são candidatos a ser utilizados em futuras terapias que envolvam tanto inibição como indução da angiogénese. Contudo, estudar *in vivo* os efeitos dos biomateriais na angiogénese é financeiramente dispendioso e existem várias variáveis que são difíceis de controlar. O desenvolvimento de modelos *in silico* surge como uma opção para testar hipóteses num ambiente completamente manipulável que proporciona resultados comparáveis com estudos experimentais.

Neste trabalho um método numérico 2D que simula a angiogénese é proposto. O modelo computacional considera que as células endoteliais migram de acordo com uma equação de reação-difusão que governa o fator de crescimento endotelial vascular (VEGF) e utiliza um método sem malha para resolver as equações que o governam. Um ensaio de angiogénese *in vivo* foi utilizado para obter redes capilares comparáveis às obtidas pelo modelo. Os efeitos na angiogénese da difusão constante e variável de VEGF por parte de um biomaterial foram estudados.

Verificou-se a migração de células endoteliais na direção da maior concentração de VEGF e a obtenção de redes capilares realistas. A uma difusão constante, quão maior a concentração de VEGF no biomaterial mais rápido as células endoteliais começavam a migrar na sua direção e a penetrá-lo. A uma difusão variável, a penetração do biomaterial por parte dos capilares ocorreu em concentrações mais elevadas de VEGF em comparação com resultados obtidos para uma concentração constante.

O modelo apresentou bons resultados de acordo com a literatura e foi validado com sucesso recorrendo ao ensaio *in vivo*. Contudo, os resultados referentes às simulações com o biomaterial ainda requerem validação experimental.

Palavras-Chave: angiogénese; modelos computacionais; modelo discreto; RPIM; angiogénese em feridas; biomateriais; ensaio *in vivo*.

Abstract

Angiogenesis is the process by which new capillaries are formed from pre-existent vasculature and it is a crucial event in wound healing and tumorous growth. Understanding the mechanisms by which angiogenesis is regulated is pivotal to develop new cancer and wound healing therapies. Biomaterials are strong candidates for future therapies involving the inhibition or induction of angiogenesis. Nevertheless, the *in vivo* study of the biomaterial's effects in the angiogenic process are financially expensive and present many variables that are hard to control. The development of *in silico* models arises as an option to test hypothesis in a completely manipulative environment that presents results comparable with experimental studies.

In this work, a 2D numerical method that simulates sprouting angiogenesis is proposed. The model considers that endothelial cells migrate according to a diffusion-reaction equation that governs the Vascular Endothelial Growth Factor (VEGF) and makes use of a meshless method to solve its governing equations. The chick chorioallantoic membrane (CAM) assay was used to obtain capillary networks that will be compared to the *in silico* obtained networks. The angiogenic effects of constant and variable VEGF diffusion by a biomaterial were studied.

Endothelial cell migration towards the highest VEGF concentration was verified and realistic capillary networks were obtained. At a constant VEGF diffusion, the higher the VEGF concentration in the biomaterial the earlier the endothelial cells started to migrate towards it and penetrating it. To a variable diffusion rate, the biomaterial penetration occurred at higher VEGF concentrations when compared to the results obtained for a constant VEGF diffusion rate.

The developed model presented good results in accordance with the literature. The modelled angiogenesis in response to a wound was validated using the CAM. However, the biomaterial simulations still require experimental validation.

Key words: angiogenesis; computational modelling; discrete model; RPIM; wound healing angiogenesis; biomaterials; CAM assay.

Index

Figures List

Tables List

List of Abbreviations

CAM – Chick Chorioallantoic Membrane

ECM – Extracellular Matrix

EGF – Epidermal Growth Factor

FEM – Finite Element Method

HBOT – Hyperbaric Oxygen Therapy

MQ-RBF– Multiquadrics Radial Basis Function

ODE Ordinary Differential Equation

PDEs – Partial Differential Equations

PDGF – Platelet-Derived Growth Factor

RBC – Red Blood Cells

RPI – Radial Point Interpolators

RPIM – Radial Point Interpolation Method

TAF – Tumour Angiogenesis Factor

TE – Tissue Engineering

VEGF – Vascular Endothelial Growth Factor

VEGFR – Vascular Endothelial Growth Factor Receptor

WBC – White Blood Cells

CHAPTER 1 – INTRODUCTION

1. Introduction

Angiogenesis is the formation of new blood vessels from pre-existing ones (W. Risau, 1997). This process is a central mechanism to tissue maintenance, being essential during wound healing and tumour growth. According to the World Health Organization (WHO) cancer is the second leading cause of death globally causing approximately 9.6 million deaths in 2018 and accounting for billions of dollars in health care. Regarding chronic skin wounds, the economic and social impact is very significant. In the United States of America alone, the estimated spending for all wound types is between 28.1 to 96.8 billion American dollars per year (Nussbaum et al., 2018). Completely understanding the mechanisms that regulate angiogenesis, physiologically and pathologically, is essential for the development of new and effective therapies. One of the most popular *in vivo* angiogenesis models is the chick chorioallantoic membrane (CAM) assay. The CAM is an extraembryonic membrane that is highly and densely vascularized and has an easy to access location in the egg (Mangir et al., 2019). The CAM assay is simple and fast at producing results but arguably, its best feature is that allows for an easy visual inspection of data. These models are also extremely useful to study the effects of biomaterials in angiogenesis (Ribatti et al., 2020). As the development of many *in vitro* and *in vivo* angiogenic models helped to understand this phenomenon (Auerbach et al., 2003; Mangir et al., 2019; Nasevicius et al., 2000; Staton et al., 2004; Watari et al., 2020) it is not yet fully understood. Furthermore, developing such models is expensive and due to the complexity of the angiogenic process it is hard to assess the behaviour of individual factors. These limitations make computational models an appealing solution to study angiogenesis.

In silico models can simulate biological angiogenic environment and are a powerful predictive tool in systems biology (Peirce, 2008). Computational models offer the possibility of controlling the interactions and behaviours between the different system's components providing an immense array of hypothesis to be tested. Regarding wound healing angiogenesis, there are three major modelling approaches: continuous or continuum approaches, which are indicated for tissue level studies; discrete approaches, more indicated for when the intention is to track individual cell behaviour and finally hybrid approaches, which combine the benefits from the previous methods. Correctly constructed models serve as an important complement to experimental studies and as a

tool for developing and testing new and effective therapies using a biomaterial driven approach to treat chronic/ischemic wounds. In the literature, many models are capable of simulating angiogenesis at diverse scales and using different approaches (Bauer et al., 2007; Bookholt et al., 2016; Gaffney et al., 2002; Scianna, 2015; Xue et al., 2009), however, there is a lack of models that are directly resultant from comparison with *in vivo* methodologies. Furthermore, regarding the usage of advanced discretization methods, the finite element method (FEM) is the most common choice. However, using meshless methods such as the radial point interpolation method (RPIM) in biological simulations has been proven advantageous over mesh-bound methods (Belinha, 2014). For instance, meshless methods allow to study complex geometries, locally insert nodes and therefore enabling local accurate solutions without compromising in computational cost and are effective at dealing with mesh distortion. Taking these aspects into consideration, this work proposes an innovative wound-healing angiogenesis model dependent on the vascular endothelial growth factor (VEGF) chemoattractant properties that can be used to study the angiogenic response to biomaterials.

1.1. Objectives

This work aims to enhance a new biological model to predict sprouting angiogenesis and to understand the influence of different factors such as, wound geometry and chemical concentration in the angiogenic process. It also aims to test the model by varying different parameters assessing its robustness and validate it by direct comparison to the CAM images.

1.2. Document Structure

The presented document is divided into seven chapters. The current chapter serves as a brief introduction to the topic of analysis while also mentioning the relevance of the study and its objectives. In chapter 2 a description of the cardiovascular system from the macro to the microscale will be made. The mechanisms behind angiogenesis and its role on tissue regeneration and tumorous growth are presented. Also, biomaterial driven therapies to inhibit/induce angiogenesis are covered. Chapter 3 focuses on mathematical and computational modelling of angiogenesis and the state-of-the-art of the different models that are used to model angiogenesis, with special focus on wound-healing models. In chapter 4 the numerical method used in this work is formalized and the proposed model is described. Chapter 5 presents the preliminary tests made to the model in order to assess

its quality. Chapter 6 regards the effects of a VEGF releasing biomaterial at a constant and/or variable rate in the capillary network morphology. Finally, chapter 7 contains the conclusions of the work along with reference to the model's current limitations and future improvements.

CHAPTER 2 – CARDIOVASCULAR SYSTEM AND ANGIOGENESIS

2. Cardiovascular System and Angiogenesis

In this section of the dissertation, the cardiovascular system will be anatomically described from the macroscale to the microscale and each of its component's functions will also be addressed. The angiogenic phenomena will be analysed and its mechanisms will be thoroughly explained. A brief state-of-the-art regarding biomaterials and angiogenesis composes the end of chapter 2.

2.1. The Cardiovascular System

The first organ system to be formed in the embryo phase is the cardiovascular system along with the heart being the first functional organ (Dabbagh et al., 2017; Hescheler et al., 1999). The cardiovascular system is formed by the heart, blood vessels and the blood itself. This system is responsible for providing oxygen and nutrients to the tissues, while also accounting for the transportation of several hormones and dispose of metabolic wastes. The transportation of such essential substances is carried by the blood.

Blood is essential to life and the average human has more than 5 litres of blood in their body. The whole composition of this fluid is a mixture of different elements, namely cells, colloids, and crystalloids. There are four different blood components, each with a different role (Basu & Kulkarni, 2014). Plasma is a yellowish fluid that is majorly composed by water, but it also contains other components such as proteins and sugars. Averagely, plasma accounts for 55% of the blood's composition, which guarantees it a liquid/fluidic form. Being the liquid base of the blood, several of the plasma's functions coincide with general blood functions. These include regulation of acid-base balance and body temperature, transportation of nutrients, respiratory gases, hormones and antibodies, amongst others (Mathew & Bhimji, 2018). Platelets (thrombocytes) are discoid anucleate cells that primarily act as haemostasis regulators and vascular integrity managers (Ghoshal & Bhattacharyya, 2014; N. Thon & E. Italiano, 2012). Such cells are the smallest blood cells with 2-3μm in diameter and, on average, a human adult contains a trillion in its bloodstream (N. Thon & E. Italiano, 2012). These anucleate cells are formed by megakaryocytes who originate and mature in the bone marrow (Ghoshal & Bhattacharyya, 2014; Tober et al., 2007). Platelets are usually in an inactive state, activating when a blood vessel is damaged to initiate the clotting process.

Oxygen and carbon dioxide are constantly in circulation in the bloodstream. The circulatory transport of these gases is carried on by the red blood cells (RBCs) or erythrocytes. RBCs are anucleate, biconcave shaped cells whose physiological role is to transport oxygen from the lungs to the remaining tissues and maintain acid/base equilibrium (Kuhn et al., 2017). Erythrocytes are the most abundant cell in the human body (Ballas, 1987), the densest component of the blood with measurements of 7.6-8.7 μm of diameter and 1.7-2.2 μm in thickness (Diez-Silva et al., 2010) and develop in the bone marrow. The cytoplasm of these cells is rich in haemoglobin, an oxygen-binding biomolecule so abundant that accounts for almost the total dry weight of the erythrocyte. Haemoglobin is a tetramer formed by four polypeptide globin chains that contain a central iron ion in the ferrous state which allows for the binding of oxygen (Farid & Lecat, 2019). The iron ion present in this molecule is what gives the blood its red colour.

White blood cells (WBCs) or leukocytes are nucleated cells that play a crucial role in immunity and defence against infections. Although being actively found in the bloodstream, they are not limited to it since they can migrate into tissues via diapedesis (Tigner et al., 2020). The WBCs migrations occur to infection or injury sites. There are different varieties of leukocyte that differentiate in the bone marrow, and every variety has a specific role and function in the immune system (Blumenreich, 1990; Mank & Brown, 2020; Tigner et al., 2020). For instance, neutrophilic granulocytes are phagocytes with the ability to ingest particles larger than 0.5 μm (Rosales & Uribe-Querol, 2017). Basophils play a crucial role in inflammatory reactions but are not usually capable of performing phagocytosis (Siracusa et al., 2013).

The heart is a muscular organ that acts like a pump and makes the blood circulate throughout the body allowing for a reliable delivery of oxygen and nutrients to every cell in the body (Drake et al., 2019; Katz, 2011). Anatomically, the human heart is located between the lungs in the thoracic cavity behind the sternum and above the diaphragm, while being positioned slightly left to the centre of the chest. The heart is divided into four different cavities: two upper chambers, the atriums and two lower chambers, the ventricles. These chambers are separated from each other by the atrioventricular valves (Katz, 2011). The septum divides the heart into left and right side. The right side of the heart is responsible for receiving venous blood from the body and pumping it to the lungs while the left side receives the oxygenated blood from the lungs and pumps it into the rest of the body (Drake et al., 2019). Pulmonary circulation is the movement of the venous

blood from the heart to the lungs, for oxygenation, and then back to the heart (Drake et al., 2019; Katz, 2011; Matienzo & Bordoni, 2020). Systemic circulation on the other hand consists in the movement of oxygenated blood from the heart to the body and then back to the heart in a deoxygenated state. Regarding pressure, the systemic circulation has considerably higher values than the pulmonary circulation (Feher, 2012) since in the latter blood needs to reach the lungs while in the former blood needs to be pumped to the rest of the body. To handle such pressure, the left ventricle walls are three times thicker than the right one (Feher, 2012), also, thick blood vessels such as the aorta are necessary.

The aorta is the largest blood vessel in the human body and it transports oxygenated blood across the body (Komutrattananont et al., 2019). Blood vessels that carry blood away from the heart, oxygenated blood, are denominated arteries. There are three different types of arteries that differ in smooth muscle and elastic fibres which contributes to the overall size, thickness and function of the vessel (Drake et al., 2019). Arteries can be large and elastic, medium and muscular, and small, which are also named arterioles. Veins are another type of blood vessel that, contrarily to arteries, transport blood towards the heart, the venous blood. Veins, as well as arteries, are subdivided into three different classes: large, medium and small (Drake et al., 2019). The exchange of oxygen, nutrients and waste in the tissues is carried by the capillaries. Capillaries are the smallest of the blood vessels, have the largest surface area and connect the arteries and veins (Matienzo & Bordoni, 2020). These blood vessels' walls consist only in one layer of endothelial cells, a basal lamina and a few scattered pericytes (Alberts et al., 2002). Pericytes are wrapped around the endothelial cells aiding in vessel stabilization and regulation of blood flow (Alberts et al., 2002; Pallone & Silldorff, 2001). Being only one cell thick optimizes the exchanges between tissues and the capillaries (Lever, 2005). The tissues' oxygenation can increase with more capillaries and contrarily less capillaries can cause hypoxia or anoxia, so, regeneration/formation of these blood vessels is vital (Adair & Montani, 2010)

2.2. Angiogenesis and its Mechanisms

Angiogenesis is the formation of new blood vessels from pre-existing ones and it is the process by which new capillaries are formed (Adair & Montani, 2010; Bikfalvi, 2004; W. Risau, 1997; Santulli, 2013; Shi et al., 2017). Contrarily to angiogenesis, the formation of new blood vessels is called vasculogenesis (Werner Risau & Flamme, 1995).

Vasculogenesis is defined as the differentiation of angioblasts into endothelial cells by which the embryo forms the primitive blood vessels (W. Risau, 1997). Contrarily to angiogenesis, that occurs throughout life, vasculogenesis only occurs during the embryo state. In healthy tissues angiogenesis can take place through two different events, endothelial sprouting or intussusception (non-sprouting) (Carmeliet, 2000). The term angiogenesis was coined by Dr. John Hunter in 1787 (Hall, 2005) however, only in 1977 sprouting angiogenesis in a tumour was described. Ausprunk & Folkman (1977) studied a carcinoma in a rabbit cornea concluding that the mechanisms behind capillaries proliferation were the same either in tumours or wound healing. The observed sprouting phenomena comprised several events such as the migration of endothelial cells beyond their parent vessel, vascular leakage of colloidal carbon particles, weakening of interendothelial contacts and recruitment of pericytes (Ausprunk & Folkman, 1977).

Sprouting angiogenesis (Figure 2.1) has been extensively studied thus, is much better documented and understood than the intussusceptive process. Intussusceptive angiogenesis consists in a splitting process where an intraluminal pillar is formed by the invagination of the capillary walls into the vascular lumen (Adair & Montani, 2010; Djonov et al., 2003) and it was discovered in 1986 by Caduff and Burri (Caduff et al., 1986). This type of angiogenesis is faster and more efficient when compared to sprouting, however, its functioning mechanism is still poorly understood (Saravanan et al., 2020). Therefore, in this work only the sprouting phenomena is addressed.

Regarding sprouting, the development of multiple *in vivo* and *in vitro* models of angiogenesis have been crucial to the scientific advance in this area. *In vitro* models focus predominantly in the study of endothelial cell behaviour in a controlled environment. Endothelial cells migration, proliferation and tube formation are the main focus of such assays (Auerbach et al., 2003; Staton et al., 2004). *In vivo* assays, on the other hand, aid in the comprehension of the grand scheme of things because they involve several kinds of cells, not only endothelial, and mimic the angiogenic process. *In vivo* models include the CAM assay (Mangir et al., 2019; Naik et al., 2018; Ribatti et al., 2020), the zebrafish model (Childs et al., 2002; Nasevicius et al., 2000; Serbedzija et al., 1999; Tal et al., 2017), corneal assays (Ausprunk & Folkman, 1977; Fournier et al., 1981) and dorsal air sac model (Watari et al., 2020; Yonekura et al., 1999).

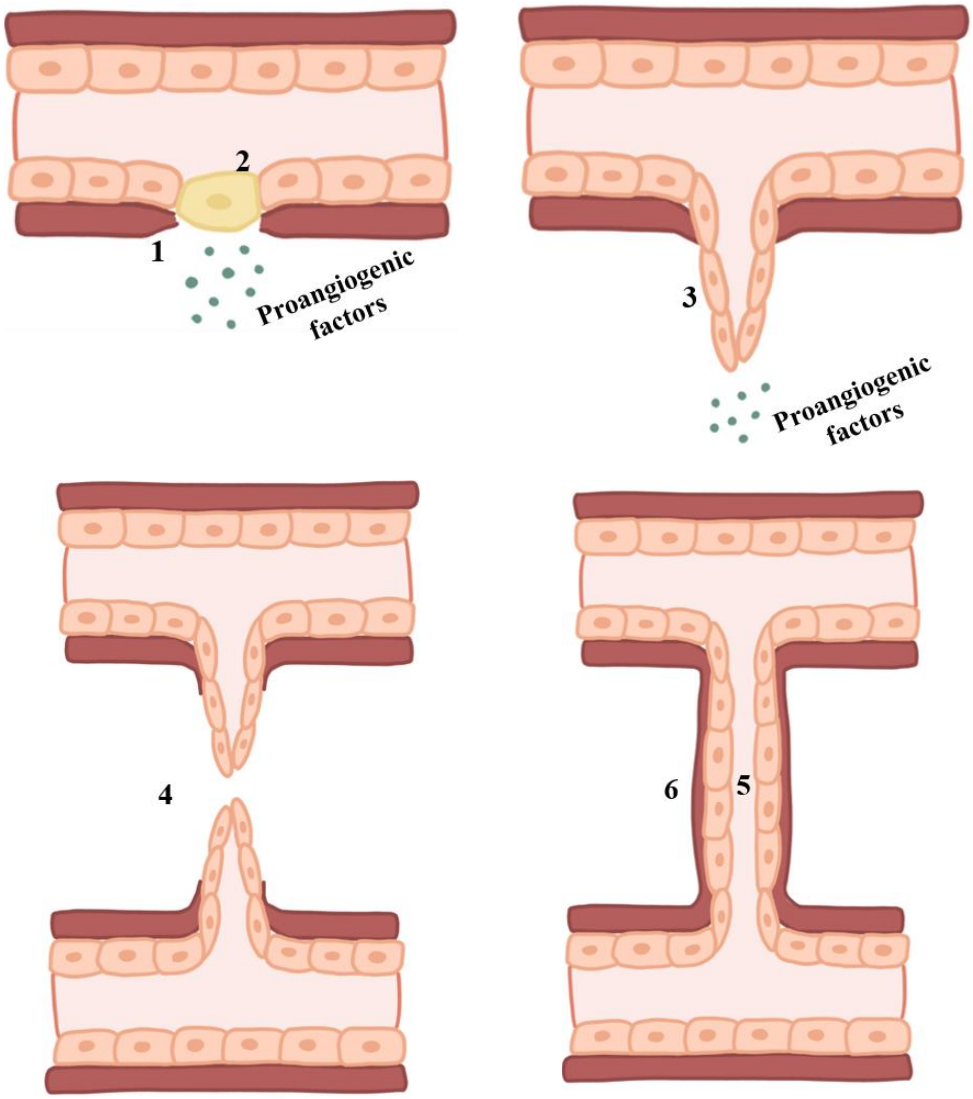

Figure 2.1- Schematic representation of sprouting angiogenesis. Upon the presence of pro-angiogenic factors, the proteolysis of the basement membrane occurs (1) and tip cells start to form (2). The stalk cells then follow the tip cell, proliferating and migrating towards the angiogenic stimulus elongating the capillary sprout (3). Neighbouring sprout vessels aim to fuse with the sprouting vessels (4). Then anastomosis occurs, allowing the re-establishment of the blood flow (5) and the basement membrane restores forming a new, stable vessel (6).

Blood vessels are usually in an equilibrium state where cell division does not occur, the quiescence state. Upon wounding, ischemia, or tumorous cells presence, angiogenic signals, such as the vascular endothelial growth factor (VEGF), are released. In response to those signals, the pericytes in the basement membrane start to detach, which causes its degradation (Carmeliet & Jain, 2011; Chang et al., 2009). The blood vessels become hyperpermeable to plasma proteins, which consequently will cause the extravasation of fibrinogen, amongst others, and the formation of a temporary extracellular matrix (ECM) rich in fibrin (Carmeliet & Jain, 2011; Sundberg et al., 2001). Endothelial cells then start to migrate onto the newly formed temporary matrix, the

sprouting. The sprouting is mainly controlled by VEGF, who stimulates the induction of tip cells. Tip cells are specialized endothelial cells located at the tips of the vascular sprouts (Gerhardt et al., 2003). These cells migrate towards the angiogenic stimulus (VEGF) leading the stalk cells (Carmeliet & Jain, 2011; Gerhardt et al., 2003; Ribatti & Crivellato, 2012). Stalk cells are cells that trail the tip cell. Contrarily to tip cells, whose nature is migratory, stalk cells proliferate and elongate the vascular sprout (Carmeliet & Jain, 2011; Gerhardt et al., 2003). The proliferation of these cells depends on the concentration of VEGF. Posteriorly, sprouts will extend until they meet so they can anastomose, thus forming the lumen and re-establishing the blood flow. The newly formed vessels will return to a quiescent state with firm junctions, a basement membrane and matured pericytes (Carmeliet & Jain, 2011). Angiogenesis is tightly regulated by several genetic factors and intracellular signalling pathways. Furthermore, diverse mechanical forces, extracellular matrices and cell-to-cell interactions also heavily modulate angiogenic behaviour (Shiu et al., 2005). The VEGF family, however, stands out as the best studied regulator of angiogenesis.

Mammalian genomes only bear 5 genes of the VEGF family, VEGF-A, VEGF-B, VEGF-C, VEGF-D and the placental growth factor (Shibuya, 2011). VEGF-C, VEGF-D and its receptor VEGFR-3 play a major role in regulating lymphangiogenesis (Alitalo & Carmeliet, 2011), on the other hand, angiogenesis is mainly regulated by VEGF-A and its tyrosine kinase receptors VEGFR-1 and VEGFR-2 (Carmeliet & Jain, 2011; Ribatti & Crivellato, 2012; Shibuya, 2011). FLT4, the protein that encodes VEGFR-3, is highly expressed during embryogenesis, however, during human development it becomes limited to lymphatic vessels (Kaipainen et al., 1995). Nevertheless, there is a high expression of that gene in angiogenic sprouts by the tip cells. Furthermore, blocking this gene leads to a decrease in sprouting, vascular density, vessel branching and endothelial cell proliferation (Tammela et al., 2008). VEGFR-2 is the principal mediator of the proliferating, angiogenic and permeability enhancing capabilities of VEGF (Ferrara et al., 2003). Thus, making the VEGF/VEGFR-2 pathway the most well-characterized pathway in angiogenesis (Abhinand et al., 2016).

Angiogenesis is a fundamental part of the wound healing process. Wound healing is a very complex and dynamic phenomenon that involves numerous interactions between cells and mediators (Broughton et al., 2006; Singer & Clark, 1999). A wound is defined as a break in the epithelial integrity of the skin (Enoch & Leaper, 2008) so, incisions,

burns, cuts, among others, can cause this type of injury. Earlier authors consider that wound healing is divided into three well-defined overlapping phases (Broughton et al., 2006; Gonzalez et al., 2016; Singer & Clark, 1999; Wallace & Zito, 2019): inflammatory, proliferative and remodelling phase. There are many authors who still today prefer this 3-phase wound healing description where haemostasis is part of the inflammatory phase. A 4-phase wound healing concept is also accepted and includes haemostasis as an independent phase prior to the inflammatory (Enoch & Leaper, 2008; Kumar et al., 2015). In haemostasis, the clotting cascade is activated by the exposed collagen during wound formation. The clot is formed by platelets and fibrins preventing blood loss. Platelets secrete many growth factors that include the platelet-derived growth factor (PDGF), which initiates the wound healing cascade by attracting fibroblast, macrophages and endothelial cells (Enoch & Leaper, 2008). In the inflammatory phase, cell response is characterized by neutrophils that enter the wound site and clear it from cellular waste and invading bacteria. Leukocytes and macrophages then arrive at the wound, phagocyting bacteria and releasing degrading enzymes, continuing the cleansing process. The enzymes and cytokines secreted by the macrophages stablish chemical gradients that attract several other cells to the wound and maintain the viability of the healing process (Singer & Clark, 1999). The proliferative phase follows and angiogenesis, re-epithelization, granulation tissue formation and collagen deposition occur. This phase contributes to the reduction of the lesioned area and the re-establishment of the vascular network through angiogenesis. The fibroblasts migrate to the wound, attracted by growth factors, and start to proliferate and synthetize collagen and matrix proteins, aiming to create the new ECM (Broughton et al., 2006). The granulation tissue, denoted by proliferation fibroblasts and loops of capillaries within a loose ECM is forming. Angiogenesis plays a crucial role in this phase since both granulation and tissue deposition require nutrients and oxygen from the capillaries. Angiogenesis is induced by different growth factors such as VEGF and PDGF. The capillary sprouts then invade the clot and organize a vascular network in the granulation tissue (Enoch & Leaper, 2008). Finally, during the remodelling phase, collagen is deposited in an organized network forming a stable ECM. The granulation tissue is progressively remodelled, and the formation of scar tissue occurs. Scar tissue is avascular and composed of largely inactive fibroblasts, collagen fragments and other ECM components. The newly formed scar tissue does not have the original strength of the unwounded tissue, reaching only about 80% of the original tensile strength (Bowden et al., 2016). Excessive collagen deposition in this phase can lead to hypertrophic scar or

keloid (Broughton et al., 2006). The remodelling process can last up to an year or more (Gonzalez et al., 2016). The disturbance of one or more phases in wound healing can lead to the development of chronic wounds. The main causes that lead to chronic wounds are hypoxia, ischemia, reperfusion injury, defects in collagen synthesis and altered cellular response (Wallace & Zito, 2019). Furthermore, pathologies such as diabetes and obesity or risk factors such as smoking and malnutrition are related to the formation of chronic wounds. Both hypoxia and ischemia are conditions that are related to the reduced oxygenation in a tissue, which highlights the importance of a functional vasculature and, therefore, the crucial role of angiogenesis in wound healing.

The induction of angiogenesis is crucial for the tissue's oxygenation and consequent growth. However, uncontrolled angiogenesis and excessive vessel formation may cause several pathologies including cancer, endometriosis, psoriasis and nephropathy (Gupta & Zhang, 2005). According to WHO, cancer is the second leading cause of death globally accounting for approximately 9.6 million deaths in 2018. Tumour growth is angiogenesis dependant (Folkman et al., 1971) since blood vessels supply nutrients and oxygen to the tumour. Without angiogenesis the tumour will stagnate its growth at 2-3 mm (Sherwood et al., 1971). The release or synthesis of pro-angiogenic factors will activate the angiogenic switch, which can be defined as the transition from pre-vascular hyperplasia to highly vascularized and progressively outgrowing tumours (Baeriswyl & Christofori, 2009). This switch will cause an unbalance between angiogenic inducers and inhibitors, resulting in a pro-angiogenic outcome.

2.3. Biomaterials for Angiogenesis Induction

Angiogenesis is a central mechanism to healthy tissue maintenance and essential in processes such as wound healing and tumorous growth. Understanding the mechanisms that regulate angiogenesis, physio and pathological, is fundamental to recreate functional vascularization and integration of tissue engineered constructs. Tissue replacement with engineered constructs to combat medical disorders is the basis of tissue engineering (TE). TE is a growing market with a compound annual growth rate of 34.8% from 2018 to 2023, being expected to be worth around $109.9 billion in 2023 (*Tissue Engineering Market Size, Industry Analysis Report*, 2020). A bottleneck in TE is recreating functional vascularization to ensure appropriate integration and function of substitute bioengineered structures. Similarly to natural reparative angiogenesis, biomaterial-driven therapeutic

angiogenesis aims at integrating a network of functional vessels to engineered tissue replacements. Traditionally, biomimetic angiogenesis is stimulated by growth factors or proteins that generally lead to immature disorganized blood vessels, reminiscent of uncontrolled tumoral angiogenesis (W. Liu et al., 2020; Mastrullo et al., 2020). Biomaterials and bioactive materials can aid in effectively induct/inhibit angiogenesis.

Promoting angiogenesis is an extremely beneficial therapy in diseases such as ischemia, which compromises the blood supply to tissues and organs. Different types of cells can be used to promote angiogenesis. Vascular endothelial cells are often used in therapies since they can organize themselves into a functional capillary network and are of easy integration in tissues, however, there are some limitations to their usage such as limited expansion potential of terminally differentiated endothelial cells and differences in functional properties caused by donor variability (Jalilian et al., 2020). There are majorly three types of cells that are accepted for angiogenic purposes: somatic, stem and induced pluripotent stem cells (Saberianpour et al., 2018). Stem cells have big vascularization potential since they can differentiate into endothelial cells after exposure to angiogenic growth factors. Nevertheless, there are still concerns regarding their heterogenic nature and high individual variability (Jalilian et al., 2020). The growth and differentiation of cells is triggered by several specific conditions, which can be proportionated by scaffolds. Scaffolds are temporary three-dimensional structures that simulate a biological environment to deliver, align and maintain cell connection that favours angiogenesis (Saberianpour et al., 2018). Scaffolds are required to have several properties, namely: biocompatibility, for cell adherence and avoid rejection by the body, biodegradability, for the eventual replacement of the scaffold by the body's own cells and mechanical properties that allow for tissue's support and surgical handling (O'Brien, 2011). These structures are fabricated of natural materials such as collagen, fibrin and alginate or synthetic materials like carbon fibre, bioactive glasses, and Teflon (Nikolova & Chavali, 2019). The choice of which material to use is made based on the tissue's properties where the scaffold is to be integrated. For instance, the use of bioactive glasses is extremely common in TE, especially in hard tissues (bones) due to their mechanical resistance, angiogenic and osteogenic capabilities (Kargozar et al., 2016). Furthermore, they can be embedded with metallic ions like Cu^{2+} which upregulates VEGF expression and promotes neovascularization while also having antibacterial capabilities (Jacobs et al., 2020). Delivery of angiogenic molecules through scaffolds is a key strategy to

stimulate angiogenesis. Other than copper, angiogenic ions such as cobalt, silicate, strontium and magnesium are especially useful in bone regenerative scaffolds (J. H. Lee et al., 2020). Angiogenic proteins that are delivered include VEGF, PDGF, fibroblast growth factor and transforming growth factor β1 (J. H. Lee et al., 2020). Normally, for vascularization purposes, scaffolds need to be porous and mimic the ECM, which is essential when delivering angiogenic growth factors, since they all naturally bind to it (Martino & Hubbell, 2010). The use of scaffolds, natural or synthetic, allows for spatial and temporal control of angiogenesis, controlled release of growth factors and bioactive molecules and cell phenotype definition. Regardless, they are constructs of extreme complexity that need to be carefully engineered. From their surface topography and stiffness to pore structure, every detail must be meticulously tailored, otherwise their effectiveness is compromised.

2.4. Biomaterials for Angiogenesis Inhibition

Cancer therapies require angiogenesis inhibition rather than its induction. Kim et al. (1993) firstly demonstrated *in vivo* that VEGF inhibition successfully suppressed tumour growth, proving the therapeutical effects of VEGF inhibition. According to technavio, the VEGF inhibitors market will be worth around $10.2 billion in 2023 (*Vascular Endothelial Growth Factor (VEGF) Inhibitors Market Size Worth $10.2 Billion by 2023 - Technavio | Business Wire*, n.d.). As of January 2021, the U.S Food and Drug Administration has approved 14 different drugs that predominantly target VEGF or its receptors. Inhibiting VEGF will prevent new tumorous vessel formation which compromises the nutrients and oxygen delivery, therefore “starving” the tumour. Although promising, the current drugs still present problems such as inefficacy and serious side effects (Ribatti, 2017). Reports of antiangiogenic drugs that targeted the VEGF pathway promoting metastasis and invasion were made in 2009 (Ebos et al., 2009; Pàez-Ribes et al., 2009). Despite demonstrating anti-tumour effects, these drugs also provoked tumour progression and adaptation in mouse models. VEGF inhibitors efficiency is compromised by genetic mutations, vascular changes, up-regulation of other angiogenic promoters and metastasis (Ribatti, 2010a). VEGF biomarkers can help identifying subsets of patients who probably will respond better to a certain antiangiogenic therapy, identifying early clinical benefit and/or treatment resistances ultimately providing a personalized cancer treatment to each individual (Ribatti, 2010a, 2010b). In the last few years there has been progress in identifying and validating

biomarkers that predict overall survival and treatment effectiveness in cancer patients (Balikova et al., 2019; De Haas et al., 2014; Hein et al., 2015), however, there is still a long way to go for personalized cancer therapies (Liang et al., 2019). Moreover, the growing number of antiangiogenic agents that are being approved intensifies the need for biomarkers that assess safety and efficacy (Mukherjee, 2018). As an alternative to conventional cancer therapies, nanomedicine and nanoparticles arise as potential candidates.

Nanoparticles have been widely investigated in the biomedical field due to their many applications from targeted drug delivery and optical bioimaging to biosensors and immunoassays (Abdalla et al., 2018). The unique properties of nanomaterials can be used in our advantage not only to diagnose cancer but develop new therapeutic approaches for its treatment. When compared to current cancer diagnostic tools, several nanoparticles-based assays displayed a far superior selectivity and sensitivity (Zhang et al., 2019). Due to their large surface area to volume ratio, nanoparticles can more efficiently capture cancer biomarkers (Ferrari, 2005; Jia et al., 2017). This nanotechnological diagnosis approach is expected to reach clinics in a near future since some assays entered clinical trials. Regarding antiangiogenic cancer therapy, nanoparticles such as gold (Beik et al., 2019; Lim et al., 2011; Siddique & Chow, 2020; Vines et al., 2019), silica (Pasqua et al., 2016; Setyawati & Leong, 2017), copper (Benguigui et al., 2019; Song et al., 2014) and silver (Huy et al., 2019; Vlăsceanu et al., 2016), have demonstrated antiangiogenic capabilities and promising results for new combinatory therapies. The future of nanomedicine is promising and offers several new opportunities for the creation of therapies to combat and diagnose cancer. Nevertheless, additional knowledge of material properties, cancerous cells metabolic properties and physiological barriers is required to improve antiangiogenic nanoparticle therapies (Abdalla et al., 2018). Furthermore, the challenge of targeting exclusively cancer cells without side effects still remains (Mukherjee, 2018). Finally, as the demand and need for knowledge increases, the recent advances in customizable biomaterials pose an interesting solution to create physiologically-relevant tumour models that will aid in developing relevant studies and discovery of new anti-angiogenic drugs and therapies (Nguyen & Murphy, 2018).

The angiogenic process is mediated by mechanical, genetic, and biological factors, where each factor plays a specific role and differently impacts the whole process. Such is the complexity of the angiogenic process, that assessing the effects of a change

in an individual factor is extremely difficult. Computational mathematical models that are capable of simulating biological angiogenic environment are powerful predictive assets that aid in the understanding of angiogenesis, its processes and the repercussions of altering different variables (Peirce, 2008).

CHAPTER 3 – COMPUTATIONAL AND MATHEMATICAL MODELLING

3. Computational and Mathematical Modelling

Computational modelling is an indispensable tool for analysing systems of extreme complexity such as biological systems. Computational models can mimic the behaviour of complex systems based on the properties of the system's components. These simulated environments offer the possibility of changing the properties of their components and the interactions between them, allowing for an immense number of hypothesis to be tested. Furthermore, it also permits to understand and predict how different components influence the final outcome (Brodland, 2015).

The majority of physical essays can be duplicated by accurately constructed computational models. The construction of a computational model firstly requires the development of a conceptual model that considers how the system of interest operates, namely, the components that are involved and how these components are likely to interact with each other. The conceptual model should be turned into mathematical form, which comprises the second phase of the computational model creation. It is crucial that all the relationships and interactions between the system's components are expressed as mathematical equations. Furthermore, it is also necessary to carefully considerate which type of data representation, integer, Boolean, amongst others, is the most suitable for each variable. The development of the mathematical model is arguably the most important part of the whole process, since good mathematical models lead to good computational models and scientifically relevant observations. Finally, the mathematical relationships previously established should be coded using an appropriate computational framework (Brodland, 2015).

Biological systems are extremely complex, involving a multitude of scales and processes. Managing every scale of a biological process is a non-trivial problem for mathematical models so, they are divided into different scales. That is the case of cancer and wound healing (Vilanova et al., 2017b). Both tumorous and wound healing angiogenesis mathematical models usually are divided in three different scales: subcellular scale, cellular scale, and the tissue scale. Each scale has a different order of magnitude and analyses different phenomena. The subcellular scale includes oncogene transcription and mutational events. On the other hand, the cellular scale includes proliferation apoptosis and endothelial cell migration. Finally, the tissue scale is in the order of centimetres and it includes angiogenesis (Vilanova et al., 2017b). There are three

types of models. Continuous, discrete and hybrid. The decision on which model to use is based on the scale of interest. The study of individual cell behaviour at cellular and subcellular scale is made using discrete models. Indeed, discrete models can individually track cells, however, they are spatially and temporally limited. Continuous or continuum models are indicated for tissue level studies and although not able to individually track cells, they are not spatially and temporally limited. Hybrid models are interesting when there is a need for representing some variables as a continuous field and others as a discrete entity (Buganza Tepole & Kuhl, 2013; Vilanova et al., 2017b). This approach is more complex, regardless, it combines the advantages of both continuous and discrete models.

Discrete models are suitable when the modelled entities and their unique behaviours are explicitly represented. Time and space increments are considered distinct entities and the objects present in the environment are treated as individual units (Peirce, 2008). These models are usually formalized by sets of ordinary differential equations (ODE) that manage the behaviour of each distinct entity. The differential equations establish the evolution in time of a characteristic variable and how a characteristic variable of a single entity interacts with other variables through coupling terms (Buganza Tepole & Kuhl, 2013). Different types of discrete models are used for biological systems modelling. Those include cell-based models with the most common being the cellular automata and the cellular Potts model (Anderson & Chaplain, 1998; Peirce, 2008; Vilanova et al., 2017b). Cellular automaton or cellular automata is a type of a discrete model characterized by numerous individual particles that are allowed to interact with each other according to certain rules. The space is divided with a lattice and each site shall be occupied by only one cell, also, the system must be finite and have clear boundaries. Furthermore, this model does not account for the cell shape (Agapie et al., 2014; Chopard & Droz, 1998). The cellular Potts model is a grid based stochastic approach where each cell may be composed by different lattice locations. This model accounts for the shape of the cell capturing the stochastic aspects of both cell movement and deformation. In addition, this type of model also can describe the evolution of the cells energetically (Rens & Edelstein-Keshet, 2019; Scianna, 2015). It is also important to note that discrete models demand more computational power, since every cell has its own equation(s).

Continuous models assume that the modulated processes are continuous in time and space. In terms of angiogenesis, continuum models describe the formed vessel network in terms of cell densities (Pillay et al., 2017). In this type of models both time and space are managed by partial differential equations (PDEs) and each field needs one equation. Continuous data discretization is needed to preserve the variable dependencies. The discretization process is even more relevant in the context of systems biology (Dimitrova et al., 2010) so, both time and space need to be divided into discrete states. Time discretization is usually made by the finite difference methods. Depending on the complexity of the space's geometry, its discretization can be more or less complex. In order to solve PDEs, mesh-dependent and meshless methods are commonly utilized for spatial discretization (Rabczuk & Zhuang, 2018). For instance, mesh-dependent methods include the FEM, and meshless methods include the RPIM. Simpler approaches such as the finite volume and finite differences methods are also possible although not indicated for arbitrary shapes. The discretization allows to solve the equations that determine how a continuum field evolves in time, how it varies in space over the domain of interest and finally how a field interacts with others though coupling terms (Buganza Tepole & Kuhl, 2013).

As it was discussed, different methods are used for studying different phases and phenomena regarding angiogenesis. Understanding which types of angiogenic computational models exist and which methods are used to model them is extremely relevant for this work. Therefore, in the following sections such matters are addressed.

3.1. Angiogenesis Modelling

Angiogenesis is a central mechanism in healthy tissue maintenance and tissue regeneration but also in tumorous growth. Being such an essential process throughout human life both in health and in disease it sparked an immense curiosity in the scientific community since its discovery. Many different *in vivo* and *in vitro* studies have contributed to understand angiogenesis and its mechanisms. Nevertheless, due to the extreme complexity of the angiogenic process some events are not still fully described. *In silico* models (computational models) are a cheaper and versatile solution for studying angiogenesis and hypothesis testing. These *in silico* models focus on specific angiogenic events, control behaviours of singular cells, manipulate the behaviours and interactions

between the system's components, amongst other advantages (Brodland, 2015). Thus, being extremely useful and utilized for angiogenesis related studies.

Deakin (1976) produced the first attempt at modelling angiogenesis. The developed model was a simple continuum model that considered two variables: the endothelial cell density and a tumour angiogenesis factor (TAF). This model described the movement of a single endothelial cell in response to TAF. Almost a decade later, in 1985, one of the most relevant and cited tumour-induced angiogenesis models was developed. Balding & McElwain (1985) proposed a one-dimensional continuum model that represented the interactions between the TAF (a chemical species), the density of the sprout tip and the capillary density, describing tumour-induced capillary growth. Also, this model distinguished between tip and stalk endothelial cells and included the phenomena of anastomosis. The authors suggested that similar models could be developed to describe other biological phenomena, especially wound healing given the similarities between tumorous and wound healing angiogenesis. Five years later, in 1990, the first model of epidermal wound healing was proposed (Sherratt & Murray, 1990). The continuum model developed by Sherratt and Murray described in a two-dimensional domain the distribution of cell density and cell proliferation in both time and space. Although not explicitly describing angiogenesis, this model laid the foundations for future wound healing models. Chaplain & Byrne (1996) reported that both tumorous and wound healing processes could be modelled using the similar mathematical frameworks, which opened the doors for the development of new models.

Nowadays many relevant continuous, cell-based and hybrid angiogenesis models have been developed. Other than wound healing and tumorous angiogenesis models (Amann et al., 2017; Chaplain, 2000; Phillips et al., 2020; Vilanova et al., 2017a, 2018) , relevant skeletal muscle angiogenic models have also being developed (Carlier et al., 2012; Gang Liu et al., 2011; Olfert et al., 2016). Nevertheless, all types of angiogenic models contribute with relevant data that can be used transversally to improve future models. The present work will be more focused towards wound healing angiogenic modelling given that it is a tightly regulated, organized and time defined event, also, it is the desired scope for this work. Therefore, the next subsections will review some of the most relevant angiogenesis models with an emphasis on wound healing angiogenesis.

3.1.1. Continuous Models

The choice of a model depends on the biological abstraction of the phenomena. Regarding wound healing, a phenomena that involves interaction between many specialized cells and chemical compounds (Reinke & Sorg, 2012), a detailed discrete modelling approach at tissue scale to describe the behaviour of entire cell populations would be overwhelmingly expensive in terms of computational cost. Thus, a continuous approach is more adequate.

As it was previously mentioned, Sherratt & Murray (1990) proposed the first model of wound healing which did not explicitly considered angiogenesis. Pettet et al. (1996a) extended the concepts introduced by Sherratt & Murray and included angiogenesis, developing the first wound healing angiogenesis models. This one-dimensional model describes the migration of tip cells according to a macrophage-derived chemoattractant (TAF) and the formation of new blood vessels during wound healing modelled by a system of three PDEs. The considered dependable variables were capillary tip density (ρ_{tip}), chemoattractant concentration (C_{chem}) and blood vessel density (ρ_{bv}). Capillary tip density evolution is described by:

$$\frac{\partial \rho_{tip}}{\partial t} = \underbrace{\mu_{tip}\frac{\partial^2 \rho_{tip}}{\partial x^2}}_{Random\ Motility} - X_{tip}\underbrace{\frac{\partial}{\partial x}\left(\rho_{tip}\frac{\partial C_{chem}}{\partial x}\right)}_{Chemotaxis} + \underbrace{\lambda_1 C_{chem}\rho_{bv}}_{Budding} - \underbrace{\lambda_2 \rho_{tip}}_{Decay} - \underbrace{\lambda_0 \rho_{tip}^2}_{Anastomosis} \quad (3.1)$$

In this formulation μ_{tip} represents the constant coefficient of random motility and the Greek letter X_{tip} represents the chemotaxis constant coefficient. Chemotaxis is the migration of cells in response to chemical gradients (Yu Wang et al., 2011) and in this model it was the assumed to be the main contribution to the tip flux. The constant of proportionality $\lambda_1$relates to the assumed proportional relation between budding and the attractant concentration and vessel density. The dominant contributions to tip loss, for simplicity purposes, were assumed to be natural death and tip-to-tip anastomosis. A linear decay of tips with rate λ_2 was used to model natural death. Regarding tip-to-tip anastomosis, its modulation was made using a proportional term to the square of the tip density (ρ_{tip}^2) with rate λ_0. The chemoattractant concentration (C_{chem}) is governed by:

$$\frac{\partial C_{chem}}{\partial t} = \underbrace{D_{at}\frac{\partial^2 C_{chem}}{\partial x^2}}_{Diffusion} + \frac{\lambda_3}{2}\left(\underbrace{1 + tanh\left(\frac{\rho_{bv_{char}} - \rho_{bv}}{\lambda_{ap}}\right)}_{Production}\right) - \underbrace{\lambda_4 C_{chem}}_{Decay} - \underbrace{\lambda_5 C_{chem}\rho_{bv}}_{Removal} \quad (3.2)$$

The attractant diffusion coefficient is represented by D_{at} and is assumed constant. The maximum rate of attractant production occurs when both oxygen concentration and vessel density are low and is represented in the model by λ_3. Attractant production becomes negligible at the vessel density of $\rho_{bv_{char}}$ and λ_{ap} is the constant that denotes the rate at which the chemoattractant production falls with increasing vessel density. The authors also assumed that local vascular network removal and natural decay are the ruling mechanisms for attractant loss. The rates at which these occur are represented by $\lambda_5$for the former and λ_4 for the latter. Blood vessel density (ρ_{bv}) is modelled by the following PDE:

$$\frac{\partial \rho_{bv}}{\partial t} = \underbrace{\mu_{bv} \frac{\partial}{\partial x}\left(\rho_{tip} \frac{\partial \rho_{bv}}{\partial x}\right)}_{Random\ Motility} - \left(\underbrace{\mu_{tip} \frac{\partial \rho_{tip}}{\partial x} - X\rho_{tip} \frac{\partial C_{chem}}{\partial x}}_{Snail\ Trail}\right) \tag{3.3}$$

In this equation μ_{bv} is the constant vessel random motility coefficient. The "Snail Trail" term in the equation refers to the model developed by Balding & McElwain (1985), which models the elongation of the capillaries that follow a particular tip and is assumed to be the main method of vessel production. The "Snail Trail" presence highlights the importance of tumour-induced angiogenesis models for the modulation of wound healing angiogenesis and the transversality between the modulation of both phenomena. Pettet et al. were successful in reproducing a wound healing model which described, quantitatively, the sequence of events associated with angiogenesis in wound healing (Pettet et al., 1996b). Albeit this approach was a success, the model had some limitations that included the effect of oxygen delivery in the wound and no distinction between cell death and anastomosis. Pettet and co-workers also developed one of the first wound healing models that accounted for the role of oxygen in controlling chemoattractant production. The model used six PDEs that modelled the evolution of capillary tips and sprouts (blood vessels), fibroblasts, ECM, chemoattractant and oxygen (Pettet et al., 1996b). Regarding results, this one-dimensional model indicates that low oxygen levels in parts of the wound are necessary for the healing unit to advance, excessive levels of oxygen cease angiogenesis and that healing rate is oxygen dependant. These behaviours are in accordance with experimental observations. The modelling approaches based on conservation by Pettet and co-workers were extremely influential. Byrne et al. (2000) developed a similar 3 species model for angiogenesis phase of soft-tissue healing and used the same dependant variables as in Pettet et al. (1996a). However, in this work the

obtained results were compared with clinical data. Also, a vessel remodelling term was added to the equation that describes blood vessel density. When comparing the results obtained for wound surface area over time, there was a good qualitative agreement between theoretical and clinical data for both healthy and chronic wound healing.

Schugart et al. (2008) developed the first model dedicated to the role of tissue oxygen tension on acute wound healing. This model was built on the six species mathematical model by Pettet et al. (1996b). The proposed reaction-transport model consisted of seven PDEs that modelled: density of capillary tips, density of capillary sprouts (blood vessels), concentration of oxygen, density of inflammatory cells, concentration of chemoattractant, density of fibroblasts and density of ECM. This model suggested that hypoxia is averse to wound healing, hyperoxia promotes both angiogenesis and wound healing and finally that the use of intermittent oxygen treatment may stimulate angiogenic response. These findings match the literature (Allen et al., 1997; Balasubramaniam et al., 2007; Liao & Johnson, 2007; Patel et al., 2005). Simplifications of this model include considering only one type of chemoattractant and describing the formation of new blood vessels in terms of endothelial cells densities. Regarding oxygenic therapies investigation, Flegg et al. (2009, 2010) developed the first mathematical model for studying the effectiveness of hyperbaric oxygen therapy (HBOT) for chronic diabetic wounds. Based on the work by Pettet et al. (1996b), the HBOT one dimensional study model by Flegg and co-workers had six chemical species governed by a system of PDE. The effects of HBOT therapy were studied in both normal and chronic wounds. Regarding normal wounds, the model suggested that HBOT marginally assists the wound closure and its application is not cost effective. Chronic wounds on the other hand benefit from HBOT, however there are some aspects to be considered: firstly, the HBOT treatment must continue until healing is complete else the healing will stall, secondly higher oxygen pressures and longer sessions positively impact the healing rate and finally HBOT will not be effective to treat non-healing wounds due to lack of growth factor production/low chemotactic responsiveness. This model presented several different clinically relevant results. Furthermore, permitted the testing of several different HBOT protocols, while also identifying wounds that will benefit to such therapy. Posteriorly to this model, Flegg and colleagues continued to develop models that, rather than being used to gain insights into wound angiogenesis mechanisms, are a tool for improving and assessing new therapies. The models include a three PDE model based in the principle of

conservation (Pettet et al., 1996a) to compare different non-healing wound treatments (Flegg et al., 2012) and a simplistic mathematical model to study healing of venous ulcers using compression therapy by short stretch bandages and graduated three layered bandage where there was good agreement between the modelled results and experimental data (Flegg et al., 2015).

All the models previously mentioned only considered chemical aspects of wound healing angiogenesis but there is also mechanical influence. Mechanochemical wound healing models account for the forces that are applied to the ECM and consider the remodelling wound healing phase (Flegg et al., 2009). Xue et al. (2009) developed the first mechanochemical model which included angiogenesis to describe wound healing in an ischemic context. ECM was considered a viscoelastic material described by its density (ρ_{ECM}) and its velocity (v). The PDE for ECM density is:

$$\frac{\partial \rho_{ECM}}{\partial t} + \nabla(\rho_{ECM} v) = \underbrace{G_{\rho_{ECM}}(\rho_{fb}, C_o, \rho_{PDGF})}_{Growth\ and\ Decay} \tag{3.4}$$

In this equation $\nabla = \frac{\partial}{\partial x}$, and the term $G_{\rho_{ECM}}(\rho_{fb}, C_o, \rho_{PDGF})$ refers to the growth and decay term due to collagen secretion by fibroblasts and ECM degradation by metalloproteinases. This term depends on the concentration of oxygen (C_o), fibroblast density (ρ_{fb}) and the density of PDGF (ρ_{PDGF}). ECM also is modelled by a motion equation. Assuming that that ECM motion in wound healing is very slow, the momentum equation is:

$$\nabla\sigma = -\nabla p + \nabla\sigma_{ds} = 0 \tag{3.5}$$

Where σ is the total stress tensor, p is the isotropic pressure and the deviatoric stress is represented by σ_{ds}. Both these equations define the ECM. Other species in the model include oxygen, PDGF, VEGF, capillary tips and sprouts, macrophages, fibroblasts and chemicals/cells who move inside the ECM. This model is an extension of the works by Pettet et al. (1996b) and Schugart et al. (2008) and is relevant for studying pressure ulcers, since they are under mechanical pressure. This model offered interesting insights, namely that an ischemic wound is of slower healing than a normal wound. For 20 days the ischemic wound was under extreme hypoxia whereas the normal wound was only under hypoxia (limited to wound edge) only during inflammatory phase/early proliferative. Finally, the peak time of the number of macrophages in the ischemic wound

was longer which corresponds to a longer inflammatory phase. Their findings are in agreement with the literature (Roy et al., 2009).

Olsen et al. (1997) used the concepts of haptotaxis and haptokinesis to model endothelial cell density during wound healing angiogenesis. Comparing to the previous mentioned models, this one differs since it only considers two species and none is chemical. Also, it is the first two-dimensional model referred and the first to consider the interactions between endothelial cells and ECM in wound healing angiogenesis. Two coupled PDE describe the spatio-temporal evolution of ECM and endothelial cells density. The extension to two dimensions gave the model a more realistic representation of wound geometry and boundary conditions. The two-dimensional approach demonstrated that angiogenesis occurred by the inwards movement from the wound margins and base by ECM and cells however, cellular activation was not considered. Another model that also uses two PDE to model healing angiogenesis was developed by Gaffney et al. (2002). This one-dimensional model is based of the three species model by Pettet, in terms of capillary tip density modelling, however the tip flux equation was modified to reduce chemotactic and haptotactic bias. The modelled species are capillary tip and endothelial cell densities. Qualitative features of the model's results were observed in cutaneous healing. Furthermore, this minimal model should be used to make predictions regarding propagation speed, capillary tip and endothelial cell density maximum.

Most continuous wound healing angiogenesis models assume a one-dimensional geometry, however, expanding dimensions allows for a more realistic approximation of the wound healing environment. Vermolen & Javierre (2012) built upon the simplified models of Maggelakis (2003) and Sherratt & Murray (1991), to develop the first model that combined wound contraction, angiogenesis and epidermal closure. Due to the dimensional complexity of this model (considering dermis and epidermis), there was a need to use an advanced discretization technique. In this case, the FEM with triangular elements was used to solve the PDEs system. The wound contraction phenomena was modelled by PDEs that described fibroblast and fibroblast produced ECM concentration. This modelling approach assumes that fibroblasts are mobilized to the wound and start producing ECM on which they exert a contractile force. Regarding angiogenesis, PDEs that model the evolution of oxygen and VEGF concentration and capillary density were used. As the vascular network is damaged in the wound there is a lack of oxygen which

initiates the production of VEGF causing the proliferation of endothelial cells and the restoration of the vascular network. Finally, the wound closure phenomena is assumed to be regulated by only one epidermal growth factor (EGF) which determines the regeneration of epidermal cells. The heal state is reached when the production of the EGF becomes stable of the wound. Thus, this phenomenon is modelled by EGF concentration and epidermal cell density. The mechanochemical model's results indicate that kinetics of angiogenesis affect the healing time of the wound, re-epithelization occurs differently in early and later stages of wound closure and low oxygenation trigger growth factors secretion. Furthermore the model also obtained results consistent with experimental data (Escámez et al., 2004; LAPLANTE et al., 2001) regarding the mechanisms of healing through keratinocytes and stratification. Valero et al. (2013) extended the works of Javierre et al. (2009) regarding wound closure by coupling angiogenesis with wound contraction. To do so, the effect of fibroblast contraction was added to the angiogenesis model. The governing equation for fibroblast density (ρ_{fb}) is:

$$\frac{\partial \rho_{fb}}{\partial t} + \nabla\left(\rho_{fb}\frac{\partial \Delta x_{ECM}}{\partial t}\right) = D_{fb}\nabla^2\rho_{fb} + \lambda_{fbp}C_o\rho_{fb}\left(1 - \frac{\rho_{fb}}{B_{MAX}}\right) - \lambda_{fbd}\rho_{fb} \tag{3.6}$$

In this equation Δx_{ECM} represents the ECM displacement vector due to wound contraction, $D_{fb}$is the fibroblast diffusion rate, λ_{fbp} corresponds to the maximum rate of fibroblast proliferation, B_{MAX} is the fibroblast maximum capacity in the dermis and, finally, λ_{fbd} corresponds to the fibroblast death rate. In this model angiogenesis is described trough fibroblast density and concentrations of oxygen and macrophage-derived growth factors. Regarding the mechanical model of wound contraction, the authors considered the work of Moreo et al. (2008) where using the species density values, the net stress of one fibroblast cell per unit of ECM (σ_{cell}) can be obtained. σ_{cell} depends on the tissue volumetric strain, and is modelled by:

$$\sigma_{cell}(\theta) = \begin{cases} K_{pas}\theta & \theta < \theta_1 \\ \frac{K_{act}\sigma_{max}}{K_{act}\theta_1 - \sigma_{max}}(\theta_1 - \theta) + K_{pas}\theta & \theta_1 \leq \theta \leq \theta^* \\ \frac{K_{act}\sigma_{max}}{K_{act}\theta_2 - \sigma_{max}}(\theta - \theta_2) + K_{pas}\theta & \theta^* \leq \theta \leq \theta_2 \\ K_{pas}\theta & \theta > \theta_2 \end{cases} \tag{3.7}$$

In this mechanical model, θ represents the volumetric strain of the tissue where cells are allocated. θ_1, θ_2 and θ^* represent, respectively, the shortening strain of the contractile element, the lengthening strain of the contractile element and the quotient $\frac{\sigma_{max}}{K_{act}}$, where σ_{max} is the maximal cellular active stress per ECM unit and K_{act} the

volumetric stiffness moduli of the actine filaments of the cell. K_{pas} represents the volumetric stiffness moduli of the passive cell components. Valero and co-workers considered the skin a hyperplastic material, which grants the model a more realist approach, which was also a novelty in wound healing angiogenesis. The non-linear model was solved using a FEM approach. Circular and elliptical wound geometries of the same area were analysed. Numerical results illustrated a severest hypoxia state in the circular wound centre, faster fibroblast migration to the centre of the elliptical wound and similar contraction rate between both geometries. Furthermore, the geometry of the wound changes due to the stresses considered in its geometry, which is observed in a real wound. Finally, the circular wound showed a higher contraction percentage regarding its original size (27%) when compared to the elliptical wound (24%). This work obtained good experimental validation regarding contraction curve shape and later start to the contraction process in the elliptical wound and macrophage density curve for non-ischaemic wounds (Gross et al., 1995; McGrath & Simon, 1983; Roy et al., 2009). There are some differences in contraction times and contraction rates, however, most of the models are animal skin models whose properties are different from human skin.

3.1.2. Discrete Models

Discrete models are suitable to study the behaviour at the level of individual cells allowing for a detailed prediction of the structure and morphology of the capillary network, which is not possible in continuous models. Stokes & Lauffenburger (1991) developed one of the first stochastic models that described angiogenesis. This model described bud formation from already existing parent vessels and the migration of the sprouts. The mechanisms for cell migration, random motility and chemotaxis, were considered stochastic events. In this two-dimensional model an ODE was used to describe the evolution of each sprout density, which varies as the tip cells migrate further away from the parent vessel. Also, tip cell velocity was equally modelled using an ODE. Results obtained suggest that greater chemotaxis can be detrimental to an effective network formation so, a moderate chemotactic response is required. In the same year, Stokes et al. validated the proposed model by comparing it with experimental data, which supported the robustness of their model. Regarding wound healing, Callaghan et al. (2006) modelled some features of wound healing using a stochastic approach. The model described the invasion of a wound by fronts of cells, where the measured parameters were speed and front width, and the motion of each cell was described as reinforced random walk towards

a stimulus. The model presented results in one and two-dimensions, however, since the wound healing process was oversimplified, the results could not be related to biological systems. The usage of stochastic models for vascular growth induced by tumours or wound healing is not common so this approach remains fairly unexplored in this modelling area.

McDougall et al. (2002) extended the approach of Anderson & Chaplain (1998) by including fluid flow on the vascular network. The previously developed discrete model by Anderson & Chaplain (1998) simulated the formation of a capillary network due to endothelial cell chemotactic response in the presence of TAF. The model accounted for the cells' interactions with the ECM. McDougall and co-workers discretized the PDEs defined in the former continuous model using the Euler finite difference method. A biased random walk model governed the movement of individual endothelial cells at the capillary sprout tips. The discretised endothelial cell equation was given by:

$$\rho_{ec_{i,j}}^{q+1} = \rho_{ec_{i,j}}^{q} P_s + \rho_{ec_{i+1,j}}^{q} P_l + \rho_{ec_{i-1,j}}^{q} P_r + \rho_{ec_{i,j+1}}^{q} P_u + \rho_{ec_{i,j-1}}^{q} P_d \tag{3.8}$$

Where ρ_{ec} represents the endothelial cell density, i (horizontal axis) and j (vertical axis) represent the position of the endothelial cell in a two-dimensional domain. The letter q is a positive constant that is equal to the quotient between time (t) and the magnitude (k) of the discrete increments, so $q = \frac{t}{k}$. Finally, P is a coefficient that represents the probability of the endothelial cell moving to the left (P_l), right (P_r), up (P_u), down (P_d) or stay stationary (P_s). This discrete model captured anastomosis, cell proliferation and branching. The simulation solves the discrete equation (Eq.3.8) for each time step and numerically generated the five different P coefficients. In the end of the simulation, two structurally different capillary networks are formed. The first one is generated as a response to a linear TAF concentration profile from a line source of tumour cells, whereas the second one is created in a response of a radially symmetric concentration profile forming a small circular tumour. Regarding the fluid flow through the vascular networks, the flow rate (Q) in each capillary was assumed to follow the Poiseuille's law:

$$Q = \frac{\pi R_{ce}^4 p_{ce}}{8\mu_{fluid} L_{ce}} \tag{3.9}$$

In this equation, R_{ce}^4 represents the radius for a single capillary element and p_{ce} the drop in pressure of each element between two joining nodes. Regarding the variables in the divisor part of the equation, μ_{fluid} represents the viscosity of the fluid and finally

L_{ce} is the length of a single capillary element. The authors studied how injected chemotherapeutic drugs interact with the tumour and concluded that the structure of the highly interconnected vasculature around the tumour should be considered for chemotherapy since the model suggested that the vascular structures around the tumour cause relatively low rates of drug delivery to the tumour. Furthermore, the model is adaptable to investigate the flow from the tumour to the main blood vessel.

Peirce et al. (2004) developed a cell-based model, cellular automata, to predict microvascular network patterning in response to hemodynamic forces and exogenous focal VEGF application that integrated epigenetic stimuli, molecular signals and cellular behaviours. Proliferation, differentiation and migration were also considered. The model's simulation environment was a two-dimensional space formed a surface area of 11840 pixels. In terms of the hemodynamic forces, the results obtained by the model were compared to *in vivo* results obtained from rat mesenteries. Some aspects of the simulation predictions agreed with the observed in the *in vivo* process. Regarding the VEGF stimuli, the model predicted that the vessel length density increased in the regions receiving the stimulus, which was in accordance with *in vivo* measurements made in rat dorsal subcutaneous tissues. Furthermore, the vessel maturation patterns also presented good results in relation to the *in vivo* counterpart. Merks et al. (2004) developed a cellular Potts model with the addition of PDEs which modelled a chemoattractant. This model simulated chemotaxis, haptotaxis, cell elongation and adhesion, amongst other phenomenology of human umbilical vascular endothelial cells. This discrete approach involves considering the cells' interactions energy and in cellular Potts models this is usually defined with the Hamiltonian. In this case:

$$H = \sum_{i,j} J_{n_i,n_j}\left(1 - \delta_{n_i,n_j}\right) + \alpha \sum_{n} (a_n - A_n)^2 \tag{3.10}$$

In this equation, n_i represents the index of the lattice sites and n_j the index of the neighbouring lattice site. Membrane bonds are represented by connections between neighbouring lattice sites of unlike index $n_i \neq n_j$, that have a characteristic bond energy J_{n_i,n_j}. The Greek letter α represents resistance to compression and the term $(a_n - A_n)$ is a volume constraint imposition to the biological cells. Finally, the Kronecker delta $\delta_{i,j} = \{1, i = j; 0, i \neq j\}$. Regarding the chemotaxis phenomena, the motion of cells along the chemoattractant gradient (c) was defined by:

$$H' = H - \sum_i X_r \frac{c(x,t)}{s\,c(x,t)+1}(1-\delta_{ni,nj}) \tag{3.11}$$

The letter H represents the Hamiltonian defined in Eq.3.10, the letter s is the saturation of the chemotactic response and X_r is the chemotactic response strength. Cell elongation affects the vascular pattern so, the authors added a cell-length constraint to the Hamiltonian:

$$H'' = H' + \lambda_{L_t}(L_a - L_t)^2 \tag{3.12}$$

The variable L_a is the length of the cell along its longest axis, L_t represents its target length and the Greek letter λ_{L_t} is the strength of the length constraint. The authors also implemented a connectivity constraint to prevent cell splitting into disconnected patches. The lattice used in the simulation had the dimensions of 500 by 500 lattice units. The results regarding intercellular cell adhesion suggested that a reduction in the adhesivity of the endothelial cells caused the cells to not form a vascular network or form unstable networks. This suggests that the adhesion is essential for a stable vascular network formation. Upon the publishing of this work, the authors were in the process of validating the model using time-lapse video microscopy experiments.

Gevertz and co-workers developed a two-dimensional cellular automata model with coupled with PDEs which modelled VEGF, its proteins and their interactions. These equations were solved using the finite difference approximation method on a triangular grid. The referred model aimed to simulate the effects of vasculature evolution on early tumorous growth in the brain and couples the remodelling of the microvasculature with the evolution of the tumour mass. Also, VEGF, Ang-1, Ang-2 and their receptors concentrations determined the modelled vasculature properties. Furthermore, tumorous growth dynamics were studied using the Voronoi tessellation and mechanical confinement pressure was included to simulate the confinement by the skull. The authors verified that if the VEGFR-2 pathway was sufficiently stimulated a concentration gradient to which endothelial cells are attracted is formed and the vessels penetrate the tumour and prevent its "starving" by providing oxygen. In the other hand, if this pathway is inhibited and there is not VEGF secretion, the tumour does not proliferate, vessel regression is verified and the tumour starves, being overwhelmed by the hypoxic environment (Gevertz & Torquato, 2006). The tumour stops growing at a diameter of 1.4mm which is in accordance to experimental observations (Brat et al., 2003).

Bauer et al. (2007) developed the first cell-based model of tumorous angiogenesis. The cellular Potts model was used to describe endothelial cell migration, growth, division, adhesion and stromal evolution. Much like the models by Gevertz & Torquato (2006) and Merks et al. (2004), Bauer and co-workers also used PDEs to describe the chemoattractant diffusion. Since it was a cellular Potts model, the Hamiltonian regulated the shape of the cells, mutual adhesive interactions and chemotactic movement of the endothelial cells. This model was capable of reproducing realistic capillary sprout morphology quantitatively comparable to the literature in terms of diameter and wideness of the capillary sprouts (S. Lee et al., 2005; Lobov et al., 2002). Also, the authors concluded that local VEGF gradient influences the morphology of the capillaries and sprout extension is affected by the proliferating region and cellular functions cooperation, since as the proliferating region was moving further from the sprout tip the sprout extension was faster. Finally, the authors refer that anastomosis and branching occur because they are preferred lower energy states. Two years later Bauer et al. (2009) extended and validated their previous model, emphasizing the effects of the topography of the ECM in migration speeds in angiogenesis. The results suggested that both density and heterogeneity of the ECM influences capillary branching and that sprout extension speeds depend on the ECM characteristics. In another approach, Bentley et al. (2008) developed a discrete agent-based model to study the VEGF-A tip cell induction with delta-like 4 notch-mediated lateral inhibition. This three-dimensional model consists of a single hollow cylindrical capillary with ten endothelial cells composed of smaller agents that represent sections of the membrane. Each of the smaller agents contains information regarding its own internal quantities of proteins and can potentially extend to a single filopodium. This model's critical parameters are VEGF-A gradients and concentration and filopodia extension. This model allowed to conclude that the VEGF gradient affects the selection rate due to filopodia extension, since VEGF concentration affects the number of tip cells and that loss of delta-like 4 resulted in increased tip cell density. The model was validated by qualitative similarities to experimental observations.

Daub et al. (2013) created a cellular Potts model which described cell-matrix interactions at the level of individual cells to explore the role of ECM-guided cell motility in angiogenesis. The modelling domain consisted of a rectangular dish of 250 by 300 lattice units with 125 endothelial cells placed at the bottom of the dish. Three PDEs described the VEGF, ECM and matrix metalloproteinases concentrations. Like the other

cellular Potts models the Hamiltonian (H) was used to represent the system's energy. In order to mimic the membrane extensions and retractions, the authors constantly attempted to replace the index n_i of a random lattice by the index of its random neighbours. The change in total effective energy, ΔH, that would occur if a copy were to be performed was calculated and the attempt was accepted with the Boltzmann probability:

$$P(\Delta H) = \begin{cases} e^{-\Delta H/\mu_{rm}} & if\ \Delta H \geq 0, \\ 1 & if\ \Delta H < 0, \end{cases} \tag{3.13}$$

Where μ_{rm} is the intrinsic random motility of the cell membranes. This equation allows for energetically unfavourable cell movements. In terms of chemotaxis and haptokinesis, a higher value of chemotaxis results in a faster height gain by the sprouts but does not influence the compactness or the maximum height. On the other hand, reducing the value for haptokinesis results in a slower sprout growth, less height and compactness and branching does not occur. Regarding ECM degradation, its occurrence at a faster rate produces less compact, higher and bigger sprouts with a higher degree of branching. If the degradation occurs at a slower pace, smaller and compact capillary sprouts that slowly grow towards the tumour will form. The optimal ECM density was of 0.5. Some model behaviours are in agreement with experimental studies, such as the need of matrix metalloproteinases for cell migration through 3D ECM matrices (Ghajar et al., 2006; Van Hinsbergh & Koolwijk, 2008) and also that at lower ECM densities there was no formation of sprouts and at very high densities the vasculature grows at a slower rate (Ghajar et al., 2006).

Scianna (2015) developed an extended cellular Potts model to reproduce and analyse a wound healing assay where the healing capacity of the cell population in different environments is assessed. The simulation domain is formed by 350 × 500 lattice units with a total section of 0.7mm×1mm. Firstly, the simulations were used to evaluate the healing capacity of the cell population in an isotropic collagen-free matrix. In comparison with a chemically stimulated healing process, the phenotype of a non-stimulated process was poorly invasive mainly due to a low basal cell motility. A significant invasive ability is observed upon a chemical stimulation. It was also verified that cells closer to the edge of the scratch have a high short-range motility. The author tested variations on cell-fibre adhesive strength on the invasive process of the culture concluding that higher values of cell-fibre adhesion discouraged the invasion, while moderate cell-fibre adhesion values augment the invasive capabilities of the culture. It

was also noted that the invasive capability of the culture increases with the number of fibres and when the fibres are along the horizontal direction maximal invasion occurs, filling the wound in 6 hours. As the fibre position approximates the vertical position the healing capability of the culture decreases. The theoretical results obtained by the model were compared with outcomes of wound healing assays presenting a good agreement. In the same year, Scianna and co-workers developed another extended cellular Potts model to study the reoxygenation of a hypoxic tissue simulating important features of the angiogenic process such as chemotaxis, anastomosis, branching and endothelial cells phenotypical differences. As the previous studied cellular Potts models, PDEs were included to describe the production, diffusion, uptake, decay and consumption of the VEGF-A secreted by the hypoxic tissue. This two-dimensional model simulations were carried on a regular lattice with a tissue area of 1mm^2 composed of 1000 × 1000 lattice sites where the movement of cells is resultant of an iterative stochastic energy reduction of the overall system (Hamiltonian). Iteratively at each time step of the Monte Carlo algorithm t, a lattice site $\boldsymbol{x}_s$ is randomly selected and attempts to copy its spin $n(\boldsymbol{x}_s)$ to one of its unlike neighbours $\boldsymbol{x}_t$. The model distinguishes three types of vascular cells, namely: quiescent, $\tau = Q$, tip, $\tau = T$, and stalk, $\tau = S$. Furthermore, it is also possible to the system to assume locally two different states, oxygenated and hypoxic. The tip cell behaviour is then described by a Boltzmann-like probability function:

$$P\big(n(\boldsymbol{x}_s) \to n(\boldsymbol{x}_t)\big)(t) =$$

$$\begin{cases} \tanh\left(T_{\sum_{n(x_s)}}(t)\right) \min\left\{1, exp\left(\dfrac{-\Delta H + w_{pol}}{T_{\sum_{n(x_s)}}(t)}\right)\right\}, if\ \tau\left(\sum_{n(\boldsymbol{x}_s)}\right) = T; \\ \tanh\left(T_{\sum_{n(x_s)}}(t)\right) \min\left\{1, exp\left(\dfrac{-\Delta H}{T_{\sum_{n(x_s)}}(t)}\right)\right\}, if\ \tau\left(\sum_{n(\boldsymbol{x}_s)}\right) = \{Q, S\}; \\ \tanh\left(T_{\sum_{n(x_t)}}(t)\right) \min\left\{1, exp\left(\dfrac{-\Delta H}{T_{\sum_{n(x_t)}}(t)}\right)\right\}, if\ n(\boldsymbol{x}_s) = 0, \end{cases} \tag{3.14}$$

The term ΔH is the net difference of the Hamiltonian due to proposed change of the domain configuration and $T_{\sum_{n(x_s)}}(t) \in \mathbb{R}_+$, where $\boldsymbol{x} \in \{\boldsymbol{x}_s, \boldsymbol{x}_t\}$ represents the Boltzmann temperature. Thus, $T_{\sum_{n(x_s)}}$ measures the agitation rate of the moving cell, either in extension $\left(\tau\left(\sum_{n(x_s)}\right) = \{Q, S, T\}\right)$ or in retraction $(n(\boldsymbol{x}_s) = 0)$. The term w_{pol} describes the directional persistent movement of polarized cells which alters the probability assign to each spin update as:

$$w_{pol}\left(n(\boldsymbol{x}_s) \rightarrow n(\boldsymbol{x}_t)\right) = k_{pm} \frac{\boldsymbol{p}_{\sum n(x_s)}}{\left|\boldsymbol{p}_{\sum n(x_s)}\right|} \cdot (\boldsymbol{x}_t - \boldsymbol{x}_s) \tag{3.15}$$

Where k_{pm} is the magnitude of the cell persistent movement and $\boldsymbol{p}_{\sum n(x_s)}$ is the polarity vector of the extending tip cell (Scianna et al., 2015). The model was able to capture the production of VEGF-A in response to hypoxia and endothelial cell differentiation to a stalk or tip phenotype according to the delta-notch signalling. Also, tip cell migration along VEGF-A gradients and the branching phenomena were captured. Indeed, the inclusion of various fundamental angiogenic phenomena lead to the simulation of a realistic capillary network.

Discrete models can effectively describe individual cell behaviour and allow for the creation of morphologically realistic vascular network patterns. Nevertheless, there are still some disadvantages regarding this type of modelling approach such as the elevated computational cost and limitations at tissue scale representations. The development of hybrid models allows to couple the best of both discrete and continuous modelling approaches.

3.1.3. Hybrid Models

Hybrid models combine cell level descriptions with tissue level descriptions. This type of modelling approach allows the integration and interaction of several temporal and spatial scales. Both individual cell behaviours and chemical species evolution can be predicted simultaneously. Milde et al. (2008) developed a three-dimensional model of sprouting angiogenesis (tumour induced) which combined a continuum description of VEGF, fibronectin, endothelial stalk cell density and matrix metalloproteinases with a cell-based approach for tip-cells. In other terms, molecular species are governed by reaction-diffusion equations and are represented by their concentrations while migrating tip cells are represented by particles. Also, newly formed capillaries are represented by the endothelial cell density. This was the first sprouting angiogenesis model to include the ECM structure effect on the network morphology while also considering different chemoattractant isoforms. A tumour was the source of soluble VEGF ($sVEGF$), which diffuses through the ECM creating a chemotactic gradient, and VEGF isoforms that bind to the ECM ($bVEGF$) and do not diffuse, being locally distributed through the ECM. The $bVEGF$ can be cleaved from the ECM ($cVEGF$) by matrix metalloproteinases released from migrating endothelial cells. Matrix-bound VEGF is regulated by:

$$\frac{\partial[bVEGF]}{\partial t} = -\lambda_c[MMP][bVEGF] \tag{3.16}$$

Where $[bVEGF]$ and $[MMP]$ are the concentrations of matrix-bound VEGF and metalloproteinases, respectively, and λ_c is the cleaving rate. The $cVEGF$ and $sVEGF$ evolution is given by:

$$\frac{\partial[cVEGF]}{\partial t} = D_{VEGF}\nabla^2[cVEGF] + \lambda_c[MMP][bVEGF] - \lambda_{EV}[cVEGF]\rho_{ECL} - \lambda_d[cVEGF] \tag{3.17}$$

$$\frac{\partial[sVEGF]}{\partial t} = D_{VEGF}\nabla^2[sVEGF] - \lambda_{ev}[sVEGF]\rho_{ECL} - \lambda_d[sVEGF] \tag{3.18}$$

Both $cVEGF$ and $sVEGF$ are subject to natural decay with rate λ_d and endothelial uptake rate of VEGF (λ_{ev}). The VEGF diffusion constant is represented by D_{VEGF} and ρ_{ECL} is the endothelial cell density lining capillary walls. The authors also considered two different states for the fibronectin, bound and unbound. Much like the VEGF when the fibronectin is in an ECM-bound state, its diffusion is inhibited. Regarding sprout tip migration, the authors assumed that chemotaxis and haptotaxis determine the migration direction and that the endothelial cell speed is influenced by the presence of fibres. Therefore, tip cell positions $\boldsymbol{x}_{i,j,k}$ are updated at each step with:

$$\frac{\partial \boldsymbol{x}_{i,j,k}}{\partial t} = \boldsymbol{v}_{i,j,k} \tag{3.19}$$

$$\frac{\partial \boldsymbol{v}_{i,j,z}}{\partial t} = \boldsymbol{a}_{i,j,k} - \lambda_{dc}\boldsymbol{v}_{i,j,k} \tag{3.20}$$

Where $\boldsymbol{v}_{i,j,k}$ is the velocity and $\boldsymbol{a}_{i,j,k}$ the acceleration at the location $\boldsymbol{x}_{i,j,k}$. The parameter λ_{dc} is the drag coefficient. In the referred model, the branching phenomena occurs in high anisotropy locations with preferred direction being determined by satellite points distributed radially around the tip cell particle. The newly formed tip cell velocity $\boldsymbol{v}'_{i,j,k}$, updates the velocity term in Eq.3.20. The direction of the new velocity is a combination of the acceleration direction at the satellite point and the direction that points from the sprout tip position ($\boldsymbol{x}_{i,j,k}$) to the satellite position ($\boldsymbol{x}_s$):

$$\boldsymbol{v}'_{i,j,k} = \frac{|\boldsymbol{v}_{i,j,k}|}{1+\beta}\left(\frac{\boldsymbol{a}_{i,j,k}}{|\boldsymbol{a}_s|} + \beta\frac{\boldsymbol{x}_s - \boldsymbol{x}_{i,j,k}}{|\boldsymbol{x}_s - \boldsymbol{x}_{i,j,k}|}\right) \tag{3.21}$$

In this equation the parameter $\beta = 0.8$ and $\boldsymbol{a}_s$ represents the acceleration of the satellite at the position $\boldsymbol{x}_s$. The equations were solved using explicit Euler steps, implicit time steps and second-order finite differences. The model predicted that both structure

and density of the ECM has an impact on the morphology, number of branches and expansion speed. Furthermore, the presence of EMC-bound VEGF isoforms resulted in an increased number of branches and an observable effect on the sprout morphology. Indeed, the model's predictions are in agreement with observations in the literature (Davis & Senger, 2005; S. Lee et al., 2005; Ruhrberg et al., 2002; Serini et al., 2006).

Cumming et al. (2009) developed a multiscale hybrid model to study the inflammation and proliferation stages of wound healing. This two-dimensional model represented fibres with a tensorial continuum approach, cells as discrete individuals capable of proliferation and with chemotactic behaviour in response to the transforming growth factor-β where diffusion equations were used to model the chemical species. A Eulerian mesh was used for chemical and fibre species and the diffusion equations were solved on a regular grid using the finite-volume method. The transforming growth factor-β acted as the mediator for the duration of the simulation. The model suggested that a decrease in transforming growth factor-β resulted in less collagen synthesis, that less cytokine cell receptors resulted in fewer macrophages migrating to the wound and expressing less cytokine and, in terms of scarring tissue, when the transforming growth factor-β receptors are blocked, the tissue becomes closely isotopically aligned. The authors compared the solution with other *in silico* models and had good agreement in results. Machado and co-workers modelled endothelial cell chemotaxis due to VEGF and haptotaxis due to ECM gradients (Machado et al., 2011). This model's modelling approach was based in the model by McDougall et al. (2006) to study tumorous angiogenesis, however, Machado et al. (2011) adapted the model to study angiogenesis in the context of wound healing, namely the regeneration of circular lesions in rodents. The mathematical model assumed that endothelial cell migration occurs through random motility, macrophage derived VEGF and haptotaxis. Endothelial cell conservation is controlled by:

$$\frac{\partial \rho_{ec}}{\partial t} = \mu_{ec}\nabla^2\rho_{ec} - \nabla\cdot\left(\frac{\chi_{ec}}{1+s_{C_{VEGF}}}\cdot\rho_{ec}\nabla C_{VEGF}\right) - \chi_h\nabla\cdot(\rho_{ec}\nabla C_{ECM}) \tag{3.22}$$

In this equation ρ_{ec} represents the endothelial cell density, χ_{ec} and $\chi_h$are respectively, the endothelial cell chemotaxis and haptotaxis coefficients, μ_{ec} is the endothelial cell random motility coefficient, C_{ECM} and C_{VEGF} the concentrations of the ECM and VEGF respectively, and finally $s_{C_{VEGF}}$is the endothelial cell chemotactic receptor saturation factor. The above equation can be discretised, allowing for individual

sprout tips migration to be governed by their local environment. The following equations complete the hybrid PDE-discrete system:

$$\frac{\partial C_{VEGF}}{\partial t} = -\lambda_{ev} \varsigma C_{VEGF} \tag{3.23}$$

$$\frac{\partial C_{ECM}}{\partial t} = \lambda_{mp} \varsigma - \lambda_{md} C_{ECM} \tag{3.24}$$

$$\frac{\partial \rho_{MMP}}{\partial t} = \lambda_{MMPr} \varsigma + D_{MMP} \nabla^2 \rho_{MMP} - \lambda_{MMPd} \tag{3.25}$$

The terms λ_{ev}, λ_{mp}, λ_{md}, λ_{MMPr} and λ_{MMPd} represent respectively the rate constants for VEGF uptake, ECM production, ECM degradation, matrix metalloproteases production and decay. The diffusion coefficient for matrix metalloproteases is represented by D_{MMP}, while their density is represented by ρ_{MMP}. Finally, the Greek letter ς is a Boolean value that indicates the presence or absence of a tip cell at a given position. To simulate blood flow through the capillaries the authors used a Poiseuille-like expression, similar to the one described in Eq.3.9. The simulation's domain was a square of 2mm with a circular wound of radius 0.6mm positioned at the centre. The *in silico* results were in great accordance concerning the temporal and spatial data of the wound area, vessel density and vessel junction densities obtained in the *in vivo* wound healing process.

Vilanova et al. (2014) created a hybrid model coupling a deterministic continuous theory with discrete random walks, allowing for the study of haptotaxis and chemotaxis in tumorous angiogenesis. The authors extended the approach by Travasso et al. (2011) and included the role of haptotaxis while also including the random walk framework. The model had a two- and three-dimensional version that contained two continuum variables, the TAF balance and a phase field that defined the location of the capillaries on the ECM. Both hypoxic and tip cells were considered discrete elements. The hypoxic cells discrete description was coupled with the continuous description of TAF balance since these cells are responsible for TAF production. Endothelial tip cells are coupled with the continuum phase field due to their proliferation. The domain's discretization was made using the Galerkin method. The model suggested that simulating with three dimensions may be the key to achieve the observed topological complexity of angiogenesis *in vivo*, and that the interaction between chemo and haptotaxis may have a crucial impact in the morphology of the vascular networks. Considering a three-dimensional *in vitro* wound model, Bookholt and co-workers developed a hybrid model to simulate the early stages of

sprouting angiogenesis. This model considered chemotaxis, random walk, cell-cell contact and durotaxis as the main forces that rule endothelial cell motility and differentiated between the interchanging tip and stalk endothelial cell phenotypes. A discrete cell-based approach modelled the cells dynamics while continuum sets of reaction-diffusion equations modelled the various proteins considered in the model: VEGF, delta-like ligand 4, matrix metalloproteinase and the urokinase plasminogen activator. Chemical concentrations were obtained via the FEM. Indeed, the approximated FEM solution to the 3D diffusion-reaction equations indicate whether the cells consume or regenerate the chemicals at their spatial positions. The performed *in vitro* assay that was posteriorly compared to the model's results, aimed to assess the angiogenic response for different VEGF concentrations. When compared, the *in silico* and *in vitro* models for different VEGF concentrations present an area of sprouted perimeter in the same order of magnitude. Also, the proposed metrics of the amount of sprouting are in accordance, in a qualitative level, with the obtained *in vitro*, hence, the morphology of the sprouts were similar in both virtual and *in vitro* models (Bookholt et al., 2016).

As it was mentioned previously, computational models can also be used to predict and assess the potential of certain therapies. Hendrata & Sudiono (2019) developed a multiscale hybrid model to explore the evolution of angiogenesis and tumorous growth under a mesenchymal stem cell therapy. The authors built a four layered model accounting for changes at the molecular, cellular, tissue and extracellular scales with cancerous, endothelial, and mesenchymal stem cells were included. At the extracellular scale a set of four reaction-diffusion equations was employed to model oxygen, VEGF, ECM and matrix degradative enzyme. Such equations were solved using the finite difference method. The tissue scale models angiogenesis, capillary growth and mesenchymal cells migration. The molecular scale describes the apoptosis signalling network for endothelial cells. Finally, at a cellular scale, tumorous cells and their behaviours are modelled. The model was capable of reproducing a brush border effect as the sprouts are drawn to the maximum VEGF concentration, sprouting, branching and anastomosis patterns commonly observed in the literature (Paweletz & Knierim, 1989). Regarding endothelial cell apoptosis induced by mesenchymal stem cells, the model suggested that in three days, the percentage of surviving endothelial cells stops decreasing at around day 3. Thus, the full effect of mesenchymal stem cells can be seen within 3 days. Also, the induced endothelial cell apoptosis is density dependent. The simulation

shows a good agreement with experimental data (Otsu et al., 2009) in terms of endothelial and mesenchymal stem cell ratio of 1:1 for the first three days of treatment. The model's tumorous growth modelling was validated by a good agreement with the literature on melanoma growth during the first 12 days (Khodadoust et al., 2009; J. Wang et al., 2013). The mesenchymal stem cell therapy, according to the model, proved to be effective in suppressing tumour growth when mesenchymal cells are given in higher number.

Yangyang Wang et al. (2019) aimed to study the principles of epidermal-dermal interactions on wound healing, which lead to the development of a hybrid two-dimensional mathematical model. The subcellular element method was used to model epidermal cell dynamics, namely, keratinocytes. A continuous approach modelled the ECM, dermal fibroblasts, and immune cells. Indeed, a set of four reaction-diffusion equations modelled fibroblast proliferation/density, overall ECM concentration, concentration of fibroblast and ECM production activators and concentration of ECM production inhibitors. In order to couple the discrete and continuum approaches, the authors used the Level Set Method to model the epidermal basement membrane as a dynamic interface that acted as a separator of the dermis and epidermis, mimicking dermal scar formation dynamics during wound healing. This dynamic interface between the epidermis and dermis was implemented by the phase function ϕ, which is defined by:

$$\frac{\partial \phi}{\partial t} = -v\nabla\phi \tag{3.26}$$

The ϕ represents the phase function in the epidermal region ($\phi > 0$) and the dermal region ($\phi < 0$) and v is the velocity field given by:

$$v = -I\nabla(C_{ECM} - C_{ECM0}) \tag{3.27}$$

In this equation I represents the temporal changes in dermal scar thickness across the modelling time and C_{ECM} represents the ECM concentration. When $C_{ECM0}\ (x, y, t)$ is in the dermis its value is zero, while if it is on the epidermis, $C_{ECM0}\ (x, y, t)$ becomes C_{ECMS}, which is the ECM in the dermis under homeostatic conditions. When perturbing activator or signalling sources dermal homeostasis and wound repair became altered. Indeed, the model predicted that both activator and inhibitor signalling factors are crucial for proper wound repair. Furthermore, it was also suggested that the rapidly increase in the production of activators and inhibitors over the baseline homeostatic levels is critical to minimize scarring in wounds. In terms of geometry and fibrin clot effects in dermal wounds, the model made several predictions that were in accordance with the literature.

The model predicted that, regardless the wound geometry the scar tissue differed in ECM and fibroblast compositions when compared to unwounded skin, which was consistent with experimental data (Pastar et al., 2014). The scars were smaller in wide shallow wounds and in deep full-thickness wounds repair with visible scars, which is a prediction consistent with the extent literature regarding wound healing (Hinshaw & Miller, 1965; Marshall et al., 2018), also, the trajectories and healing outcomes of dermal wounds are strongly affected by the fibrin clot.

Phillips et al. (2020) developed a hybrid mathematical model with the objective of studying tumour growth. The discrete agent-based modelling approach was used to describe all the endothelial cells including their interactions with different chemicals, while also considering their phenotypic transitions. In a tissue scale, reaction-diffusion equations govern the VEGF and nutrients fields. The phenotypic transitions are defined according to the VEGF concentration and nutrients, which couples the discrete and continuum modelling approaches. The FEM was used to compute macromolecule fields at the tissue level. The authors considered that every cell was under the drag force $\boldsymbol{F}_d$, the cell-to-cell adhesive ($\boldsymbol{F}_{cca}$) and repulsive ($\boldsymbol{F}_{ccr}$) forces and finally compression ($\boldsymbol{F}_{ct}$) and resistance to compression ($\boldsymbol{F}_{rct}$) forces from the boundary. While the drag force is given by $\boldsymbol{F}_d = -\eta\boldsymbol{v}$, where the Greek letter on the right side of the expression depends on the fluid viscosity and $\boldsymbol{v}$ is the velocity, the other forces acting on the cells are proportional to the adhesion φ and repulsion potentials Ψ, which are obtained by, respectively:

$$\nabla\varphi = \begin{cases} \left(\frac{|\boldsymbol{d}|}{R_A} - 1\right)^2 \frac{\boldsymbol{d}}{|\boldsymbol{d}|}, & 0 \le |\boldsymbol{d}| \le R_A \\ 0 \end{cases} \tag{3.28}$$

$$\nabla\Psi = \begin{cases} -\left(\frac{R_N|\boldsymbol{d}|}{R^2} - \frac{2|\boldsymbol{d}|}{R} + 1\right)\frac{\boldsymbol{d}}{|\boldsymbol{d}|}, 0 \le |\boldsymbol{d}| \le R_N, \\ \left(\frac{|\boldsymbol{d}|^2}{R^2} - \frac{2|\boldsymbol{d}|}{R} + 1\right)\frac{\boldsymbol{d}}{|\boldsymbol{d}|}, R_N \le |\boldsymbol{d}| \le R, \\ 0 \end{cases} \tag{3.29}$$

In these equations $\boldsymbol{d}$ is the distance between the centre of two cells or the distance between the centre of the cell and the domain boundary. The terms R, R_N and R_A represent the cytoplasmatic, nuclear and action radii, which are all stored in each discrete endothelial cell. The tip cells move due to chemotaxis according to the "VEGF force"

$\boldsymbol{F}_{VEGF}$. The directionality of the force is according to the VEGF gradient and is modelled by:

$$\boldsymbol{F}_{VEGF}^{ij} = -\lambda_{sp}\nabla\bar{\Psi}(\boldsymbol{d}^{ij}|R_N^i + R_N^j, R^i + R^j, C_{VEGF}) \quad (3.30)$$

Where λ_{sp} is a scaling parameter, $\bar{\Psi}$ is the VEGF potential and $\boldsymbol{d}^{ij}$ represents the distance between tip cell i and the stalk cell j. The model was able to effectively capture tip cell activation and angiogenic sprouting due to hypoxia, the tumour transition from avascular to vascular, the proliferative/quiescent behaviour of tumour cells, vessel anastomosis and associated nutrient delivery and vessel occlusion and collapse. Indeed, the model contributed with a novel way to model vessel occlusion and collapse by computing the physical forces between the tumour and endothelial cells.

3.2.Discussion

Biological phenomena are very complex multiscale processes. This multidimensionality paired with the many chemical and mechanical interactions during the processes make them hard to model. Wound healing and angiogenesis are no exception. The majority of wound healing angiogenesis models are one dimensional and continuous (Flegg et al., 2010; Pettet et al., 1996a; Pettet et al., 1996b; Schugart et al., 2008). This one-dimensionality cannot accurately capture the role that the wound shape surface has in the wound healing process. Phenomena such as re-epithelization and wound closure cannot be accurately captured in 1D models. Nevertheless, one-dimensional models are simpler and analytically tractable. Gaffney et al. (2002) made use of only two variables (capillary tips and endothelial cells densities) to model wound healing angiogenesis in the dermis. This approach was possible by considering that maximal density blood vessels are more capable of supply nutrients to the wound. Despite its simplicity, the model presented qualitative features observed in cutaneous wound healing. Furthermore, it also allowed for predictions regarding the maximum density of capillary tips and endothelial cells. In this model no chemical species were considered. Most continuous models describe angiogenesis based on cells densities and chemical concentrations. In early stages of angiogenesis, when the movement of endothelial cells is governed by chemical species gradients, this is a good approach. The “snail trail” angiogenic model (Balding & McElwain, 1985) has been very influential, being used and modified throughout the years (Pettet et al., 1996a; Schugart et al., 2008) but only being used in one-dimensional approaches. Some of the reviewed models also contribute with

interesting insights that help in creating protocols for current therapies (Flegg et al., 2010; Hendrata & Sudiono, 2019) and improving their effectiveness. Other than densities and chemical species, there are mechanical forces that influence wound healing. For instance, endothelial cells extend lamellipodia and apply tractional forces on the ECM. Xue et al. (2009), in addition to the chemical species, included the forces that are applied to the ECM and considered the remodelling wound healing phase. Other than presenting qualitative results in accordance with literature, this model could be used to study wounds subjected to mechanical pressure, such as foot ulcers. Wound shapes are also an important aspect that should be considered in models because they play an important role in the healing process. Two-dimensional models are used to represent deeper wounds (dermis and epidermis) and analyse to what extend wound geometry influences the healing process. Valero et al. (2013) used a 2D model for wound closure by coupling angiogenesis with wound contraction. This model also considered different wound geometries (circular or elliptical), which differed in some aspects during the healing process. In the circular wound, hypoxia was more severe while in the elliptical wound fibroblast migration occurred earlier. The contraction rate was the same between different geometries. Literature corroborated some of the findings in this work, however, most *in vivo* studies were in animal skin, which differs from human skin. There are some aspects in wound-healing that are extremely difficult to capture in continuum models. The skin structure is one example. The achievement of such degree of complexity requires 3D models, which are more expensive (in terms of computational resources) and more analytically complex. Nevertheless, they would allow for more realistic wound geometries. Continuous models cannot describe individual cell behaviour nor accurately predict the structure of vascular network. Such capabilities are associated with discrete models. Nevertheless, continuous models are valid approaches that can provide new perspectives on wound healing and angiogenesis.

Discrete models have usually a higher spatial dimension when compared to their continuum counterpart. Furthermore, they allowed for a prediction of the vessel network structure, providing realistic vascular networks morphologies. Most discrete models involve a cell-based approach, namely the cellular automata and the cellular Potts model. Nevertheless, it is possible to develop discrete models using only a discrete stochastic probabilistic approach, as it is the case of Stokes & Lauffenburger (1991) and Callaghan et al. (2006). These stochastic models differ from the cell-based models in that the latter

involve the discretization of a continuum field, usually the chemical species. The majority of the reviewed discrete models was cell-based and considered tumorous angiogenesis rather than wound healing angiogenesis. In cell-based models, the cellular dynamics are usually characterized by decisions that minimize the total energy in the system. If a chemotaxis term is included in the energy equation, cell movement is stimulated to occur in the direction of the highest VEGF concentration (or any other chemoattractant). A very important aspect that discrete models were capable of simulating was the different endothelial cells phenotypes observed throughout the angiogenic process. For instance, the work of Scianna et al. (2015), considered three different cell phenotypes: stalk, tip and quiescent. The phenotype of the cells was defined according to the delta-notch signalling. Not only this, but the model was also able to capture anastomosis, chemotaxis and branching. Another key aspect that was successfully captured by discrete model was cell adhesion mechanics, per instance, the model by Merks et al. (2004). This model highlighted the importance of intercellular cell adhesion in the formation of the vascular network, concluding that this force is essential for a stable network formation. Also, Bauer et al. (2007) demonstrated, in their tumorous angiogenesis model, that the direction of sprout migration was predominantly determined by chemotaxis and endothelial cell adhesion to the matrix fibres. One of the main advantages of discrete models is their capability of capturing and including intra-cellular processes such as epigenetic stimulus (Peirce et al., 2004) and metabolic pathways (Bentley et al., 2008; Gevertz & Torquato, 2006). Although presenting several advantages already mentioned, discrete models cannot present a description of the whole biological process as this would require an amount of computational power that is not feasible. Thus, the development of hybrid models is an interesting approach in order to overcome the disadvantages presented by both types of modelling approach.

In general, hybrid models tend to be more complex than the previously mentioned modelling approaches, however they offer more reliable biophysical processes across length and time scales. Furthermore, they also offer the possibility of easily upscaling the model, from cell to tissue scale. A solid example of the scaling potential of hybrid models is the model by Hendrata & Sudiono (2019) which accounted the molecular, cellular, extracellular and tissue scale in order to study the effectiveness of a mesenchymal stem cell therapy. The extension to three-dimensions of some of the presented hybrid models also increase the realism of the biological phenomena representation. The importance of

3D modelling is highlighted in the modelling approach by Phillips et al. (2020) and Vilanova et al. (2014). The former developed a two-dimensional model of tumour growth that innovated in the modelling of vessel occlusion and collapse, however, the authors suspected that the proliferation of tumour cells to the third dimension could cause the model to over-predict the frequency of the collapse and occlusion events. The latter developed a hybrid model to study haptotaxis and chemotaxis in angiogenesis that had a two and three-dimensional version. The three-dimensional version demonstrated a topological complexity similar to what is find in experiments, while the two-dimensional simulation did not. There are models that present good results that are in accordance with the literature, however, there are no "perfect" models capable of simulating every aspect of the biological phenomena they aim to recreate. Regardless of the used modelling approach, it is always necessary to make certain assumptions and simplifications.

When developing a mathematical model, the biological abstraction of the phenomena is essential to decide if the scale of interest is molecular, cell, tissue or even multiscale. The number of spatial dimensions is also extremely important in order to decide which modelling approach to choose. When modelling wound-healing angiogenesis, the wound's shape and nature is extremely important to consider and can be the deciding factor on the model's spatial dimensions. There are several approaches that considered a 1D wound (Gaffney et al., 2002; Schugart et al., 2008) and there are others where the wound was considered two-dimensional (Valero et al., 2013; Vermolen & Javierre, 2012). When considering the wound in 2D it is possible to study the role that both shape, surface and depth have on wound healing. Depending on the modelling approach considered, continuous, discrete or hybrid, it is important to carefully choose the species to be included in the model. Chemical species such as VEGF, transforming growth factor-β, PDGF, oxygen, amongst others, need to be considered depending on the phenomena or processes that are to be modulated. In addition to that, decisions regarding the types of cells (endothelial cells, cancerous cells, etc.) and if their phenotype changes (tip cell, stalk cell, quiescent cell, etc.) should also be considered. Generally, the more species and interactions considered, the more complex the *in silico* model will be. Reaction-diffusion equations were the most used type of approach in order to model chemical species in all types of models (Bauer et al., 2007; Daub et al., 2013; Machado et al., 2011; Schugart et al., 2008; Vermolen & Javierre, 2012). Individual cell modelling involved the cellular Potts model (Bauer et al., 2007; Daub et al., 2013; Scianna, 2015),

the cellular automata model (Gevertz & Torquato, 2006; Peirce et al., 2004) and the simpler stochastic approaches (Callaghan et al., 2006; Stokes & Lauffenburger, 1991).

The numerical method selected to perform the numerical simulation is crucial for its success. Different models used different approaches and techniques to solve their governing equations. Per instance, McDougall et al. (2002) utilized the Euler finite difference method to solve PDEs, while Vilanova et al. (2014) utilized the Galerkin method. When the model presents a high dimensional complexity, advanced discretization should be utilized. Vermolen & Javierre (2012) utilized the FEM with triangular elements to discretize their model that included both dermis and epidermis. Bookholt et al. (2016), Phillips et al. (2020) and Valero et al. (2013) have also utilized the FEM as the method for solving the system's equations. The FEM is a mesh-dependent method that effectively can be used to simulate tumorous or wound healing angiogenesis. However, the application of meshless methods such as the RPIM in biological models has been proved effective and with advantages over mesh-dependent methods (Belinha, 2014; Peyroteo et al., 2018). Meshless methods allow to study structures with complex geometries such as biological tissues, converge faster than mesh-bound methods and allow to obtain smoother variable fields. Despite all these advantages, these numerical methods are still underexplored in the field of angiogenesis modelling. Matters regarding numerical methods will be discussed in depth in the next section.

The majority of mathematical angiogenesis models are used to gain insights on the mechanisms that rule angiogenesis. Nevertheless, mathematical models, apart from retrieving insights about wound healing and tumorous angiogenesis mechanisms should also be used to test and assess current and novel therapies. For instance, Flegg et al. (2009) investigated the effectiveness of the HBOT for chronic diabetic wounds and were able to obtain clinically relevant results regarding the effectiveness and responsiveness of this therapy. Hendrata & Sudiono (2019) also developed a model to assess the potential of a certain therapy. In this case tumorous angiogenesis was studied under a mesenchymal cell therapy and the model predicted that mesenchymal cell therapy was effective in supressing tumorous growth when mesenchymal cells are administrated in higher number. In this work, the proposed mathematical model will be used to study the influence of a VEGF releasing biomaterial in the formation of capillary networks, which can be seen as a very preliminary effort to study pro-angiogenic wound healing therapies.

The predictive capabilities of mathematical models depend on the values that are chosen for the model's parameters so, it is crucial that all of the parameters are properly sourced. Ideally, the parameters should be obtained from an experimental source, however, when the complexity of the model increases, a single *in vivo* experiment may not be enough to obtain all the desired parameter values. When this is the case, the missing parameters must be estimated. Statistical analysis are an important asset in order to correctly estimate the parameter values. In addition to that, it is important to test the robustness of the model concerning variations on those parameters and, if possible, compare the model results to an *in vivo* model.

In an ending note, is important to note that many of the modelling approaches implemented in wound-healing angiogenesis come from tumorous angiogenesis studies. The "snail-trail" model per example. It is essential to continue to transversally use the insights retrieved from different types of models to incrementally construct more complete wound-healing angiogenesis models. Finally, the results obtained via modulation must be anchored to the real world, that is, the results need good agreement with experimental measurements to be validated.

CHAPTER 4- NUMERICAL METHODS

4. Numerical Methods

The field of numerical analysis aims to provide adequate methods that allow to obtain useful, numerical solutions to mathematically formulated problems (Hildebrand, 1987). The FEM is one of the most popular numerical method and has being extensively used due to its applicability in a wide range of areas. As a mesh-based method, the FEM's domain is discretized with a finite number of elements, all interconnected between themselves forming a mesh. The simplicity of the FEM's discretization concept is its most significant advantage (Belinha et al., 2016). In a scenario of a complex geometry or when a constant update of the mesh is required, the generation of highly an distorted mesh is fairly common (Belinha et al., 2016; Dinis et al., 2007). This compromises the performance of the method. Mesh-free or meshless methods arise as potential candidates to overcome some of the difficulties presented by the FEM. When compared to the FEM, meshless methods present several advantages: higher continuity and reproducibility (due to the virtually higher order of their shape functions); re-meshing efficiency (that allows one to work with large distortions of soft materials such as skin and internal organs); the produced smoother variable fields; the freedom to locally insert nodes (which grants accurate local solutions without compromising in the computational cost); and finally, meshless methods present faster convergence rates (Belinha, 2014; Belinha et al., 2016). In order to simulate endothelial cell migration during angiogenesis, the presented model in this work inserts new nodes and/or changes the position of the existing ones, which causes mesh distortion, therefore, meshless methods are indicated to efficiently handle such problem. Also, meshless methods allow to model any phenomenon governed by differential equations, like sprouting angiogenesis. In this work, the meshless method used will be the RPIM.

4.1. Radial Point Interpolation Method

The Radial Point Interpolation Method (J. G. Wang & Liu, 2002) emerged as an evolution to the Point Interpolation Method in the instance that it added radial basis functions for the solution of partial differential equations. The RPIM combines the Galerkin weak form with radial basis functions, forming a radial Point Interpolation Method (J. G. Wang & Liu, 2002). Contrarily to the Point Interpolation Method, in the RPIM the interpolation is carried out within an influence domain instead of a global

domain, the node distribution in an influence domain is unstructured and the sparse matrix of the system makes it more suitable for problems that involve a larger scale.

In the next subsections the RPIM will be formalized, and topics such as nodal connectivity, integration and shape functions will be addressed.

4.1.1. Nodal connectivity

The RPIM is a discrete method, so the problem's domain needs to be discretized. In the RPIM, the domain $\boldsymbol{\Omega} \in \mathbb{R}^2$, bounded by a physical boundary $\boldsymbol{\Gamma} \subset \boldsymbol{\Omega}$, is completely discretized with a nodal set $\boldsymbol{N} = \{\boldsymbol{x}_1, \boldsymbol{x}_2, \dots, \boldsymbol{x}_N\} \in \boldsymbol{\Omega}$. There is no predefined nodal connectivity in meshless methods so, in the RPIM the nodal interdependency is rather imposed with the influence-domain, which is obtained after the nodal discretization. The overlap of such geometric constructions (influence-domains) allows to ultimately establish nodal connectivity. In order to obtain an influence-domain it is necessary to radially search sufficient nodes inside a fixed area or volume, depending on the considered dimensions (Belinha et al., 2016). The influence-domains size or shape variation influences the performance of the RPIM, so, according to the literature, for a two-dimensional problem it should be considered $n = [9{,}16]$ nodes inside each influence-domain (Belinha, 2014).

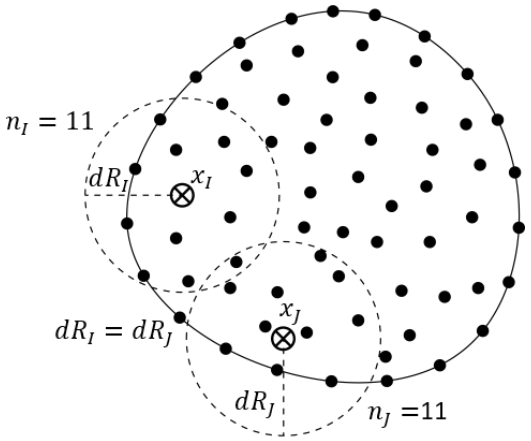

Figure 4.1-Influence-domain example for the RPIM.

4.1.2. Integration and background mesh

The RPIM requires the construction of a background integration mesh in order to perform numerical integration. Indeed, discrete numerical methods that use the Galerkin weak formulation need a background integration mesh. In order to define the background integration it is necessary to divide the domain in a regular grid forming quadrilateral

integration cells that will be filled with gauss integration points according to the Gauss-Legendre quadrature scheme (Belinha, 2014; J. G. Wang & Liu, 2002). Isoparametric interpolation functions are then used to obtain the Cartesian coordinates of the quadrature points. It is common in the RPIM to use a regular quadrature integration mesh due to its simplicity, however, in some cases, this causes the grid to be larger than the solid domain, which results in some integration points to be outside of it. So, if the grid does not completely fit the solid domain, the integration points that are outside of it need to be removed in post treatment (Belinha et al., 2016). This can be seen in Figure 4.2 d) where many of the integration points observable in Figure 4.2 c) were removed.

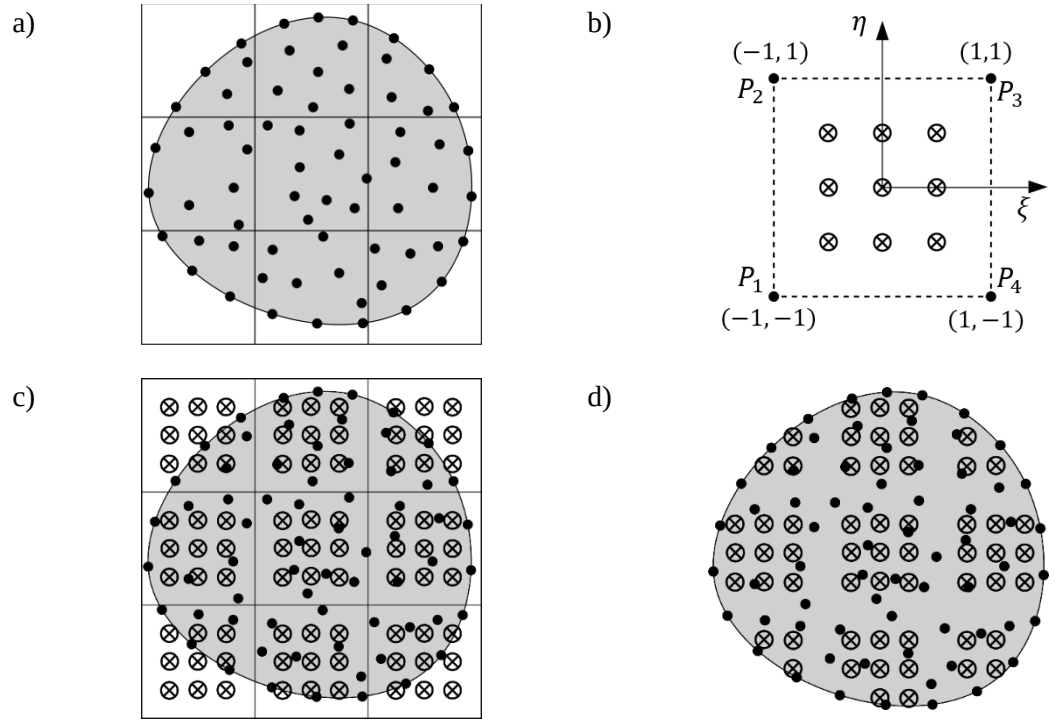

Figure 4.2-Schematic representation of the construction of the background mesh according to the Gauss-Legendre quadrature scheme. a), domain's division in a regular 3×3 square grid with the integration points. b), Gauss-Legendre quadrature 3×3 scheme. c), insertion of the Gauss points. d), final domain after post-treatment.

4.1.3. Shape functions

The RPIM uses Radial Point Interpolators (RPI) to construct the shape functions. This technique combines a polynomial basis function $\boldsymbol{p}(\boldsymbol{x})^T = \{p_1(\boldsymbol{x}), p_2(\boldsymbol{x}), \dots, p_m(\boldsymbol{x})\}$, with a radial basis function, $\boldsymbol{r}(\boldsymbol{x})^T = \{r_1(\boldsymbol{x}), r_2(\boldsymbol{x}), \dots, r_n(\boldsymbol{x})\}$, building an approximation function $u^h(\boldsymbol{x})$ that interpolates the nodal data. The interpolation function $u^h(\boldsymbol{x})$ can be defined at the specific point $\boldsymbol{x}_I$ by:

$$u^h(\boldsymbol{x}_I) = \sum_{i=1}^{n} r_i(\boldsymbol{x}_I)a_i + \sum_{j=1}^{m} p_j(\boldsymbol{x}_I)b_j = \boldsymbol{r}(\boldsymbol{x}_I)^T\boldsymbol{a} + \boldsymbol{p}(\boldsymbol{x}_I)^T\boldsymbol{b} = u(\boldsymbol{x}_I) \tag{4.1}$$

In this equation, the integers m and n correspond to the number of monomial terms of the polynomial basis and the number of nodes inside the influence-domain of the interest point $\boldsymbol{x}_I$, respectively. The non-constant coefficients of $\boldsymbol{r}(\boldsymbol{x})^T$ and $\boldsymbol{p}(\boldsymbol{x})^T$ are represented by $\boldsymbol{a}^T = \{a_1, a_2, \dots, a_n\}$ for the former, and $\boldsymbol{b}^T = \{b_1, b_2, \dots, b_m\}$ for the latter.

The RPIM can be combined with distinct radial basis functions in order to construct the shape function, however, the literature suggests that the Multiquadrics Radial Basis Function (MQ-RBF) as the most efficient (Dinis et al., 2007; J. G. Wang & Liu, 2002). Considering d_{iI} as the distance between the interest point $\boldsymbol{x}_I = \{x_I, y_I\}^T$ and a node $\boldsymbol{x}_i = \{x_i, y_i\}^T$ inside the influence domain, the MQ-RBF and d_{iI} can be defined as follows:

$$\boldsymbol{r}_i(\boldsymbol{x}_I) = \boldsymbol{s}(d_{iI}) = \left(d_{iI}^2 + c^2\right)^p \tag{4.2}$$

$$d_{iI} = \sqrt{(x_i - x_I)^2 + (y_i - y_I)^2} \tag{4.3}$$

With the variables c and p being the shape parameters of the MQ-RBF. The shape parameters can affect the efficiency of the meshless method therefore, it is extremely important to choose the adequate value for them. The literature suggests $c = 0.0001$ and $p = 0.9999$ (Belinha et al., 2016; Dinis et al., 2007). The RPI originally enforced a complete polynomial basis function, however, research works demonstrated that using a simple constant basis $\boldsymbol{p}(\boldsymbol{x}_i) = \{1\}$ increases the efficiency of the RPI formulation by reducing its computational cost while maintaining the same accuracy level (Belinha, 2014). With the usage of a simple basis, the number of monomial terms is one thus, $m = 1$. As a means to guarantee a unique solution the additional polynomial function is necessary:

$$\sum_{i=1}^{n} p_j(x_i, y_i)a_i = 0, \;\; j = 1,2, \dots, m. \tag{4.4}$$

The shape functions can be defined in a matrix form, establishing the following system of equations:

$$\begin{bmatrix} \boldsymbol{R} & \boldsymbol{P} \\ \boldsymbol{P}^T & \boldsymbol{Z} \end{bmatrix} \begin{Bmatrix} \boldsymbol{a} \\ \boldsymbol{b} \end{Bmatrix} = \begin{Bmatrix} \boldsymbol{u} \\ z \end{Bmatrix} \leftrightarrow \boldsymbol{G} \begin{Bmatrix} \boldsymbol{a} \\ \boldsymbol{b} \end{Bmatrix} = \begin{Bmatrix} \boldsymbol{u} \\ z \end{Bmatrix} \tag{4.5}$$

The letter $\boldsymbol{G}$ represents the complete moment matrix, while $\boldsymbol{Z}$ is a null matrix. The variable nodal values vector is defined by $u_i = u(x_i), \forall\{i \in \mathbb{N}: i \leq n\}$. The radial moment matrix $\boldsymbol{R}$ and the polynomial moment matrix $\boldsymbol{P}$ are represented as it follows:

$$\boldsymbol{R}_{[n\times n]} = \begin{bmatrix} r_1(x_1,y_1) & r_1(x_2,y_2) & \cdots & r_1(x_n,y_n) \\ r_2(x_1,y_1) & r_2(x_2,y_2) & \cdots & r_2(x_n,y_n) \\ \vdots & \vdots & \ddots & \vdots \\ r_n(x_1,y_1) & r_n(x_2,y_2) & \cdots & r_n(x_n,y_n) \end{bmatrix} \tag{4.6}$$

$$\boldsymbol{P}_{[n\times m]} = \begin{bmatrix} p_1(x_1,y_1) & p_2(x_1,y_1) & \cdots & p_m(x_1,y_1) \\ p_1(x_2,y_2) & p_2(x_2,y_2) & \cdots & p_m(x_2,y_2) \\ \vdots & \vdots & \ddots & \vdots \\ p_1(x_1,y_1) & p_2(x_n,y_n) & \cdots & p_m(x_n,y_n) \end{bmatrix} \tag{4.7}$$

The matrix $\boldsymbol{R}$ is symmetric ($\boldsymbol{R}_{ij} = \boldsymbol{R}_{ji}$) due to the distance being directionless.

Considering that $rank\colon(p) = m \leq n$, the solvability of the system presented in Eq.4.5 is assured (Belinha, 2014). The usage of the simple constant polynomial basis $\boldsymbol{p}(\boldsymbol{x}_i) = \{1\}$, satisfies the above-mentioned condition. The interpolation function is obtained by:

$$u^h(\boldsymbol{x}_I) = \{\boldsymbol{r}(\boldsymbol{x}_I)^T; \boldsymbol{p}(\boldsymbol{x}_I)^T\}\boldsymbol{G}^{-1}\begin{Bmatrix}\boldsymbol{u}\\ Z\end{Bmatrix} = \{\boldsymbol{\varphi}(\boldsymbol{x}_I)^T; \boldsymbol{\Psi}(\boldsymbol{x}_I)^T\}\begin{Bmatrix}\boldsymbol{u}\\ Z\end{Bmatrix} \tag{4.8}$$

The term $\boldsymbol{\Psi}(\boldsymbol{x}_I)$ is a residual scalar without relevant physical meaning and $\boldsymbol{\varphi}(\boldsymbol{x}_I)$is the interpolation function vector. In respective order, both terms are defined as follows:

$$\boldsymbol{\Psi}(\boldsymbol{x}_I) = \{\Psi_1(\boldsymbol{x}_I) \quad \Psi_2(\boldsymbol{x}_I) \quad \ldots \quad \Psi_m(\boldsymbol{x}_I)\} \tag{4.9}$$

$$\boldsymbol{\varphi}(\boldsymbol{x}_I) = \{\varphi_1(\boldsymbol{x}_I) \quad \varphi_2(\boldsymbol{x}_I) \quad \ldots \quad \varphi_n(\boldsymbol{x}_I)\} \tag{4.10}$$

Hence, the interpolation field is obtained with:

$$u^h(\boldsymbol{x}_I) = \Phi(\boldsymbol{x}_I)^T\boldsymbol{u} = \{\boldsymbol{\varphi}(\boldsymbol{x}_I)^T; \boldsymbol{\Psi}(\boldsymbol{x}_I)^T\}\begin{Bmatrix}\boldsymbol{u}\\ Z\end{Bmatrix} \tag{4.11}$$

The partial derivatives of the RPI shape functions are obtained in a direct manner. With respect to x and y, the partial derivative of interpolated field variable is:

$$\begin{cases} \dfrac{\partial u^h(\boldsymbol{x}_I)}{\partial x} = \dfrac{\partial \boldsymbol{\Phi}(\boldsymbol{x}_I)^T}{\partial x} & \boldsymbol{u} = \left\{\dfrac{\partial \boldsymbol{\varphi}(\boldsymbol{x}_I)^T}{\partial x}; \dfrac{\partial \boldsymbol{\Psi}(\boldsymbol{x}_I)^T}{\partial x}\right\}\begin{Bmatrix}\boldsymbol{u}\\ \boldsymbol{z}\end{Bmatrix} \\ \dfrac{\partial u^h(\boldsymbol{x}_I)}{\partial y} = \dfrac{\partial \boldsymbol{\Phi}(\boldsymbol{x}_I)^T}{\partial y} & \boldsymbol{u} = \left\{\dfrac{\partial \boldsymbol{\varphi}(\boldsymbol{x}_I)^T}{\partial y}; \dfrac{\partial \boldsymbol{\Psi}(\boldsymbol{x}_I)^T}{\partial y}\right\}\begin{Bmatrix}\boldsymbol{u}\\ \boldsymbol{z}\end{Bmatrix} \end{cases} \tag{4.12}$$

The partial derivative of the $\boldsymbol{r}(\boldsymbol{x}_I)$ vector is, with respect to x and y:

$$\begin{cases} \dfrac{\partial r_i(\boldsymbol{x}_I)}{\partial x} = 2p(x_i - x_I)\left(d_{iI}^2 + c^2\right)^{p-1} \\ \dfrac{\partial r_i(\boldsymbol{x}_I)}{\partial y} = 2p(y_i - y_I)\left(d_{iI}^2 + c^2\right)^{p-1} \end{cases} \tag{4.13}$$

The RPI test functions $\boldsymbol{\varphi}(\boldsymbol{x}_I)$ are dependently related to the distribution of the spread nodes while also being linearly independent in the influence-domain. It is also important to refer that such test functions have the Kronecker delta property, which allows to directly impose essential boundary conditions in the system. Furthermore, by including a polynomial basis, the RPI test functions will have reproducing and unity partition properties (Belinha, 2014).

4.2. Reaction-Diffusion Equations

The presented algorithm considers that endothelial cell migration is governed by the chemical diffusion in a homogenous medium. Since the RPIM is used as the method to obtain the systems' numerical solution, it is necessary to represent chemical diffusion as a discrete equation system. Chemical diffusion can be numerically simulated as a field problem (GR Liu & Quek, 2013), and using the general form of the Helmholtz the equation system of a two-dimensional linear steady field problem was defined:

$$D_x \frac{\partial^2 \varphi}{\partial x^2} + D_y \frac{\partial^2 \varphi}{\partial y^2} - g\varphi + Q = 0 \tag{4.14}$$

The Greek letter φ is the field variable that, in the presented angiogenesis model, corresponds to the VEGF concentration. The VEGF diffusion coefficient is represented by D_x and D_y along the dimension of x and y, respectively. The letter g is the matrix of chemical infusibility, however, in this work $g = 0$. Finally, the VEGF release rate is represented by Q. The meshless system equations were formed using the weighted residual approach:

$$\left[\boldsymbol{K}_D + \boldsymbol{K}_g\right]\boldsymbol{\Phi} - \boldsymbol{f}_q = 0 \tag{4.15}$$

making use of Eq. 4.14 it is possible to represent the variable $\boldsymbol{K}_D$ as:

$$\boldsymbol{K}_D = \int_A \boldsymbol{B}_G^T \boldsymbol{D} \boldsymbol{B}_G dA \tag{4.16}$$

where $\boldsymbol{B}_G$ and $\boldsymbol{D}$ are respectively defined by:

$$\boldsymbol{B}_G = \begin{bmatrix} \frac{\partial \varphi}{\partial x} \\ \frac{\partial \varphi}{\partial x} \end{bmatrix} = \begin{bmatrix} \frac{\partial \varphi_1}{\partial x} & \frac{\partial \varphi_2}{\partial x} & \cdots & \frac{\partial \varphi_n}{\partial x} \\ \frac{\partial \varphi_1}{\partial y} & \frac{\partial \varphi_2}{\partial y} & \cdots & \frac{\partial \varphi_n}{\partial y} \end{bmatrix} \tag{4.17}$$

$$\boldsymbol{D} = \begin{bmatrix} D_x & 0 \\ 0 & D_y \end{bmatrix} \tag{4.18}$$

Moreover, $\boldsymbol{K}_g$ and the discrete VEGF release rate vector $\boldsymbol{f}_q$ can respectively be defined as:

$$\boldsymbol{K}_g = \int_A g \{\varphi_1 \quad \varphi_2 \quad \dots \quad \varphi_n\}^T \{\varphi_1 \quad \varphi_2 \quad \dots \quad \varphi_n\} dA \tag{4.19}$$

$$\boldsymbol{f}_q = \int_A Q \{\varphi_1 \quad \varphi_2 \quad \dots \quad \varphi_n\}^T dA \tag{4.20}$$

Using the calculated parameters, it is finally possible to calculate the final VEGF concentration in the medium, $\boldsymbol{\Phi}$, which is obtained by solving Eq. 4.15.

4.3. General Algorithm

The utilized algorithm generates the influence domain of each integration point and builds the shape functions utilizing different routines. The background integration mesh was created resorting to the square integration cell coming from a regular lattice and the Gauss-Legendre quadrature 3×3 integration scheme was used. The influence domain of each integration point was established by searching 19 nodes (belonging to the nodal discretization) in the vicinity of such integration point, as suggested in the literature (Guerra, Belinha, & Natal Jorge, 2020; Guerra, Belinha, Mangir, et al., 2020). Endothelial cell movement is governed by VEGF concentration. The tip cells are placed in endothelial cell monolayer sub-domain, and they are marked using Cartesian coordinates. Then, an iterative loop begins and in each time step the tip cells are successively marked. Vector $\boldsymbol{u}$ governs the direction of the tip cell movement according to the gradient vector from the VEGF concentration field to its source. The new tip cell position is then calculated by summing the old tip cell position with the $\boldsymbol{u}$ vector multiplied by the average distance between cells also, in each iteration the $\boldsymbol{u}$ variation angle is calculated. The process stops whenever a tip cells arrives at the wound, domain boundary or if it is too close to another endothelial cell. The algorithm used in the presented work is represented in Figure 4.3.

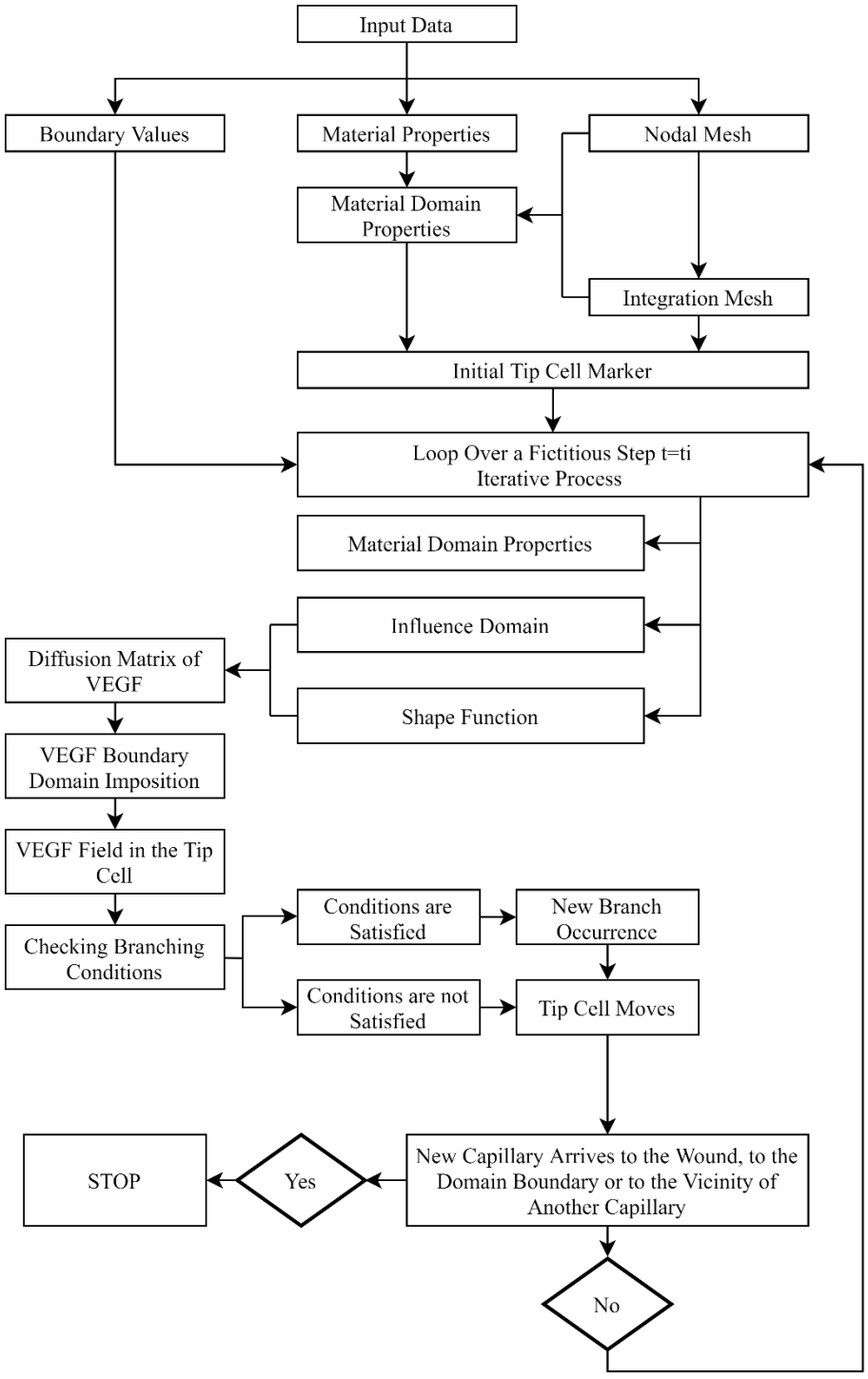

Figure 4.3- Graphical representation of the general algorithm used by the RPIM software that was used in this project.

CHAPTER 5- PRELIMINARY TESTS

5. Preliminary Tests

In this section, several tests were performed to assess the quality and robustness of the model. Firstly, simulations will only account for a single endothelial sprout migrating towards a wound then, the model's geometry will consider more wounds and more capillary sprouts. Finally, the branching event will be included and the obtained *in silico* capillary networks will be compared to images of networks obtained in a CAM assay.

5.1. Endothelial Sprout Migration

The angiogenic process was modelled in a 1 × 1 mm^2 square domain, discretized by a total of 2601 nodes (51 × 51) obtaining a regular nodal distribution. The size of an endothelial cell is, on average, about 20µm. By dividing the domain length (1mm) by the number of nodes on the x axis (51) the obtained size of each node is of 19.6µm. These dimensions allow each node to represent an area that is approximately the size of one endothelial cell. Four different regions are considered in the domain's geometry: the vessel lumen, the monolayer of endothelial cells, the ECM and finally the wound. Endothelial tip cells are also considered. The geometry of the referred zones is customizable, being possible to manipulate their shape and position in the domain recurring to Cartesian coordinates. Figure 5.1 represents an example of a possible model geometry.

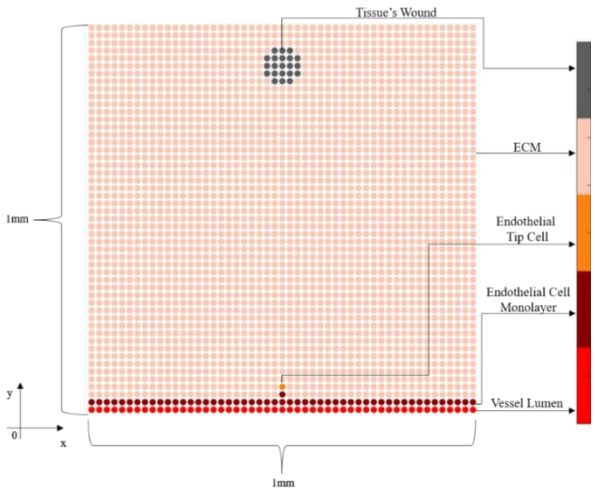

Figure 5.1- Example of a domain geometry. Each different area is represented by a different colour presented in the coloured bar. Red represents the vessel lumen while the darker red is the monolayer of endothelial cells. In the centre of the endothelial cell monolayer, there is an orange dot which represents a tip cell. The ECM is represented by pink and the wound is represented by the grey colour.

The essential chemical boundary conditions used are the VEGF basal concentration in the lumen vessel and the VEGF concentration in the wound. The natural boundary condition is the VEGF chemical diffusion coefficient. All the VEGF concentration values were obtained from the literature (Karayiannakis et al., 2003; Vermolen & Javierre, 2012). Table 5.1 contains the values for the mentioned parameters as well the source from which they were retrieved.

Table 5.1- Values used for the VEGF basal and wound concentration and VEGF diffusion concentration.

Parameter	**Value**	**Source**
Basal VEGF concentration	2.35×10^{-13} g mm^{-3}	Karayiannakis et al., 2003
VEGF concentration on the wound	6.43×10^{-13} g mm^{-3} 5.00×10^{-13}g mm^{-3}	Karayiannakis et al., 2003
VEGF diffusion concentration	1.16×10^{-6} mm^{2}s^{-1}	Vermolen & Javierre, 2012

Endothelial cell migration due to the chemotactic response upon the release of a chemoattractant (VEGF) reflects a random walk behaviour (Alt, 1980; Sleeman & Wallis, 2002). To account for this factor, the performed simulations use a random parameter that randomizes the movement of the endothelial tip cells. Figure 5.2 a) represents the VEGF diffusion gradient which goes from dark blue to yellow, where the former corresponds to the endothelial cell monolayer (basal VEGF concentration) and the latter the wound. It is observable that the concentration of VEGF is at its highest next to the centre of the wound and that, as the distance from the centre increases, VEGF concentration decreases. During the simulation, the VEGF diffusion rate was constant. Figure 5.2 b) demonstrates some steps of the endothelial cell migration guided by the tip cell. The image shows that the tip cell migrates from the endothelial cell monolayer (dark red colour) towards the location with the highest VEGF concentration, the wound (grey colour). As the tip cell goes onward towards the wound, endothelial cells follow and elongate the vascular sprout. Moreover, it is also observable the deviation of the tip cell towards the wound in the later phases of the migration. The tip cell was located at 0.1 mm in the x axis.

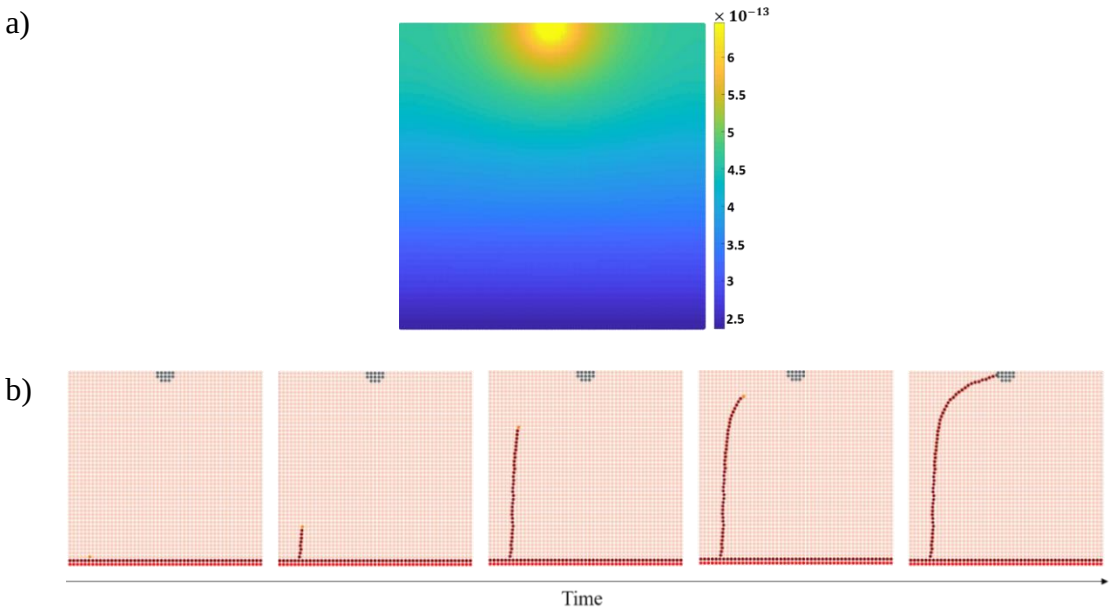

Figure 5.2- Tip cell migration due to a wound releasing VEGF at the top-middle of the domain. a) VEGF diffusion gradient (VEGF concentration in g mm^{-3}). b) tip cell migration profile at different stages with random motion in a regular nodal discretization mesh. The tip cell position is at x = 0.1 mm.

Figure 5.3 represents the results obtained for the simulation of the triple tip cell sprouting. The position of the wound was different in each simulation with six different locations tested. In every test the tip cell migrated from the endothelial cell monolayer towards the VEGF stimulus (wound) according to the chemoattractant gradient (Figure 5.3 a, c). In the centre and top-middle simulations in Figure 5.3 b), where the wound was located at the middle of the abscissa axis, the tip cells placed at x = 0.24 mm and x = 0.76 mm bent towards the wound. This happens due to the increase in VEGF concentration near the wound. The bending is also notable in the remaining tests, with special emphasis in the middle-right and middle-left simulations in Figure 5.3 d), where the tip cell further away from the wound (x = 0.24 mm and x = 0.76 mm respectively) makes an accentuated arch towards the location where the VEGF concentration is superior.

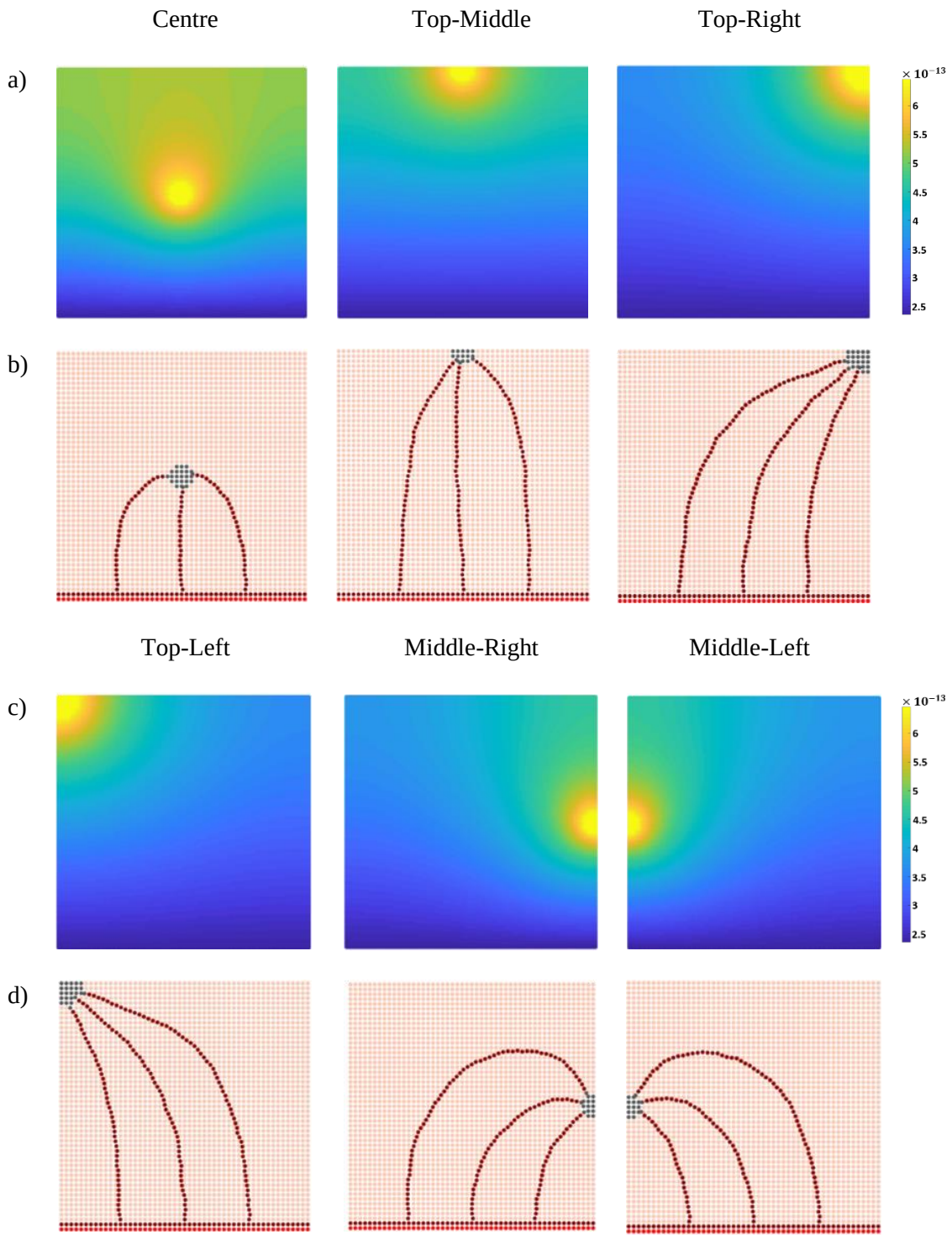

Figure 5.3- Triple tip cell migration with random motion in a regular nodal discretization mesh. a), VEGF diffusion gradient (VEGF concentration in g mm^{-3}). b), cell migration pattern towards the wound releasing VEGF in centre, top-middle and top-right locations. c), VEGF diffusion gradient (VEGF concentration in g mm^{-3}). d), cell migration pattern towards the wound releasing VEGF in top-left, middle-right and middle-left locations. The tip cells were located at x = 0.24 mm, x = 0.5 mm, and x = 0.76 mm.

Figure 5.4 contains the obtained results for the triple tip cell migration pattern with the influence of two wounds with equal VEGF concentration. In every simulation, the tip

cell migration occurred from the endothelial cell monolayer towards the wound, according to the VEGF gradient. The non-symmetric gradient simulation shows that the tip cells at positions x = 0.24 mm and x = 0.5 mm migrated to the middle-left wound, which is in accordance to the VEGF gradient (Figure 5.4 a). As for the remaining simulations, the VEGF gradient is symmetric. Regarding the tip cell migration, upon a symmetric VEGF gradient the random motion factor influences the wound to which the tip cell will migrate to.

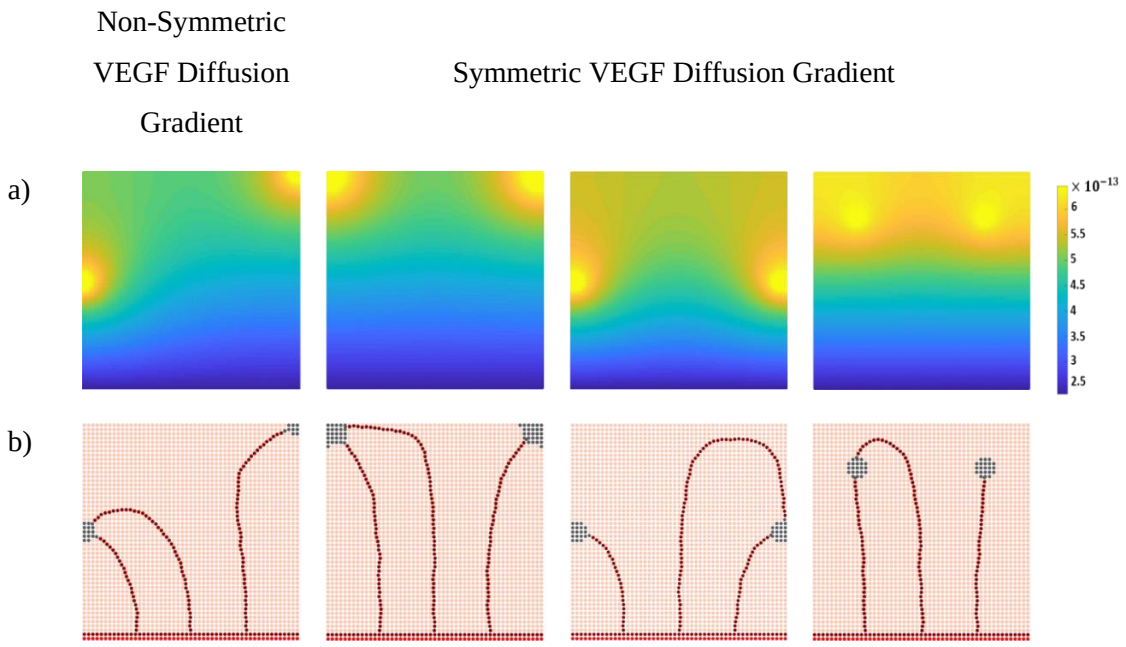

Figure 5.4- Triple tip cell migration towards two wounds releasing VEGF in different locations. a), VEGF diffusion gradient (VEGF concentration in g mm^{-3}). b), triple tip cell migration with random motion in a regular nodal discretization mesh. The tip cells were located at x = 0.24 mm, x = 0.5 mm, and x = 0.76 mm

With the purpose of exploring different biological geometries and capillary network patterns, five more simulations were performed. The results obtained are represented in Figure 5.5.

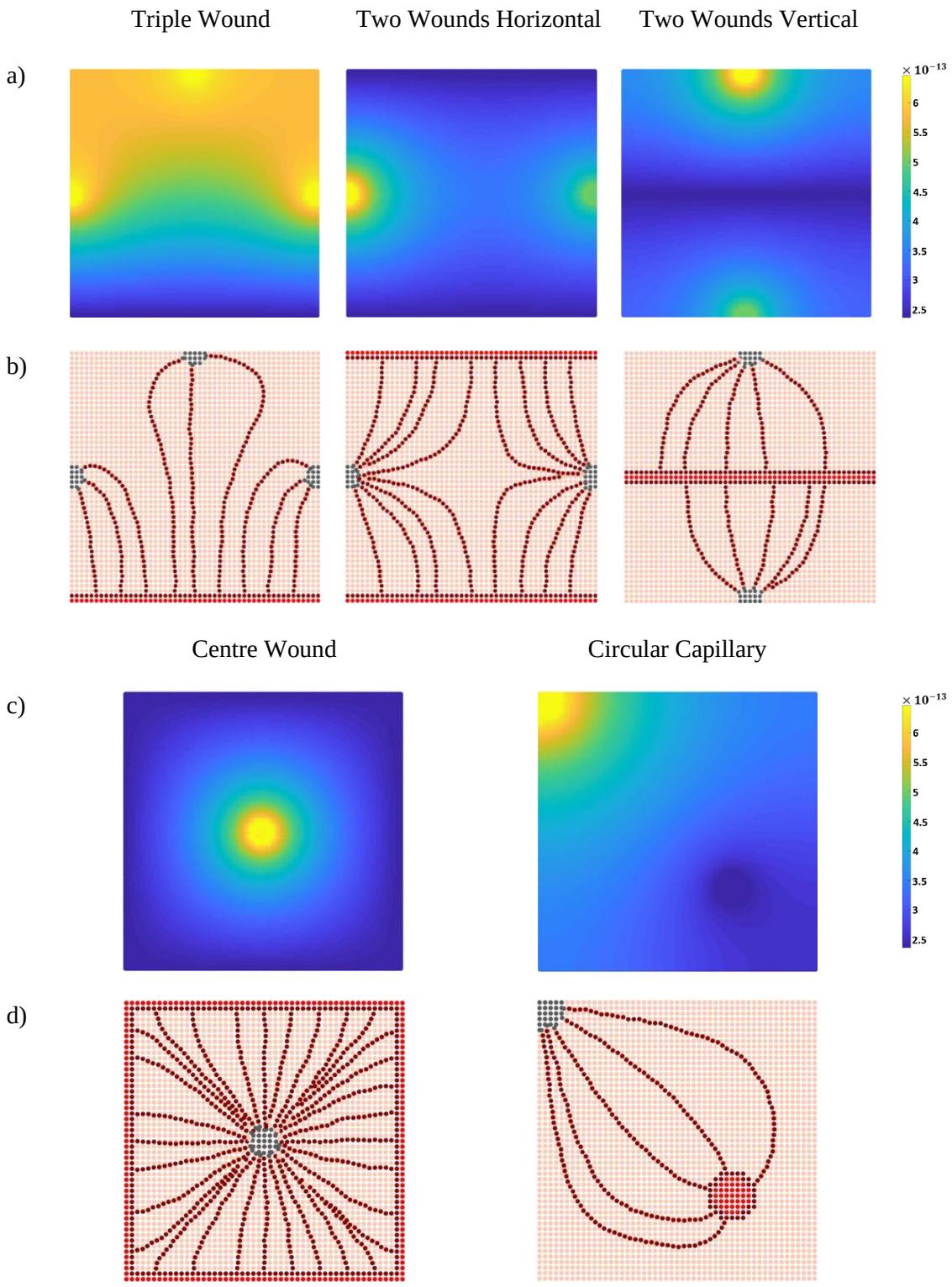

Figure 5.5- Tip cell migration pattern. a), VEGF diffusion gradient (VEGF concentration in g mm^{-3}). b), tip cell migration with random motion in a regular nodal discretization mesh. The tip cells are at random positions and the wounds differ in number, position and VEGF concentration. c) VEGF diffusion gradient (VEGF concentration in g mm^{-3}). d) tip cell migration with random motion in a regular nodal discretization mesh. The tip cells are at random positions and the wounds differ in position.

In the horizontal simulation both wounds were reached by the same number of tip cells (8) despite the wound in the middle-right having a lower VEGF concentration when compared to the middle-left. This is due to the position of the fifth tip cell (counting from the left) being closer to the middle right wound. In the circular capillary simulation tip cells migrate towards the wound according to the VEGF gradient from the endothelial cell monolayer.

5.2. Capillary Branching

The previous simulations did not include the branching event, which is a fundamental process during angiogenesis. The implementation of the branching process was made by analysing capillary networks of CAM images following the capillary order concept where the 1st order represents capillaries with the highest calibre and the 3rd order the ones with the lowest. Furthermore, the distance between consecutive branch points (d) was measured (in CAM images) to set the branching locations(Guerra et al., 2020), allowing to obtain the following equation:

$$d = 0.9286e^{-0.219 \times O_{cap}} \tag{5.1}$$

In this equation O_{cap} is the capillary order, and branching occurs if the distance to the previous branch is greater than d, for the considered order. More information regarding the model's calibration can be found in Guerra et al. (2020).

Figure 5.6 b) and c) represent the sprouting angiogenesis from one parent vessel in a regular nodal mesh. In Figure 5.6 a) the VEGF diffusion gradient for both simulations is presented. The basal, wound and diffusion VEGF values are the ones referred in Table 5.1.

It is apparent in Figure 5.6 b) and c) that the profile of the endothelial cell migration is according to the highest VEGF concentration and from the parent vessel towards the wound. Furthermore, it is also noticeable the increasing number of endothelial cells near the wound when compared to near the endothelial cell monolayer. Another geometry was tested, and the obtained results are represented in Figure 5.7.

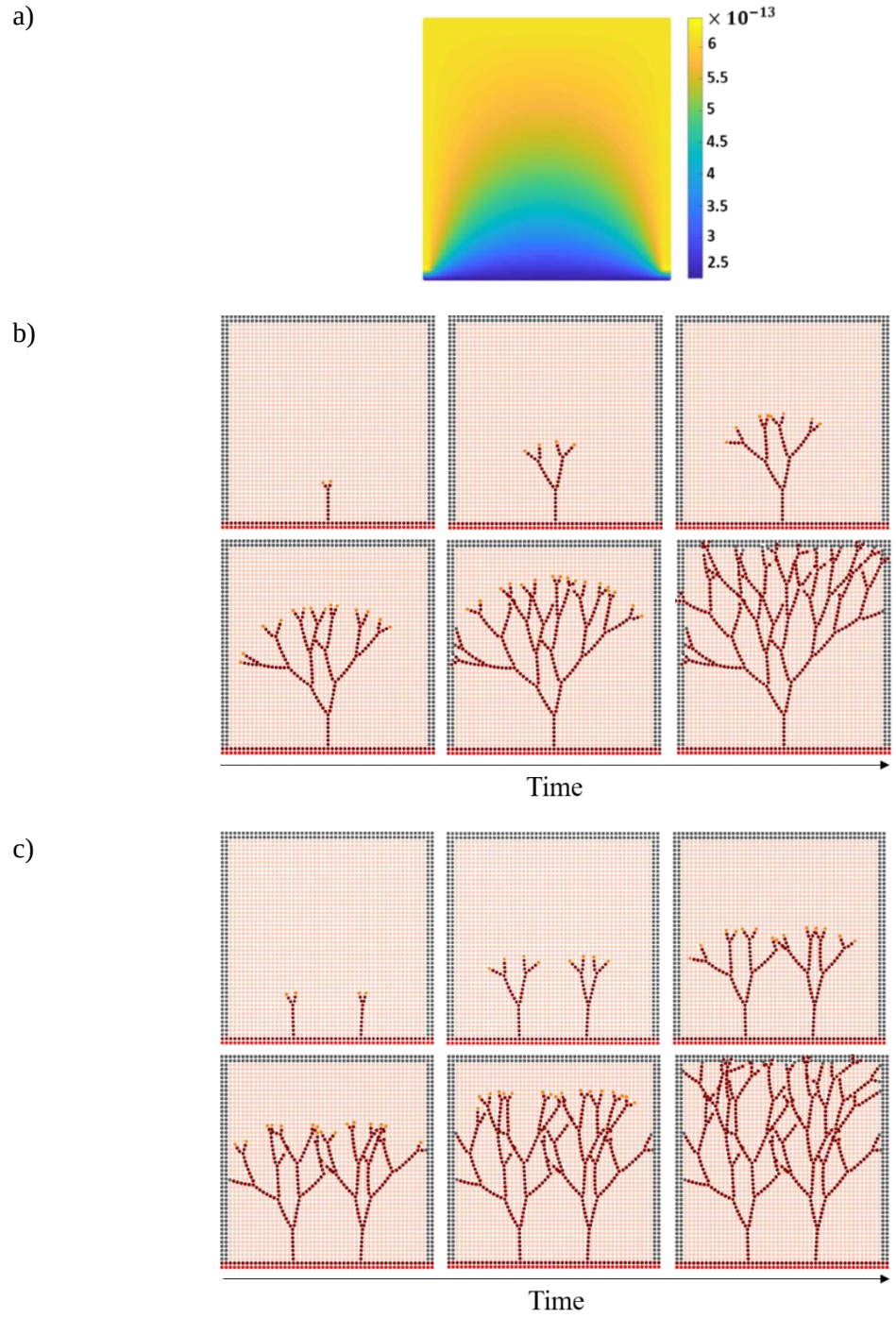

Figure 5.6- Tip cell migration pattern and formed capillary network. a), VEGF diffusion gradient (VEGF concentration in g mm^{-3}). b), tip cell migration profile at different stages in a regular nodal discretization mesh with the tip cell located at x= 0.5 mm. c), double tip cell migration profile at different stages in a regular nodal discretization mesh with the tip cells located at x= 0.36mm and x= 0.64 mm.

a)

b)

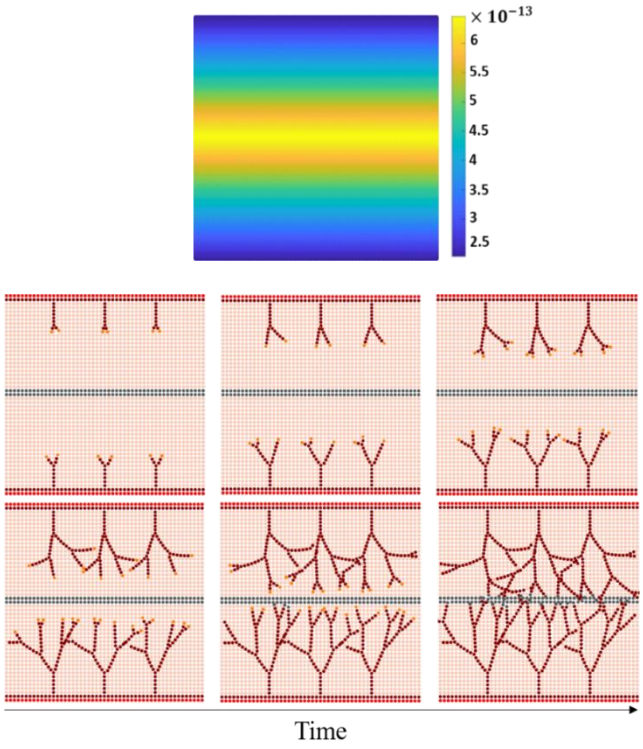

Figure 5.7- Tip cell migration pattern and formed capillary network. a), VEGF diffusion gradient (VEGF concentration in g mm^{-3}). b), tip cell migration profile from six tip cells at different stages in a regular nodal discretization mesh. The tip cells are located at x= 0.24 mm, x=0.5mm and x=0.76mm.

In Figure 5.7, tip cell migration occurred from the endothelial cell monolayer towards the wound in accordance with higher VEGF concentrations, which is in accordance with the results from *in vitro* studies regarding the VEGF role as chemoattractant of endothelial cells (Pellet-Many, 2015; Shamloo et al., 2008; Yoshida et al., 1996). Also, there are more endothelial cells near the wound. The observed formed capillary network is not symmetric. This occurrence is due to the randomized branching direction implemented in the developed model. Vessel branching occurs randomly to the left or to the right with some angle fluctuation allowed (Guerra et al., 2020).

In the literature, experimental results demonstrate an increase in sprouting in the presence of VEGF, which also implies an increased endothelial cell density (Brodsky et al., 2007; H. Wang et al., 2014; Yang et al., 2010). With the purpose of assessing if the developed model was in accordance with this fact, three simulations with different VEGF concentrations were performed. In each trial, the VEGF concentration was increased and the number of endothelial cells for each simulation was quantified. The tested VEGF concentrations were 6.43×10^{-13} g mm^{-3}, 1.286×10^{-12} g mm^{-12} and 1.929×10^{-12} g mm^{-12}. The obtained results are presented in Figure 5.8.

a)

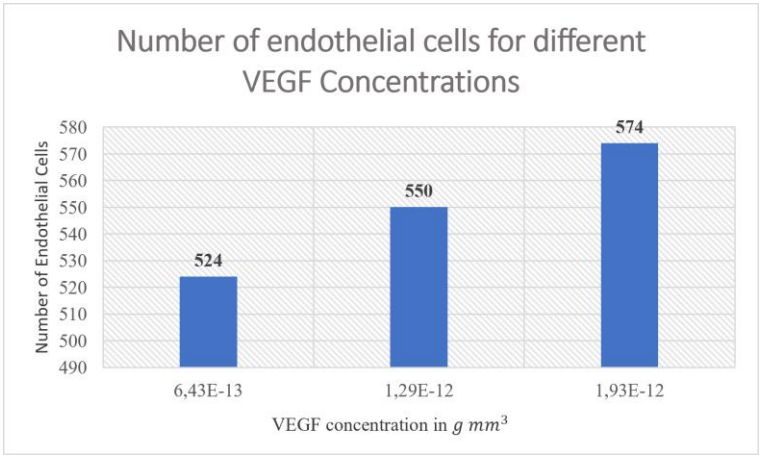

b)

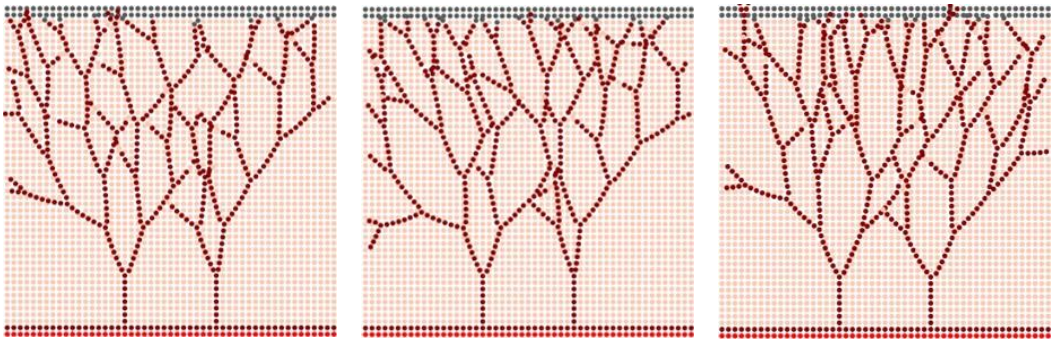

6.43×10^{-13} g mm^{-3} 1.286×10^{-12} g mm^{-12} 1.929×10^{-12} g mm^{-12}

Figure 5.8- Endothelial cell density for different VEGF concentrations. a), number of endothelial cells of the final iteration for each different VEGF concentration tested. b), resultant capillary network profiles in a regular nodal discretization mesh for the different VEGF concentrations.

As it its observable from graph in Figure 5.8 a) the number of endothelial cells increased as the VEGF concentration in the wound also increased. These results are in accordance with the experimental ones. Furthermore, all the results obtained by the presented model were in conformity with the principle of chemotaxis (Yu Wang et al., 2011) since the endothelial tip cells migrated towards the highest concentration of VEGF from the endothelial cell monolayer. Also, the random walk behaviour due to chemotactic response was accounted for.

The proposed model presents good results, however, in order to be validated, *in silico* models require comparison and accordance with *in vivo* models. Therefore, to validate the developed model, the total capillary volume fraction obtained by the simulation was compared to the one observed in selected CAM area images.

5.3. Validation of the Proposed Angiogenesis Model

As it was previously mentioned, CAM assays are currently one of the most used *in vivo* models for angiogenesis study. The CAM is an extraembryonic membrane that allows gas exchange between the embryo and the environment being highly vascularized and presenting a dense capillary network. Furthermore, its location on the top of the developing chick embryo makes it extremely accessible for experimental purposes (Mangir et al., 2019). This assay is also very cost-effective, simple, fast at producing results and allows an easy visual inspection of capillary networks (Ribatti et al., 2020). Moreover, it is useful to study the angiogenic potential of different biomaterials. The CAM images utilized in this work to validate the proposed model were kindly provided by Naside Mangir, a team member of the Professor Sheila MacNeil group from Kroto Research Institute, Department of Material Science and Engineering, University of Sheffield, North Campus, Broad Lane, Sheffield, S3 7HQ, UK.

The capillary volume fraction comparison between *in vivo* and *in silico* results was made by dividing the obtained network in a 10 × 10 grid where the capillary volume fraction in each square was quantified (Figure 5.9). Finally, the difference between the total capillary volume fraction for both the CAM image and the simulation was compared. The sprouting angiogenesis process was modelled in a 5 × 5 mm^2 square domain, discretized by a total of 2601 nodes (51 × 51) obtaining a regular nodal distribution. The domain's geometry was augmented from 1 × 1 mm^2 to 5 × 5 mm^2 in order to match the dimension of the region of interest of the CAM images. The basal, wound and diffusion VEGF values used are referred in Table 5.1 and are constant throughout time. Finally, a branching angle of 68º was used in all simulations.

In silico capillary network

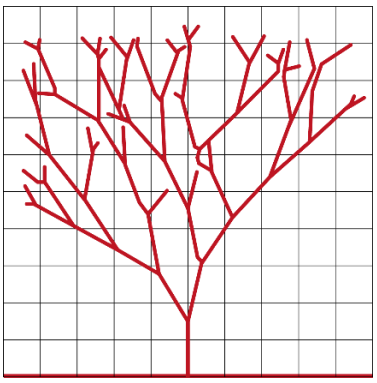

In vivo capillary network

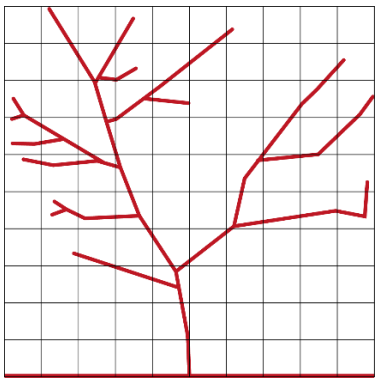

Figure 5.9- Representation of the 10 × 10 grid used for the comparison between the capillary volume fraction obtained for the *in silico* and *in vivo* results.

There were conducted three different tests where the capillary volume fraction was compared between *in silico* and *in vivo* methodologies. For each test, a different region of interest containing a capillary network was selected from the original CAM image. Then, a simulation with an identical domain geometry was performed. Finally, the capillary volume fraction of both *in silico* and *in vivo* networks was compared. Figure 5.10 represents the obtained results for the conducted tests.

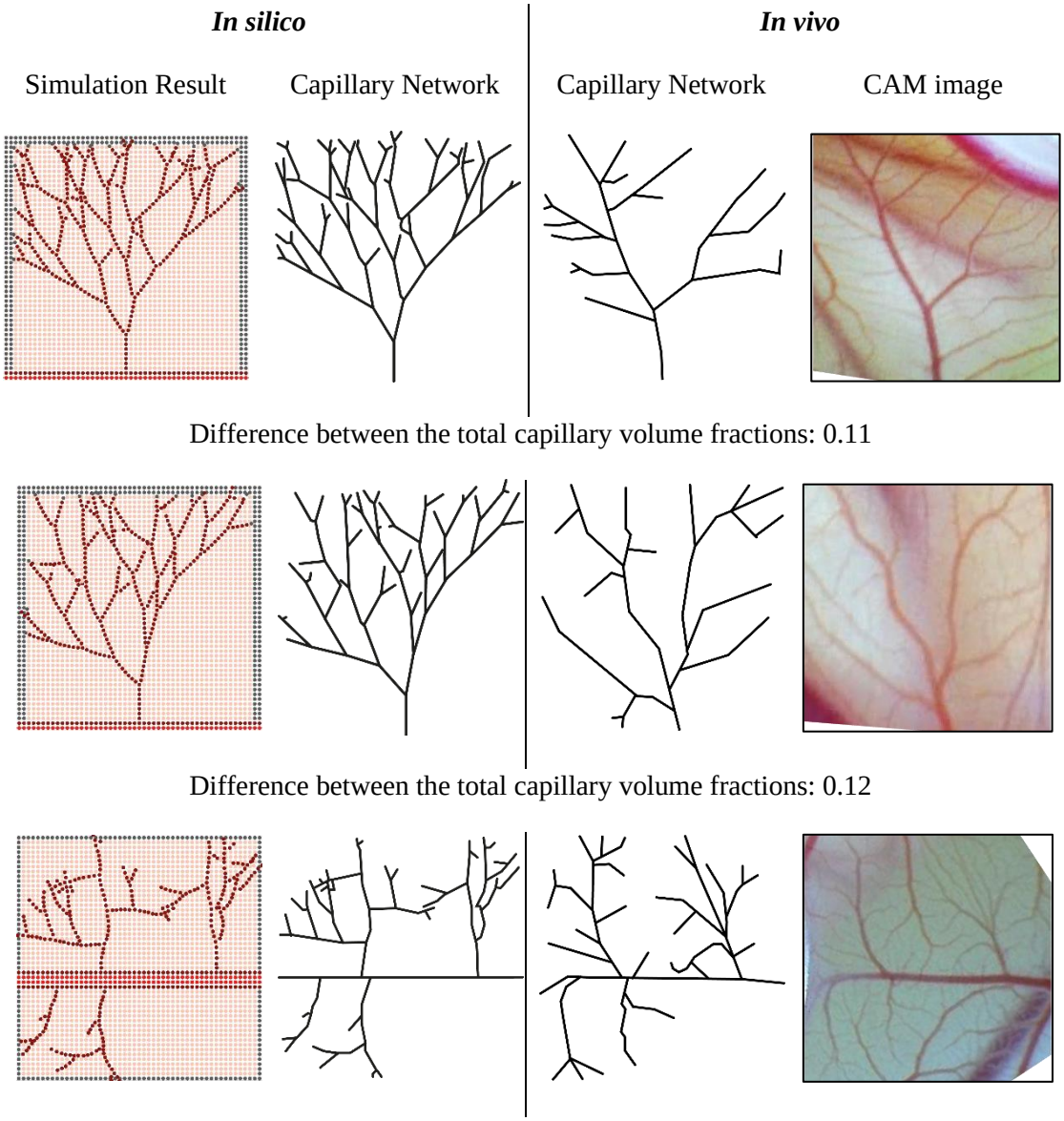

Figure 5.10- Profile of the capillary networks *in silico* and *in vivo* and respective differences between the total capillary volume fractions. Image's dimensions: 5×5 mm^2.

The resultant capillary networks from the simulations do not entirely match the networks obtained from the CAM images, however, they are alike. Considering the complexity and magnitude of the angiogenesis process and the many biological factors

involved, such differences between the capillary networks' profiles are comprehensible. Furthermore, there are several factors that exist *in vivo* angiogenesis that were not considered in the model such as the ECM mechanical stimuli. The values obtained for the difference between the total capillary volume fractions were satisfatory since the maximum difference obtained was of 15%. These results support the robustness of the developed model and assess the quality of Eq.5.1 as the branching equation. The developed model is then suited to model angiogenesis in CAM.

CHAPTER 6 – BIOMATERIAL'S ANGIOGENIC RESPONSE

6. Biomaterial's Angiogenic Response

The accuracy of the presented model has been assessed in previous section by comparison with capillary networks presented in the CAM images. This type of experimental test has been used to understand and test biocompatibility, angiogenic response and scaffolding performance of potential biomaterials. As the developed model can simulate the capillary network presented in CAM images, it is of great interest to explore the impact of a pro-angiogenic biomaterial in the formation of the capillary network and how it can compete with the wound releasing VEGF.

In this section the response of the capillary sprouts to both biomaterial and wound VEGF stimulus will be assessed. Tests were conducted for two different scenarios: one with the highest VEGF concentration in the biomaterial and the other in the wound, with some of those tests considering a variable VEGF diffusion rate in the biomaterial.

6.1. Highest VEGF Concentrations at the Biomaterial

The sprouting angiogenic process was modelled in a 5 × 5 mm^2 square domain, discretized by a total of 2601 nodes (51 × 51) obtaining a regular nodal distribution. The domain's geometry used for the biomaterial's simulations is represented in Figure 6.1.

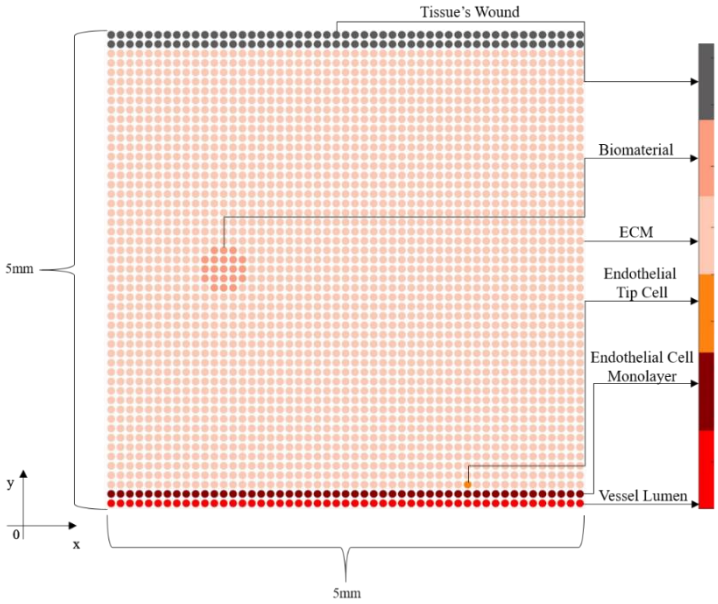

Figure 6.1- Domain's geometry for the biomaterial simulations. Each different area is represented by a different colour presented in the coloured bar. The red colour represents the vessel lumen while the darker red the monolayer of endothelial cells. The orange dot represents a tip cell that starts the sprouting process. The ECM is represented by pink and the darker pink represents the biomaterial. The wound is represented by the grey colour.

The tip cell is located at x = 3.8 mm and the biomaterial has a circular shape with a radius of 0.25mm with the coordinates of x = 1.2 mm and y = 2.5 mm. The basal, wound and diffusion VEGF values used are referred in Table 5.1. The biomaterial's VEGF concentration will be affected by an α parameter that multiplies by the wound's VEGF concentration.

$$Biomaterial\ VEGF\ concentration = \alpha \cdot \underbrace{6.43 \times 10^{-13}\ \mathrm{g\,mm^{-3}}}_{Wound\ VEGF\ concentration} \tag{6.1}$$

In the first simulations the α parameter will take values superior to 1 (100%), meaning that the VEGF concentration in the biomaterial will be superior to the concentration in the wound. Firstly, the biomaterial's concentration will be increased by increments of 5% up until 125%. From then on, increments of 25% up until 200%, doubling the wound's concentration, will be made. The VEGF diffusion rate for both wound and biomaterial is constant, not varying throughout time. In the first simulations only a single endothelial sprout migration with no branching was considered. Also, the random parameter was included. The obtained results are represented in Figure 6.2.

In Figure 6.2 a) it is noticeable that, as the VEGF concentration in the biomaterial increases, the top part of the images becomes greener with a few yellowish tones, while the circular shaped biomaterial remains yellow. Regarding the capillary tip in Figure 6.2 b) for the 105% and 110% concentrations the capillary reaches the wound but, its bending towards the biomaterial is notable. From those concentrations onwards, the capillary sprout always penetrates the biomaterial. The curve that the capillary does to reach the biomaterial flattens each time the concentration in the biomaterial increases. The curve is firstly reminiscent of a parable, however, in the third and fourth images of Figure 6.2 d) the curve is more comparable to a hyperbole since it has flattened. Considering that the concentration of the biomaterial's VEGF exceeds the wound's concentration, these results are in accordance with the chemotaxis principle since the cells migrate towards the highest VEGF concentration. The fact that in the first two images of Figure 6.2 b) the tip cell reached the wound regardless of the highest VEGF concentration on the biomaterial can be explained by the geometry used. Due to the tip cell starting the sprouting process at a considerable distance from the biomaterial, upon reaching a certain "height", the wound's VEGF influence on the tip cell was superior of the biomaterial's. This becomes clearer by observing the correspondent VEGF diffusion gradient (Figure 6.2 a and c).

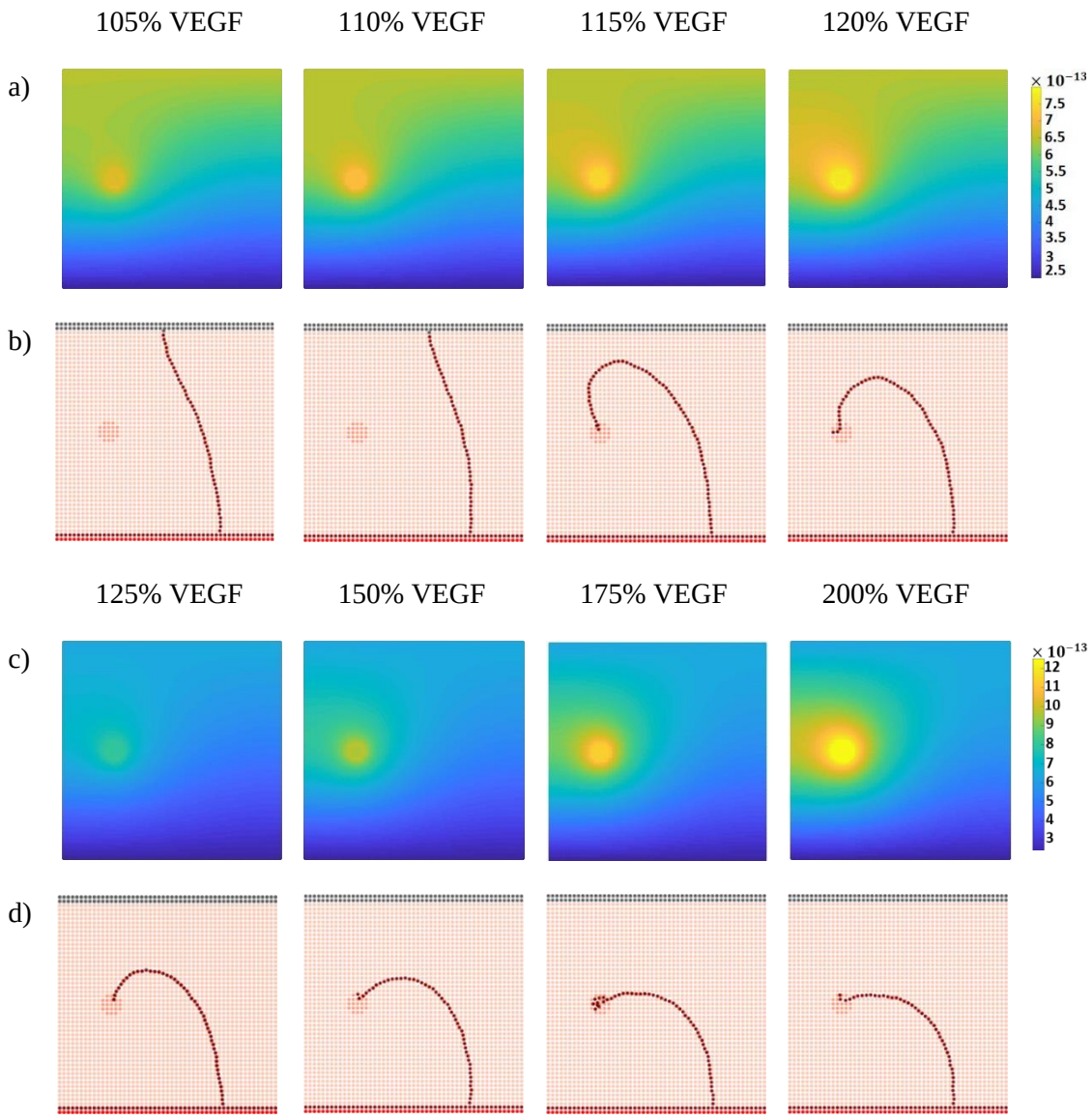

Figure 6.2- Tip cell migration pattern with the VEGF from both wound and biomaterial being diffused at a constant rate. a), VEGF diffusion gradient for the simulations of 105%, 110%, 115% and 120% of the wound's VEGF concentration (VEGF concentration in g mm^{-3}). b), tip cell migration with random motion in a regular nodal discretization mesh for the VEGF concentrations of 105%, 110%, 115% and 120%. c), VEGF diffusion gradient of 125%, 150%, 175% and 200% of the wound's VEGF concentration (VEGF concentration in g mm^{-3}). d), tip cell migration with random motion in a regular nodal discretization mesh for the VEGF concentrations of 125%, 150%, 175% and 200%. The tip cell is located at x = 3.8 mm.

6.2.Lowest VEGF Concentrations at the Biomaterial

Using the methodology that was previously applied, the endothelial cell migration when the α parameter is inferior to 1 (100%) will be evaluated. Increments of 25% in the biomaterial's concentration will be made up until 75%. Figure 6.3 contains the obtained results.

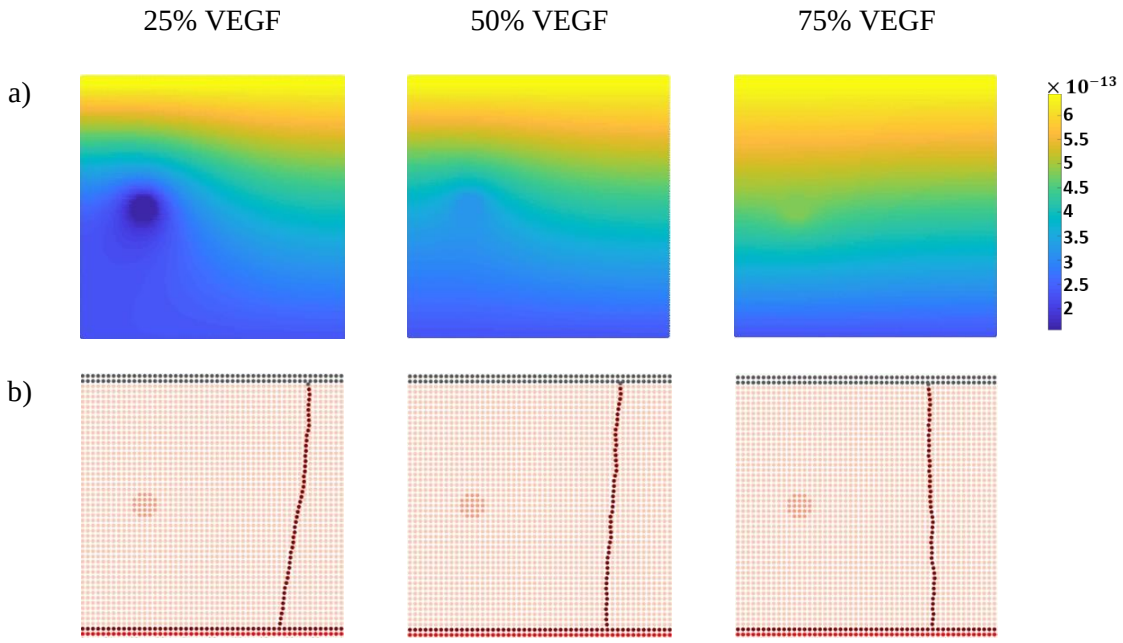

Figure 6.3- Tip cell migration pattern with the VEGF from both wound and biomaterial being diffused at a constant rate. a), VEGF diffusion gradient for the simulations of 25%, 50% and 75% of the wound's VEGF concentration (VEGF concentration in g mm^{-3}). b), tip cell migration with random motion in a regular nodal discretization mesh. The tip cell is located at x = 3.8 mm.

The obtained results were expected since for biomaterial's VEGF concentrations that were inferior or equal to 110% of the wound's concentration, the capillary sprout would go towards the wound. In the simulations presented on Figure 6.3 the capillary always reaches the wound. Observing Figure 6. 3 b), in the first image, the capillary sprout leans towards the right, which can be explained by the VEGF gradient created by the biomaterial, observable in Figure 6.3 a). As the biomaterial's VEGF concentration increases, the sprout starts to tend more and more to the biomaterial's side, which is expected since its VEGF concentration is increasing. At 75%, the sprout in Figure 6.3 b) almost follows a straight line, indicating that the VEGF concentration of the biomaterial is similar to the one presented in the wound, as it can be verified in Figure 6.3 a). The results suggest that, for the presented geometry and considered conditions, a single capillary sprout trajectory deviates from the biomaterial as long as its VEGF concentration is of 50% or inferior to the VEGF concentration of the wound. Also, it is possible to conclude that the chemotactic principle was respected.

The branching event was not included in any of the simulations until this point. In order to obtain realistic network morphologies its inclusion is necessary. Following the previous methodology, six tests with different VEGF concentrations in the biomaterial were conducted. In addition to biomaterial VEGF concentration values of 25%, 50% and

75%, values of 67%, 87% and 100% of the wound's VEGF concentration will be considered. The branching angle considered in the simulations was of 86º. Table 6.1 contains the correspondent VEGF concentration in the biomaterial for each of the performed simulations and Figure 6.4 presents the obtained results.

Table 6.1- VEGF concentrations for the biomaterial for each of the conducted tests.

25%	**50%**	**67%**	**75%**	**87%**	**100%**
1.60×10^{-13}	3.21×10^{-13}	4.30×10^{-13}	4.82×10^{-13}	5.59×10^{-13}	6.43×10^{-13}
VEGF Concentration ($\mathbf{g\ mm^{-3}}$)					

Firstly, the obtained capillary networks in Figure 6.4 present a realistic morphology. When comparing the three images in Figure 6.4 b) it is noticeable that, as the VEGF concentration in the biomaterial increases, the endothelial cells become more and more close to the biomaterial to the point that they go through it. Indeed, the capillaries are more intensely dragged to the biomaterial as its VEGF concentration increases. In Figure 6.4 d) the capillaries continue to pass through the biomaterial, however, as the VEGF concentration increases the capillaries start to penetrate the biomaterial at a lower point. In the third image, one of the capillaries is so dragged down that almost does not touch the biomaterial. In observation of the different capillary networks, it is noticeable that in lower VEGF concentrations the curve of the capillaries that grow to the side of the biomaterial was rounder and as the VEGF concentration increases the curve starts to flatten. This occurs because the biomaterial's chemoattractant effect is felt sooner by the tip cells so, they star to migrate in its direction earlier.

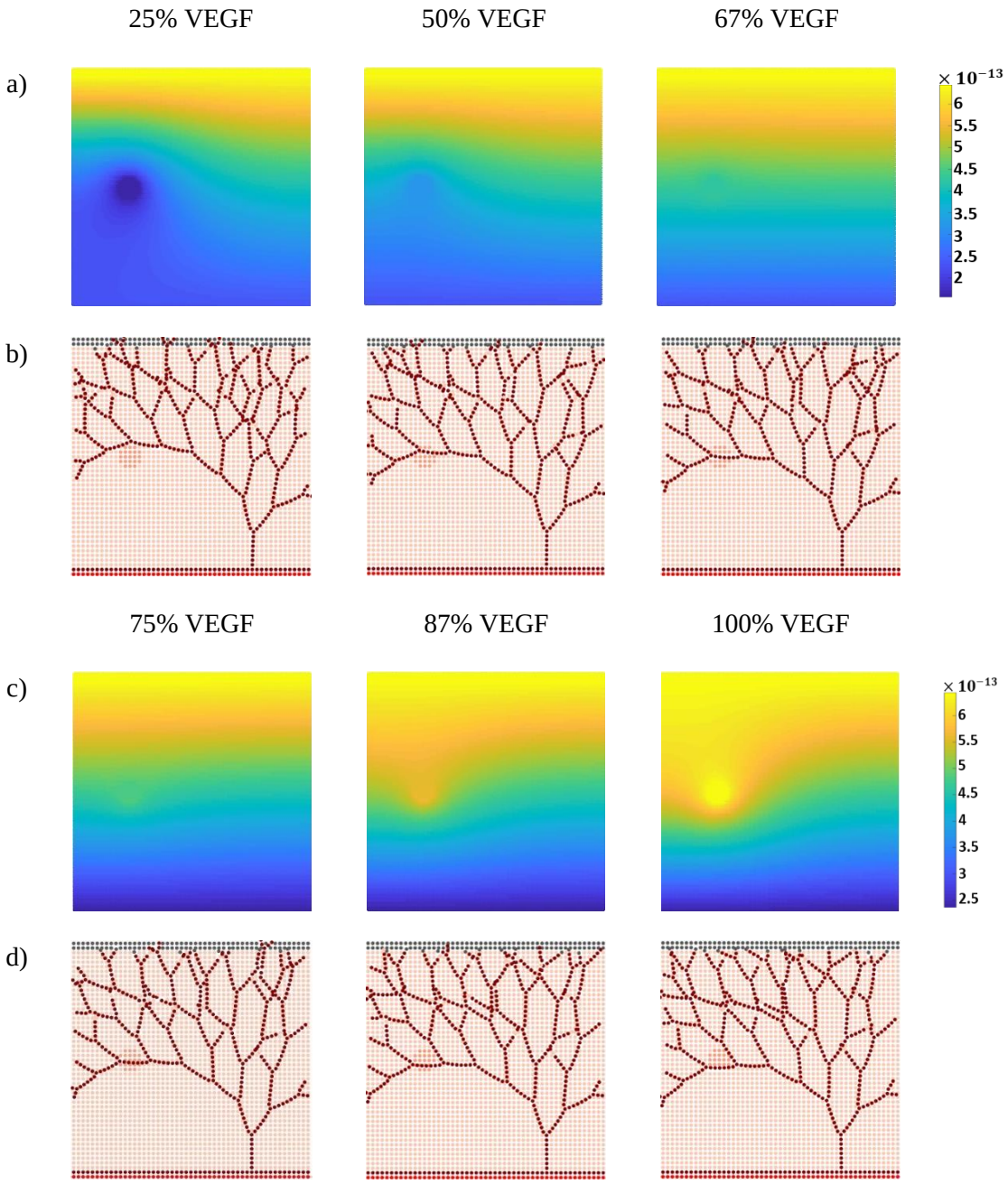

Figure 6.4- Capillary networks formed with the VEGF from both wound and biomaterial being diffused at a constant rate. a), VEGF diffusion gradient for the simulations of 25%, 50% and 67% of the wound's VEGF concentration (VEGF concentration in g mm^{-3}). b), vascular network patterns obtained for the VEGF concentrations of 25%, 50% and 67% in a regular nodal discretization mesh. c), VEGF diffusion gradient for the simulations of 75%, 87% and 100% of the wound's VEGF concentration (VEGF concentration in g mm^{-3}). d), vascular network patterns obtained for the VEGF concentrations of 75%, 87% and 100% in a regular nodal discretization mesh. The tip cell is located at x = 3.8 mm.

Analysing the VEGF gradients presented in Figure 6.4 a) and c) and the endothelial cell migration profile, it is possible to verify that the endothelial cells migrate from the parent vessel to the locations with higher VEGF concentration, following the principle of chemotaxis.

The total number of endothelial cells in each network was quantified with the purpose of understanding how the capillary network density varies with the increase in the biomaterial's VEGF concentration. Figure 6.5 represents the total number of endothelial cells for each different VEGF concentration in the biomaterial.

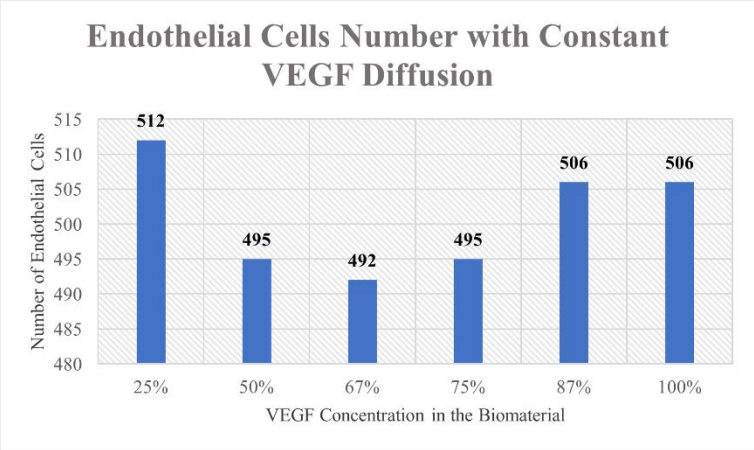

Figure 6.5- Graph representing the number of endothelial cells for each of the biomaterial's VEGF concentration. The VEGF concentration in the biomaterial is expressed relatively to the wound's VEGF concentration of 6.43×10^{-13} g mm^{-3}.

Figure 6.5 shows the highest number of endothelial cells was verified for the lowest VEGF concentration in the biomaterial. After the 25% concentration, the number of endothelial cells drops and stays fairly constant (variation of 3 endothelial cells) throughout the three following concentrations. The 87% concentration is marked by an increase in the endothelial cell number which remains the same until the 100% concentration levels. The first image in Figure 6.4 b) appears to be the denser network of the set. Indeed, in the 25% simulation more endothelial cells migrated towards the right side, creating a denser vessel network on that side when compared to the other networks. Moreover, this capillary network is the one showing a higher number of capillaries penetrating the wound. With the exception of the 25% simulation, the density of the vessel network seems to increase with the increase in biomaterial's VEGF concentration.

6.3. Variable Biomaterial VEGF Diffusion Rate

The VEGF diffusion rate was considered constant in all of the previous simulations. In this section the biomaterial's VEGF diffusion rate will vary throughout time. The capillary network morphology obtained for the simulations where the VEGF diffusion was constant in both biomaterial and wound, will be compared to the morphology obtained with a variable VEGF diffusion rate in the biomaterial for VEGF

concentrations inferior and equal to the wound's. In order to determine how the biomaterial's VEGF would vary throughout time, experimental results from CAM images were investigated. By examining the capillary growth for 12 days it was noted that between days 10 and 11 the capillaries grew approximately 0.5mm. Considering that growth period (0.5mm/day) and that the internodal distance in the presented model is 0.1mm, it is possible to obtain that 5 iterations in the model correspond to approximately 1 day. Regarding the mentioned information it is possible to develop a function that represents the variation of the VEGF concentration in the biomaterial throughout the days, $C(t)$:

$$C(t) = (C_{MAX})\frac{[cos\left(2\pi\frac{t}{\tau}\right) + 1]}{2} \tag{6.2}$$

In the defined equation C_{MAX} represents the maximum concentration of the VEGF in the biomaterial, t represents the iterations and finally τ represents the time period of 1 day so, $\tau = 5$, since 5 iterations correspond to 1 day. Figure 6.6 is the graphical representation of the above defined equation:

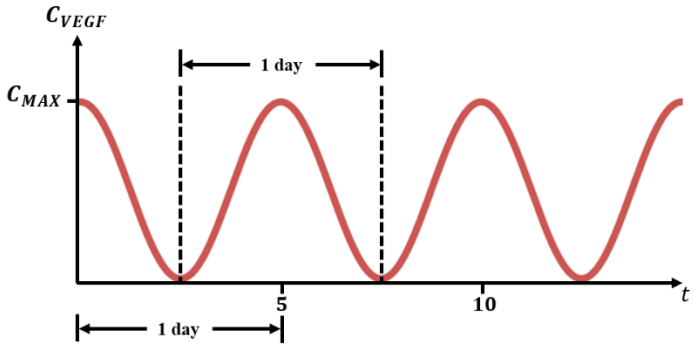

Figure 6.6- Graphical representation of Eq.6.2.

As it can be seen in Figure 6.6, the VEGF starts at a maximum concentration, corresponding to the loading of the biomaterial with VEGF by automatic pipetting. As time goes by the VEGF decays until reaching a minimum at 2.5 days. Then, the biomaterial is loaded again, with the VEGF concentration peaking at day 5. The process is repeated throughout time.

The performed simulations followed the already described methodology. The loading concentrations for the biomaterial's VEGF are of 25%, 50%, 67%, 75%, 87% and 100% of the wound's VEGF concentration. During the simulation, the VEGF concentration in the biomaterial alternated between three different values that depend on

the iteration number of the system (Eq.6.2). The three different concentrations will be referred to as maximum (loading concentration), medium and minimum. Table 6.2 contains all the possible values for the biomaterial's VEGF concentration for the six simulations.

Table 6.2- Possible VEGF concentrations for the biomaterial for each of the conducted tests.

		25%	**50%**	**67%**	**75%**	**87%**	**100%**
VEGF Concentration ($g\,mm^{-3}$)	**Maximum**	1.60×10^{-13}	3.21×10^{-13}	4.30×10^{-13}	4.82×10^{-13}	5.59×10^{-13}	6.43×10^{-13}
	Medium	1.05×10^{-13}	2.10×10^{-13}	2.81×10^{-13}	3.15×10^{-13}	3.66×10^{-13}	4.20×10^{-13}
	Minimum	1.53×10^{-14}	3.07×10^{-14}	4.11×10^{-14}	4.60×10^{-14}	5.34×10^{-14}	6.14×10^{-14}

Due to the variable VEGF diffusion rate, it is interesting to follow the evolution of the VEGF diffusion gradient and the endothelial cell migration over time. Therefore, the results will be presented at different stages (iterations). The branching angle for the simulations was of 86º and only the biomaterial had a variable VEGF diffusion rate. The obtained results for all the different loading concentrations of VEGF in the biomaterial (25%, 50%, 67%, 75%, 87% and 100%) are presented, respectively, from Figure 6.7 to 6.12.

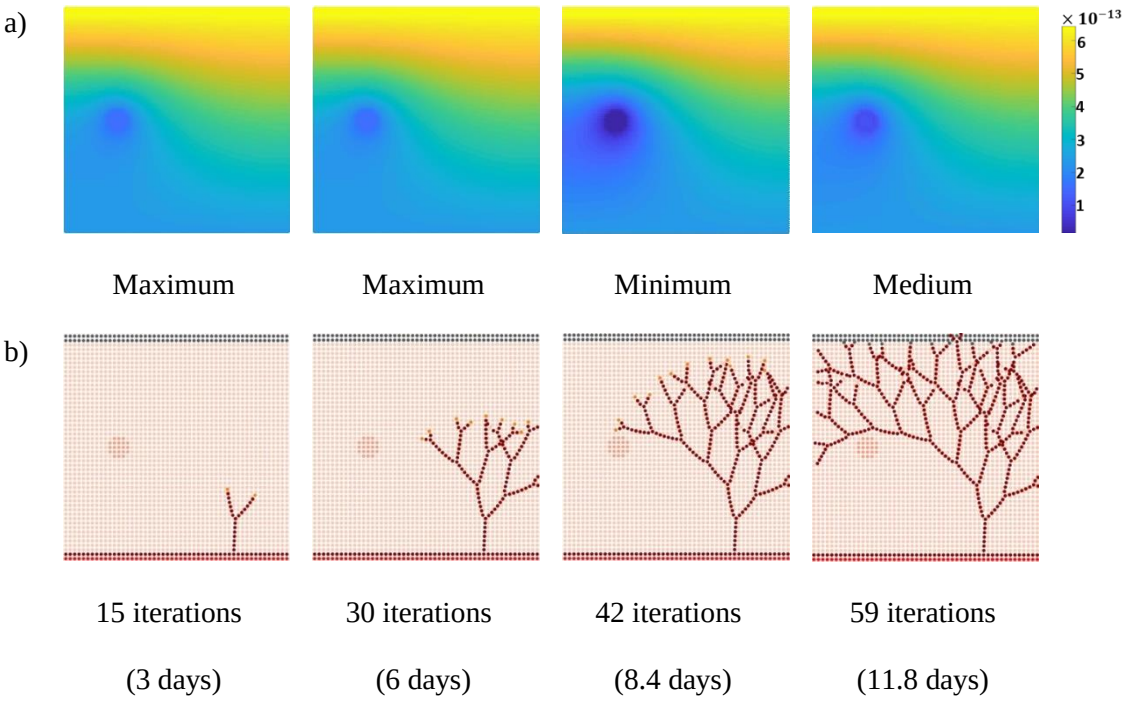

Figure 6.7- Capillary network formed with the biomaterial's VEGF being diffused at a variable rate. Biomaterial loaded with a VEGF concentration of 25% of the wound's concentration. a), VEGF diffusion gradient throughout time (VEGF concentration in g mm^{-3}). b), vascular network pattern evolution throughout time in a regular nodal discretization mesh. The tip cell is located at x = 3.8 mm.

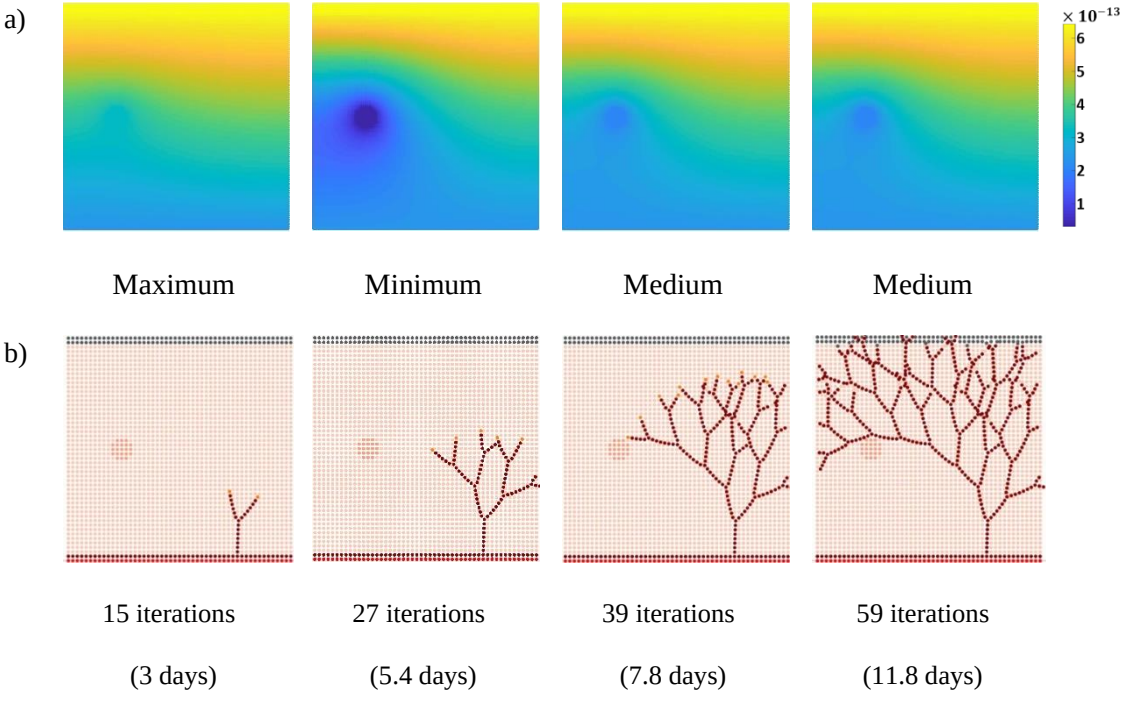

Figure 6.8- Capillary network formed with the biomaterial's VEGF being diffused at a variable rate. Biomaterial loaded with a VEGF concentration of 50% of the wound's concentration. a), VEGF diffusion gradient throughout time (VEGF concentration in g mm^{-3}). b), vascular network pattern evolution throughout time in a regular nodal discretization mesh. The tip cell is located at x = 3.8 mm.

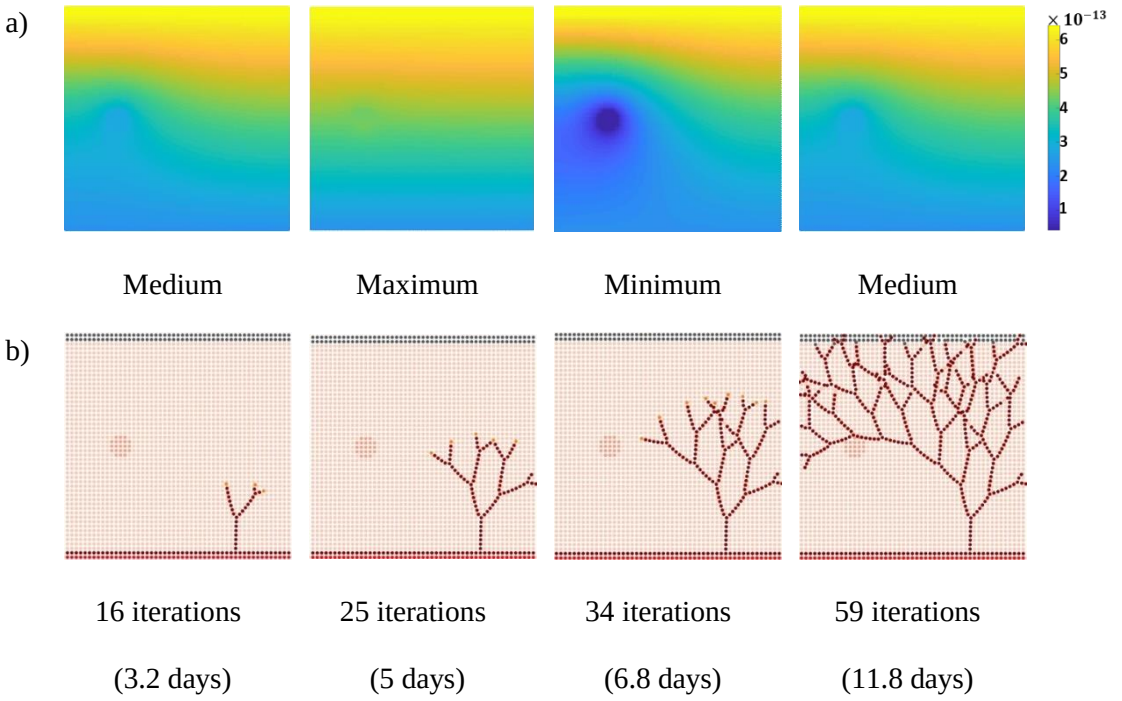

Figure 6.9- Capillary network formed with the biomaterial's VEGF being diffused at a variable rate. Biomaterial loaded with a VEGF concentration of 67% of the wound's concentration. a), VEGF diffusion gradient throughout time (VEGF concentration in g mm^{-3}). b), vascular network pattern evolution throughout time in a regular nodal discretization mesh. The tip cell is located at x = 3.8 mm.

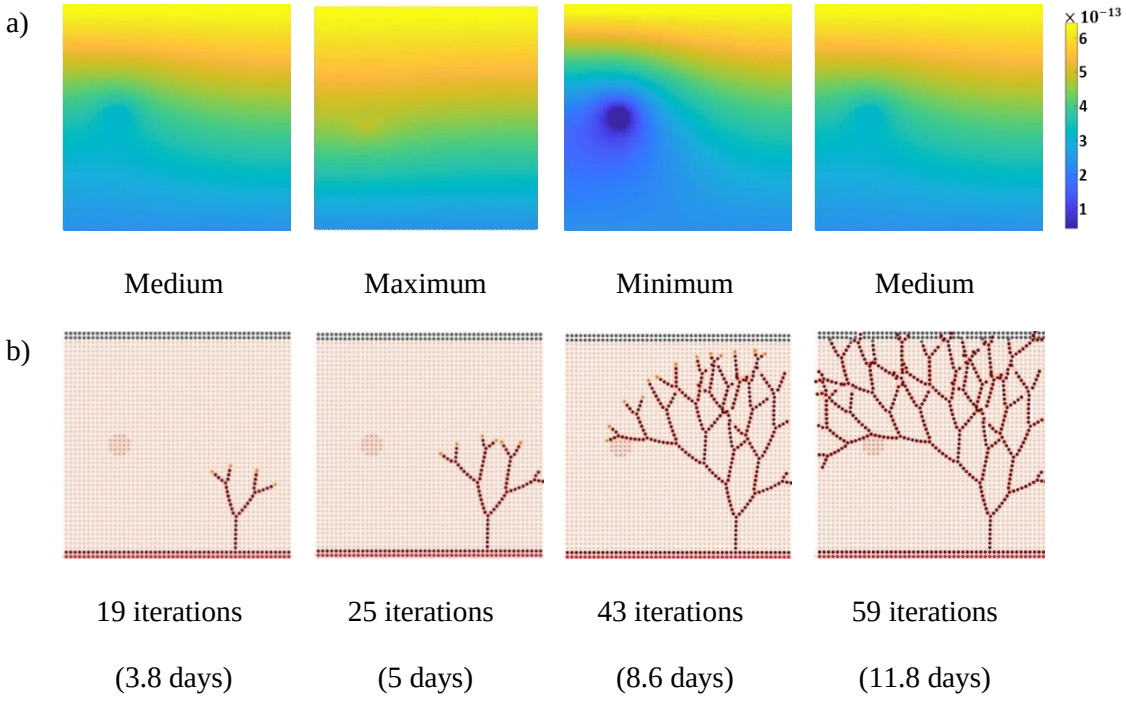

Figure 6.10- Capillary network formed with the biomaterial's VEGF being diffused at a variable rate. Biomaterial loaded with a VEGF concentration of 75% of the wound's concentration. a), VEGF diffusion gradient throughout time (VEGF concentration in g mm^{-3}). b), vascular network pattern evolution throughout time in a regular nodal discretization mesh. The tip cell is located at x = 3.8 mm.

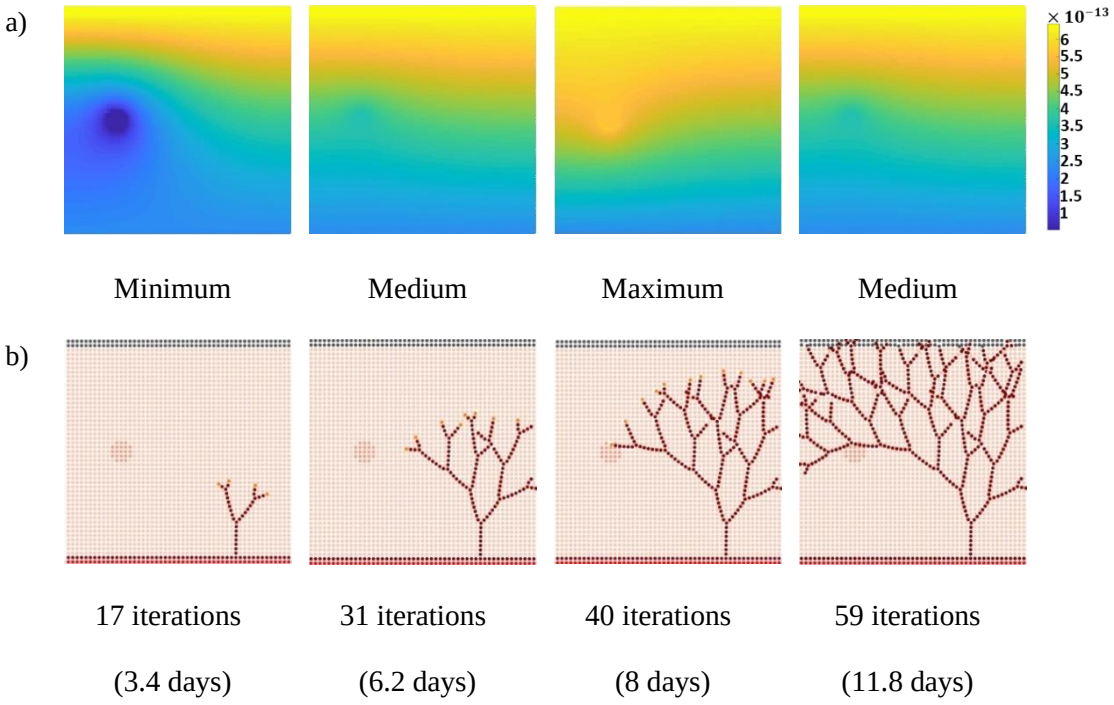

Figure 6.11- Capillary network formed with the biomaterial's VEGF being diffused at a variable rate. Biomaterial loaded with a VEGF concentration of 87% of the wound's concentration. a), VEGF diffusion gradient throughout time (VEGF concentration in g mm^{-3}). b), vascular network pattern evolution throughout time in a regular nodal discretization mesh. The tip cell is located at x = 3.8 mm

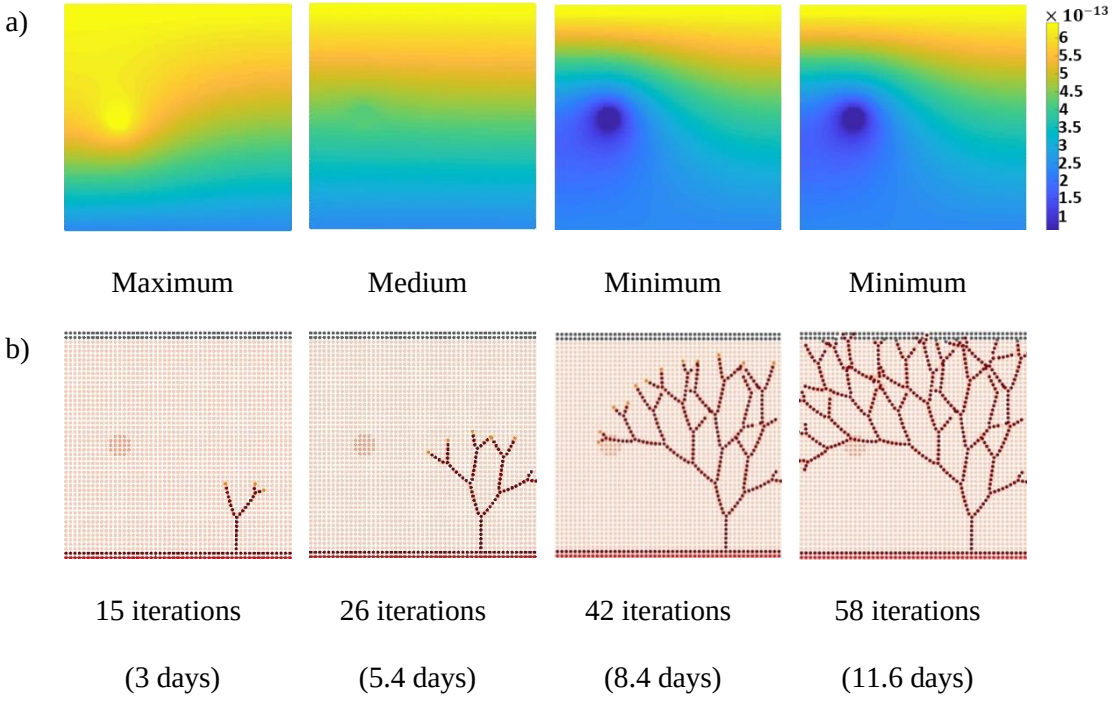

Figure 6.12- Capillary network formed with the biomaterial's VEGF being diffused at a variable rate. Biomaterial loaded with a VEGF concentration equal to the wound's. a), VEGF diffusion gradient throughout time (VEGF concentration in g mm^{-3}). b), vascular network pattern evolution at throughout time in a regular nodal discretization mesh. The tip cell is located at x = 3.8 mm

The presented figures follow the evolution of the capillary network and the VEGF gradient throughout different iterations. In terms of the morphology of the formed capillary networks, the obtained results are similar to the ones for a constant VEGF diffusion rate. Much like the outcomes presented in Figure 6.4, as the biomaterial was loaded with higher VEGF concentrations the more the capillaries grew in its direction. This can be verified by analysing the vessel network images from Figure 6.7 to 6.12. Nevertheless, the capillaries do not migrate as sharply towards the biomaterial when its VEGF concentration decayed over time. Indeed, it is visible in Figure 6.11 b) that the capillaries barely penetrate the biomaterial despite its loading VEGF concentration being of 75% of the wound's concentration. This behaviour was according to expectations since the biomaterial's VEGF concentration decays every time after its loading, decreasing the average biomaterial VEGF concentration. The VEGF diffusion gradient (Figure 6.7 to 6.12) highlights the variation of the VEGF concentration in the biomaterial throughout time.

When comparing the vascular network of 50% VEGF concentration in Figure 6.4 b) to the fourth image of Figure 6.12 b), the location where the capillary penetrates the biomaterial is similar. Not only that, but the overall structure of the vessel network is similar. However, in order to obtain the same network structure, in the variable diffusion rate simulation (Figure 6.12 b) the biomaterial was loaded with double the amount of VEGF (100%) when compared to the constant diffusion rate simulation (50%) (Figure 6.4). This trend is also noticeable upon comparison of the 25% VEGF concentration with constant diffusion rate (Figure 6.4 b) with the 50% VEGF concentration with variable diffusion rate (Figure 6.8 b). This occurrence can be explained by the average VEGF concentration in the simulations where its diffusion rate was variable. Considering the VEGF concentrations (maximum, medium and minimum) denoted at Table 6.2, for a loading concentration of 50% VEGF in a 5-iteration (1 day) cycle, the average concentration of VEGF in the biomaterial is:

$$\frac{3.21 \times 10^{-13} + 2 \times 2.10 \times 10^{-13} + 2 \times 3.07 \times 10^{-14}}{5} = 1.60 \times 10^{-13}\ \mathrm{g\ mm^{-3}}$$

Similarly, for the VEGF loading concentration of 100% the average concentration in a 5-iteration cycle is:

$$\frac{6.43 \times 10^{-13} + 2 \times 4.20 \times 10^{-13} + 2 \times 6.14 \times 10^{-14}}{5} = 3.21 \times 10^{-13}\ \mathrm{g\ mm^{-3}}$$

The average concentration values are the same as the 25% and 50% values presented in Table 6.1 thus, explaining the similarities in the morphology of the compared vessel networks. These results suggest that the vessel network morphology obtained with a biomaterial's VEGF concentration C diffusing at constant rate can be reproduced by loading the biomaterial with a VEGF concentration of $2C$ that has its diffusion rate defined by Eq. 6.2, as long as the wound's VEGF diffusion rate and the domain's geometry are the same in both cases.

The number of endothelial cells for each simulation where the VEGF diffusion was variable was also quantified and it is represented in Figure 6.13.

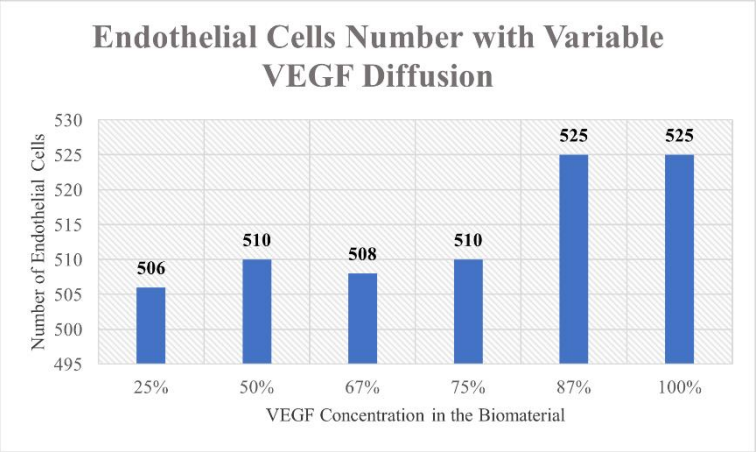

Figure 6.13- Graph representing the number of endothelial cells for each of the VEGF concentrations loaded in the biomaterial. The VEGF concentration in the biomaterial is expressed relatively to the wound's VEGF concentration of 6.43×10^{-13} g mm^{-3}.

Figure 6.13 suggests a tendency for the vascular network density to increase as the VEGF concentration loaded in the biomaterial also increases. There is a small increase in the endothelial cell number from 25% to 50%. The number of endothelial cells the remains fairly constant from 50% until 75%. There is an increase of 15 endothelial cells when the concentration goes to 87%. The number then remains constant until 100%. Comparing Figure 6.13 to Figure 6.5, from concentrations of 50% up until 100% both graphics follow a similar pattern.

Regarding the simulations where the obtained vascular morphology was similar, for the constant VEGF diffusion with concentration of 25% the number of endothelial cells obtained was 512 (Figure 6.5), whereas for the variable VEGF diffusion with loading concentration of 50% the number was 510 (Figure 6.13). These values are extremely close, which supports the similarity between the two capillary networks. For the constant VEGF diffusion with concentration of 50% the number of endothelial cells was of 495

(Figure 6.5) and for the variable VEGF diffusion with loading concentration of 100% the number was 525 (Figure 6.13). The endothelial cell number is discrepant between both simulations. When comparing both vessel networks it is observable that, on the top right corner of the last image of Figure 6.12 there are a few more endothelial cells than in Figure 6.4 b) at the 50% simulation thus, justifying the endothelial count difference.

CHAPTER 7 – CONCLUDING REMARKS

7. Concluding Remarks

In this work, an innovative 2D discrete framework was proposed to model wound-healing sprouting angiogenesis in terms of VEGF diffusion. The proposed model combined the RPIM with VEGF diffusion and was able to reproduce endothelial cell migration and the branching event culminating in morphological realistic networks.

The model was used to study the influence of different parameters such as chemical concentration and wound geometry in the capillary network morphology during wound healing. The results obtained in the preliminary single endothelial sprout studies were in accordance with the principle of chemotaxis and observations in the literature since, regardless of the domain's geometry, it was verified that the endothelial cells migrated from the endothelial cell monolayer to the wound according to the VEGF gradient.

The branching process was implemented in the model by directly using data obtained from *in vivo* CAM assays which by itself is an innovation. The consideration of the branching event resulted in a morphologically realistic capillary network. Furthermore, the model suggested an increased vascular density for superior wound VEGF concentrations which is also in accordance with the literature (Brodsky et al., 2007; H. Wang et al., 2014; Yang et al., 2010). The mathematical model was validated by comparison between the total capillary volume fractions between *in silico* and *in vivo* CAM capillary networks, obtaining a maximum difference of 15%.

The inclusion of a biomaterial that constantly released VEGF in the simulation domain influenced the capillary network formation in a way that, the more the VEGF concentration in the biomaterial increased, the more the capillary network was dragged towards the biomaterial. When considering a variable VEGF diffusion rate for the biomaterial, the capillaries were not as attracted towards it as when compared to the previous constant diffusion simulation. In both cases the capillary network density increased as the VEGF concentration in the biomaterial also increased, and chemotaxis was verified.

Mathematical models need to make assumptions and simplifications to be able to represent the biological phenomena under study. The proposed model presents some limitations, with one of them being its two-dimensionality. Nevertheless, the presented 2D domain is infinite since it uses periodic boundary conditions, which links left-right

and up -down boundary conditions. Other aspects that were not considered in the model include: the uptake of VEGF by the endothelial cells, the mechanical forces that *in vivo* influence angiogenesis, the anisotropic and heterogeneous behaviour of the ECM and other chemical species effects. The inclusion of the mentioned limitations is going to be addressed in future works, since the ultimate goal of the model is to be as complete as possible and produce clinically relevant results. Another possible improvement for the presented model is the expansion to 3D, which would proportionate a level of realism that the model actually does not possess. Nevertheless, it is important to consider that more parameters are needed as the complexity of the model increases and some, may be really hard to obtain or estimate. The results presented in this work regarding the biomaterial's influence in the capillary network formation need to be compared to *in vivo* CAM assays in order to be validated. Furthermore, more domain's geometries need to be tested. These are the next stapes to take.

Ultimately, the aim of this work was exploring a new framework for the modelling of wound-healing angiogenesis and understand how alterations in the wound's geometry, chemical parameters and insertion of new materials can influence the formation of the capillary network. Despite its limitations, the presented model is a valid modelling approach that contributes with valuable information providing an innovative, versatile modelling framework and demonstrating the value of the meshless RPIM for biological problems' applications.

Bibliography

Abdalla, A. M. E., Xiao, L., Ullah, M. W., Yu, M., Ouyang, C., & Yang, G. (2018). Current challenges of cancer anti-angiogenic therapy and the promise of nanotherapeutics. In *Theranostics* (Vol. 8, Issue 2, pp. 533–549). Ivyspring International Publisher. https://doi.org/10.7150/thno.21674

Abhinand, C. S., Raju, R., Soumya, S. J., Arya, P. S., & Sudhakaran, P. R. (2016). VEGF-A/VEGFR2 signaling network in endothelial cells relevant to angiogenesis. *Journal of Cell Communication and Signaling*, *10*(4), 347–354. https://doi.org/10.1007/s12079-016-0352-8

Adair, T. H., & Montani, J.-P. (2010). Angiogenesis. In *Angiogenesis*. Morgan & Claypool Life Sciences. http://www.ncbi.nlm.nih.gov/pubmed/21452444

Agapie, A., Andreica, A., & Giuclea, M. (2014). Probabilistic cellular automata. *Journal of Computational Biology*, *21*(9), 699–708. https://doi.org/10.1089/cmb.2014.0074

Alberts, B., Johnson, A., Lewis, J., Raff, M., Roberts, K., & Walter, P. (2002). *Blood Vessels and Endothelial Cells*. https://www.ncbi.nlm.nih.gov/books/NBK26848/

Alitalo, K., & Carmeliet, P. (2011). Molecular mechanisms of the kidney in health and disease. *Cancer Cell*, *1*, 219–227.

Allen, D. B., Maguire, J. J., Mahdavian, M., Wicke, C., Marcocci, L., Scheuenstuhl, H., Chang, M., Le, A. X., Hopf, H. W., & Hunt, T. K. (1997). Wound hypoxia and acidosis limit neutrophil bacterial killing mechanisms. *Archives of Surgery*, *132*(9), 991–996. https://doi.org/10.1001/archsurg.1997.01430330057009

Alt, W. (1980). Biased random walk models for chemotaxis and related diffusion approximations. *Journal of Mathematical Biology*, *9*(2), 147–177. https://doi.org/10.1007/BF00275919

Amann, A., Zwierzina, M., Koeck, S., Gamerith, G., Pechriggl, E., Huber, J. M., Lorenz, E., Kelm, J. M., Hilbe, W., Zwierzina, H., & Kern, J. (2017). Development of a 3D angiogenesis model to study tumour - endothelial cell interactions and the effects of anti-angiogenic drugs. *Scientific Reports*, *7*(1), 1–13. https://doi.org/10.1038/s41598-017-03010-6

Anderson, A. R. A., & Chaplain, M. A. J. (1998). Continuous and discrete mathematical

models of tumor-induced angiogenesis. *Bulletin of Mathematical Biology*, *60*(5), 857–899. https://doi.org/10.1006/bulm.1998.0042

Auerbach, R., Lewis, R., Shinners, B., Kubai, L., & Akhtar, N. (2003). Angiogenesis assays: A critical overview. *Clinical Chemistry*, *49*(1), 32–40. https://doi.org/10.1373/49.1.32

Ausprunk, D. H., & Folkman, J. (1977). Migration and proliferation of endothelial cells in preformed and newly formed blood vessels during tumor angiogenesis. *Microvascular Research*, *14*(1), 53–65. https://doi.org/10.1016/0026-2862(77)90141-8

Baeriswyl, V., & Christofori, G. (2009). The angiogenic switch in carcinogenesis. In *Seminars in Cancer Biology* (Vol. 19, Issue 5, pp. 329–337). https://doi.org/10.1016/j.semcancer.2009.05.003

Balasubramaniam, V., Mervis, C. F., Maxey, A. M., Markham, N. E., & Abman, S. H. (2007). Hyperoxia reduces bone marrow, circulating, and lung endothelial progenitor cells in the developing lung: Implications for the pathogenesis of bronchopulmonary dysplasia. *American Journal of Physiology - Lung Cellular and Molecular Physiology*, *292*(5). https://doi.org/10.1152/ajplung.00347.2006

Balding, D., & McElwain, D. L. S. (1985). A mathematical model of tumour-induced capillary growth. *Journal of Theoretical Biology*, *114*(1), 53–73. https://doi.org/10.1016/S0022-5193(85)80255-1

Balikova, I., Postelmans, L., Pasteels, B., Coquelet, P., Catherine, J., Efendic, A., Hosoda, Y., Miyake, M., Yamashiro, K., Thienpont, B., & Lambrechts, Di. (2019). Genetic biomarkers in the VEGF pathway predicting response to anti-VEGF therapy in age-related macular degeneration. *BMJ Open Ophthalmology*, *4*(1). https://doi.org/10.1136/bmjophth-2019-000273

Ballas, S. K. (1987). Erythrocyte concentration and volume are inversely related. In *Clinica Chimica Acta* (Vol. 164, Issue 2, pp. 243–244). https://doi.org/10.1016/0009-8981(87)90078-7

Basu, D., & Kulkarni, R. (2014). Overview of blood components and their preparation. In *Indian Journal of Anaesthesia* (Vol. 58, Issue 5, pp. 529–537). Indian Society of Anaesthetists. https://doi.org/10.4103/0019-5049.144647

Bauer, A. L., Jackson, T. L., & Jiang, Y. (2007). A cell-based model exhibiting branching and anastomosis during tumor-induced angiogenesis. *Biophysical Journal*, *92*(9), 3105–3121. https://doi.org/10.1529/biophysj.106.101501

Bauer, A. L., Jackson, T. L., & Jiang, Y. (2009). Topography of extracellular matrix mediates vascular morphogenesis and migration speeds in angiogenesis. *PLoS Computational Biology*, *5*(7). https://doi.org/10.1371/journal.pcbi.1000445

Beik, J., Khateri, M., Khosravi, Z., Kamrava, S. K., Kooranifar, S., Ghaznavi, H., & Shakeri-Zadeh, A. (2019). Gold nanoparticles in combinatorial cancer therapy strategies. In *Coordination Chemistry Reviews* (Vol. 387, pp. 299–324). Elsevier B.V. https://doi.org/10.1016/j.ccr.2019.02.025

Belinha, J. (2014). *Meshless Methods in Biomechanics - Bone Tissue Remodelling Analysis* (J. M. R. S. Tavares & R. M. Natal Jorge (eds.); Vol.16). Lecture Notes in Computational Vision and Biomechanics, Springer Netherlands. https://doi.org/10.1007/978-3-319-06400-0

Belinha, J., Araújo, A. L., Ferreira, A. J. M., Dinis, L. M. J. S., & Natal Jorge, R. M. (2016). The analysis of laminated plates using distinct advanced discretization meshless techniques. *Composite Structures*, *143*, 165–179. https://doi.org/10.1016/j.compstruct.2016.02.021

Benguigui, M., Weitz, I. S., Timaner, M., Kan, T., Shechter, D., Perlman, O., Sivan, S., Raviv, Z., Azhari, H., & Shaked, Y. (2019). Copper oxide nanoparticles inhibit pancreatic tumor growth primarily by targeting tumor initiating cells. *Scientific Reports*, *9*(1), 1–10. https://doi.org/10.1038/s41598-019-48959-8

Bentley, K., Gerhardt, H., & Bates, P. A. (2008). Agent-based simulation of notch-mediated tip cell selection in angiogenic sprout initialisation. *Journal of Theoretical Biology*, *250*(1), 25–36. https://doi.org/10.1016/j.jtbi.2007.09.015

Bikfalvi, A. (2004). *Angiogenesis*. *1*, 227–233.

Blumenreich, M. S. (1990). The White Blood Cell and Differential Count. In *Clinical Methods: The History, Physical, and Laboratory Examinations*. Butterworths. http://www.ncbi.nlm.nih.gov/pubmed/21250104

Bookholt, F. D., Monsuur, H. N., Gibbs, S., & Vermolen, F. J. (2016). Mathematical modelling of angiogenesis using continuous cell-based models. *Biomechanics and*

Modeling in Mechanobiology, *15*(6), 1577–1600. https://doi.org/10.1007/s10237-016-0784-3

Bowden, L. G., Byrne, H. M., Maini, P. K., & Moulton, D. E. (2016). A morphoelastic model for dermal wound closure. *Biomechanics and Modeling in Mechanobiology*, *15*(3), 663–681. https://doi.org/10.1007/s10237-015-0716-7

Brat, D. J., Kaur, B., & Van Meir, E. G. (2003). Genetic modulation of hypoxia induced gene expression and angiogenesis: Relevance to brain tumors. In *Frontiers in Bioscience* (Vol. 8). Frontiers in Bioscience. https://doi.org/10.2741/942

Brodland, G. W. (2015). How computational models can help unlock biological systems. In *Seminars in Cell and Developmental Biology* (Vols. 47–48, pp. 62–73). Academic Press. https://doi.org/10.1016/j.semcdb.2015.07.001

Brodsky, S. V., Mendelev, N., Melamed, M., & Ramaswamy, G. (2007). Vascular density and VEGF expression in hepatic lesions. *Journal of Gastrointestinal and Liver Diseases*, *16*(4), 373–377. https://europepmc.org/article/med/18193117

Broughton, G., Janis, J. E., & Attinger, C. E. (2006). Wound healing: An overview. In *Plastic and Reconstructive Surgery* (Vol. 117, Issue 7 SUPPL.). https://doi.org/10.1097/01.prs.0000222562.60260.f9

Buganza Tepole, A., & Kuhl, E. (2013). Systems-based approaches toward wound healing. In *Pediatric Research* (Vol. 73, Issues 4–2, pp. 553–563). https://doi.org/10.1038/pr.2013.3

Byrne, M., Chaplain, M. A. J., Evans, D. L., & Hopkinson, I. (2000). Mathematical modelling of angiogenesis in wound healing: Comparison of theory and experiment. *Journal of Theoretical Medicine*, *2*(3), 175–197. https://doi.org/10.1080/10273660008833045

Caduff, J. H., Fischer, L. C., & Burri, P. H. (1986). Scanning electron microscope study of the developing microvasculature in the postnatal rat lung. *The Anatomical Record*, *216*(2), 154–164. https://doi.org/10.1002/ar.1092160207

Callaghan, T., Khain, E., Sander, L. M., & Ziff, R. M. (2006). A stochastic model for wound healing. *Journal of Statistical Physics*, *122*(5), 909–924. https://doi.org/10.1007/s10955-006-9022-1

Carlier, A., Geris, L., Bentley, K., Carmeliet, G., Carmeliet, P., & Van Oosterwyck, H.

(2012). MOSAIC: A Multiscale Model of Osteogenesis and Sprouting Angiogenesis with Lateral Inhibition of Endothelial Cells. *PLoS Computational Biology*, *8*(10), e1002724. https://doi.org/10.1371/journal.pcbi.1002724

Carmeliet, P. (2000). Mechanisms of angiogenesis and arteriogenesis. In *Nature Medicine* (Vol. 6, Issue 4, pp. 389–395). https://doi.org/10.1038/74651

Carmeliet, P., & Jain, R. K. (2011). Molecular mechanisms and clinical applications of angiogenesis. *Nature*, *473*(7347), 298–307. https://doi.org/10.1038/nature10144

Chang, S. H., Kanasaki, K., Gocheva, V., Blum, G., Harper, J., Moses, M. A., Shih, S. C., Nagy, J. A., Joyce, J., Bogyo, M., Kalluri, R., & Dvorak, H. F. (2009). VEGF-A induces angiogenesis by perturbing the cathepsin-cysteine protease inhibitor balance in venules, causing basement membrane degradation and mother vessel formation. *Cancer Research*, *69*(10), 4537–4544. https://doi.org/10.1158/0008-5472.CAN-08-4539

Chaplain, M. A. J. (2000). Mathematical modelling of angiogenesis. In *Journal of Neuro-Oncology* (Vol. 50, Issues 1–2, pp. 37–51). Springer. https://doi.org/10.1023/A:1006446020377

Chaplain, M. A. J., & Byrne, H. M. (1996). The mathematical modelling of wound healing and tumour growth: two sides of the same coin. *Wounds: A Compendium of Clinical Research and Practice*, *8*(2), 42–48. https://discovery.dundee.ac.uk/en/publications/the-mathematical-modelling-of-wound-healing-and-tumour-growth-two

Childs, S., Chen, J.-N., Garrity, D. M., & Fishman, M. C. (2002). Patterning of angiogenesis in the zebrafish embryo. *Development*, *129*(4).

Chopard, B., & Droz, M. (1998). Cellular Automata Modeling of Physical Systems. In C. Godrèche (Ed.), *Cambridge University Press*. Cambridge University Press.

Cumming, B. D., McElwain, D. L. S., & Upton, Z. (2009). A mathematical model of wound healing and subsequent scarring. *Journal of the Royal Society Interface*, *7*(42), 19–34. https://doi.org/10.1098/rsif.2008.0536

Dabbagh, A., Amini, A., Abdollahifar, M. A., & Saghafi, M. A. (2017). Cardiovascular system embryology and development. In *Congenital Heart Disease in Pediatric and Adult Patients: Anesthetic and Perioperative Management* (pp. 11–64). Springer

International Publishing. https://doi.org/10.1007/978-3-319-44691-2_2

Daub, J. T., Roeland, ·, Merks, M. H., Daub, J. T., & Merks, R. M. H. (2013). A Cell-Based Model of Extracellular-Matrix-Guided Endothelial Cell Migration During Angiogenesis. *Bull Math Biol*, *75*, 1377–1399. https://doi.org/10.1007/s11538-013-9826-5

Davis, G. E., & Senger, D. R. (2005). Endothelial extracellular matrix: Biosynthesis, remodeling, and functions during vascular morphogenesis and neovessel stabilization. In *Circulation Research* (Vol. 97, Issue 11, pp. 1093–1107). Circ Res. https://doi.org/10.1161/01.RES.0000191547.64391.e3

De Haas, S., Delmar, P., Bansal, A. T., Moisse, M., Miles, D. W., Leighl, N., Escudier, B., Van Cutsem, E., Carmeliet, P., Scherer, S. J., Pallaud, C., & Lambrechts, D. (2014). Genetic variability of VEGF pathway genes in six randomized phase III trials assessing the addition of bevacizumab to standard therapy. *Angiogenesis*, *17*(4), 909–920. https://doi.org/10.1007/s10456-014-9438-1

Deakin, A. S. (1976). Model for initial vascular patterns in melanoma transplants. *Growth*, *40*(2), 191–201. http://europepmc.org/article/med/1278714#impact

Diez-Silva, M., Dao, M., Han, J., Lim, C. T., & Suresh, S. (2010). Shape and biomechanics characteristics of human red blood cells in health and disease. *MRS Bulletin*, *35*(5), 382–388. https://doi.org/10.1557/mrs2010.571

Dimitrova, E. S., Licona, M. P. V., McGee, J., & Laubenbacher, R. (2010). Discretization of time series data. *Journal of Computational Biology*, *17*(6), 853–868. https://doi.org/10.1089/cmb.2008.0023

Dinis, L. M. J. S., Natal Jorge, R. M., & Belinha, J. (2007). Analysis of 3D solids using the natural neighbour radial point interpolation method. *Computer Methods in Applied Mechanics and Engineering*, *196*(13–16), 2009–2028. https://doi.org/10.1016/j.cma.2006.11.002

Djonov, V., Baum, O., & Burri, P. H. (2003). Vascular remodeling by intussusceptive angiogenesis. *Cell and Tissue Research*, *314*(1), 107–117. https://doi.org/10.1007/s00441-003-0784-3

Drake, R. L., Vogl, A. W., & Mitchell, A. W. . (2019). Gray's Anatomy for Students, 4th Edition. In *Gray's Anatomy for Students*.

Ebos, J. M. L., Lee, C. R., Cruz-Munoz, W., Bjarnason, G. A., Christensen, J. G., & Kerbel, R. S. (2009). Accelerated Metastasis after Short-Term Treatment with a Potent Inhibitor of Tumor Angiogenesis. *Cancer Cell*, *15*(3), 232–239. https://doi.org/10.1016/j.ccr.2009.01.021

Enoch, S., & Leaper, D. J. (2008). Basic science of wound healing. In *Surgery* (Vol. 26, Issue 2, pp. 31–37). https://doi.org/10.1016/j.mpsur.2007.11.005

Escámez, M. J., García, M., Larcher, F., Meana, A., Muñoz, E., Jorcano, J. L., & Del Río, M. (2004). An in vivo model of wound healing in genetically modified skin-humanized mice. *Journal of Investigative Dermatology*, *123*(6), 1182–1191. https://doi.org/10.1111/j.0022-202X.2004.23473.x

Farid, Y., & Lecat, P. (2019). Biochemistry, Hemoglobin Synthesis. In *StatPearls*. StatPearls Publishing. http://www.ncbi.nlm.nih.gov/pubmed/30725597

Feher, J. (2012). The Heart as a Pump. In *Quantitative Human Physiology* (pp. 516–524). Elsevier. https://doi.org/10.1016/b978-0-12-800883-6.00047-1

Ferrara, N., Gerber, H., & Lecouter, J. (2003). *The biology of VEGF and its receptors*. *9*(6), 669–676.

Ferrari, M. (2005). Cancer nanotechnology: Opportunities and challenges. In *Nature Reviews Cancer* (Vol. 5, Issue 3, pp. 161–171). Nature Publishing Group. https://doi.org/10.1038/nrc1566

Flegg, J. A., Byrne, H. M., Flegg, M. B., & Sean McElwain, D. L. (2012). Wound healing angiogenesis: The clinical implications of a simple mathematical model. *Journal of Theoretical Biology*, *300*, 309–316. https://doi.org/10.1016/j.jtbi.2012.01.043

Flegg, J. A., Byrne, H. M., & McElwain, D. L. S. (2010). Mathematical Model of Hyperbaric Oxygen Therapy Applied to Chronic Diabetic Wounds. *Bulletin of Mathematical Biology*, *72*(7), 1867–1891. https://doi.org/10.1007/s11538-010-9514-7

Flegg, J. A., Kasza, J., Darby, I., & Weller, C. D. (2015). Healing of venous ulcers using compression therapy: Predictions of a mathematical model. *Journal of Theoretical Biology*, *379*, 1–9. https://doi.org/10.1016/j.jtbi.2015.04.028

Flegg, J. A., McElwain, D. L. S., Byrne, H. M., & Turner, I. W. (2009). A three species model to simulate application of hyperbaric oxygen therapy to chronic wounds.

PLoS Computational Biology, *5*(7), 1000451. https://doi.org/10.1371/journal.pcbi.1000451

Folkman, J., Merler, E., Abernathy, C., & Williams, G. (1971). *Isolation of a Tumor Factor Responsible For Angiogenesis*. https://doi.org/https://doi.org/10.1084/jem.133.2.275

Fournier, G. A., Lutty, G. A., Watt, S., Fenselau, A., & Patz, A. (1981). A corneal micropocket assay for angiogenesis in the rat eye. *Investigative Ophthalmology and Visual Science*, *21*(2), 351–354.

Gaffney, E. A., Pugh, K., Maini, P. K., & Arnold, F. (2002). Investigating a simple model of cutaneous wound healing angiogenesis. *Journal of Mathematical Biology*, *45*(4), 337–374. https://doi.org/10.1007/s002850200161

Gerhardt, H., Golding, M., Fruttiger, M., Ruhrberg, C., Lundkvist, A., Abramsson, A., Jeltsch, M., Mitchell, C., Alitalo, K., Shima, D., & Betsholtz, C. (2003). VEGF guides angiogenic sprouting utilizing endothelial tip cell filopodia. *Journal of Cell Biology*, *161*(6), 1163–1177. https://doi.org/10.1083/jcb.200302047

Gevertz, J. L., & Torquato, S. (2006). Modeling the effects of vasculature evolution on early brain tumor growth. *Journal of Theoretical Biology*, *243*(4), 517–531. https://doi.org/10.1016/j.jtbi.2006.07.002

Ghajar, C. M., Blevins, K. S., Hughes, C. C. W., George, S. C., & Putnam, A. J. (2006). Mesenchymal stem cells enhance angiogenesis in mechanically viable prevascularized tissues via early matrix metalloproteinase upregulation. *Tissue Engineering*, *12*(10), 2875–2888. https://doi.org/10.1089/ten.2006.12.2875

Ghoshal, K., & Bhattacharyya, M. (2014). Overview of platelet physiology: Its hemostatic and nonhemostatic role in disease pathogenesis. *The Scientific World Journal*, *2014*. https://doi.org/10.1155/2014/781857

Gonzalez, A. C. D. O., Andrade, Z. D. A., Costa, T. F., & Medrado, A. R. A. P. (2016). Wound healing - A literature review. In *Anais Brasileiros de Dermatologia* (Vol. 91, Issue 5, pp. 614–620). Sociedade Brasileira de Dermatologia. https://doi.org/10.1590/abd1806-4841.20164741

Gross, J., Farinelli, W., Sadow, P., Anderson, R., & Bruns, R. (1995). On the mechanism of skin wound “contraction”: A granulation tissue “knockout” with a normal

phenotype. *Proceedings of the National Academy of Sciences of the United States of America*, *92*(13), 5982–5986. https://doi.org/10.1073/pnas.92.13.5982

Guerra, A., Belinha, J., Mangir, N., MacNeil, S., & Natal Jorge, R. (2020). Sprouting Angiogenesis: A Numerical Approach with Experimental Validation. *Annals of Biomedical Engineering*, *49*(2), 871–884. https://doi.org/10.1007/s10439-020-02622-w

Guerra, A., Belinha, J., & Natal Jorge, R. (2020). A preliminary study of endothelial cell migration during angiogenesis using a meshless method approach. *International Journal for Numerical Methods in Biomedical Engineering*, *36*(11). https://doi.org/10.1002/cnm.3393

Gupta, K., & Zhang, J. (2005). Angiogenesis: A curse or cure? *Postgraduate Medical Journal*, *81*(954), 236–242. https://doi.org/10.1136/pgmj.2004.023309

Hall, A. P. (2005). The role of angiogenesis in cancer. *Comparative Clinical Pathology*, *13*(3), 95–99. https://doi.org/10.1007/s00580-004-0533-3

Hein, A., Lambrechts, D., Von Minckwitz, G., Häberle, L., Eidtmann, H., Tesch, H., Untch, M., Hilfrich, J., Schem, C., Rezai, M., Gerber, B., Dan Costa, S., Blohmer, J. U., Schwedler, K., Kittel, K., Fehm, T., Kunz, G., Beckmann, M. W., Ekici, A. B., … Fasching, P. A. (2015). Genetic variants in VEGF pathway genes in neoadjuvant breast cancer patients receiving bevacizumab: Results from the randomized phase III GeparQuinto study. *International Journal of Cancer*, *137*(12), 2981–2988. https://doi.org/10.1002/ijc.29656

Hendrata, M., & Sudiono, J. (2019). A hybrid multiscale model for investigating tumor angiogenesis and its response to cell-based therapy. *In Silico Biology*, *13*(1–2), 1–20. https://doi.org/10.3233/ISB-170469

Hescheler, J., Fleischmann, B. K., Wartenberg, M., Bloch, W., Kolossov, E., Ji, G., Addicks, K., & Sauer, H. (1999). Establishment of ionic channels and signalling cascades in the embryonic stem cell-derived primitive endoderm and cardiovascular system. *Cells Tissues Organs*, *165*(3–4), 153–164. https://doi.org/10.1159/000016695

Hildebrand, F. (1987). *Introduction to numerical analysis*. https://www.google.com/books?hl=pt-

PT&lr=&id=f7We11dz0_kC&oi=fnd&pg=PP1&dq=Introduction+to+Numerical+Analysis:+Second+Edition+Por+F.+B.+Hildebrand&ots=7GdtZuLoyB&sig=1_Ewh-vpB6Q2zJmjxUnG9O4oRq0

Hinshaw, J. R., & Miller, E. R. (1965). Histology of Healing Split-Thickness, Full-Thickness Autogenous Skin Grafts and Donor Sites. *Archives of Surgery*, *91*(4), 658–670. https://doi.org/10.1001/archsurg.1965.01320160112027

Huy, T. Q., Huyen, P. T. M., Le, A.-T., & Tonezzer, M. (2019). Recent Advances of Silver Nanoparticles in Cancer Diagnosis and Treatment. *Anti-Cancer Agents in Medicinal Chemistry*, *20*(11), 1276–1287. https://doi.org/10.2174/1871520619666190710121727

JACOBS, A., RENAUDIN, G., FORESTIER, C., NEDELEC, J.-M., & DESCAMPS, S. (2020). Biological properties of copper-doped biomaterials for orthopedic applications: a review of antibacterial, angiogenic and osteogenic aspects. *Acta Biomaterialia*. https://doi.org/10.1016/j.actbio.2020.09.044

Jalilian, E., Elkin, K., & Shin, S. R. (2020). Novel cell-based and tissue engineering approaches for induction of angiogenesis as an alternative therapy for diabetic retinopathy. *International Journal of Molecular Sciences*, *21*(10), 1–20. https://doi.org/10.3390/ijms21103496

Javierre, E., Vermolen, F. J., Vuik, C., & van der Zwaag, S. (2009). A mathematical analysis of physiological and morphological aspects of wound closure. *Journal of Mathematical Biology*, *59*(5), 605–630. https://doi.org/10.1007/s00285-008-0242-7

Jia, S., Zhang, R., Li, Z., & Li, J. (2017). Clinical and biological significance of circulating tumor cells, circulating tumor DNA, and exosomes as biomarkers in colorectal cancer. In *Oncotarget* (Vol. 8, Issue 33, pp. 55632–55645). Impact Journals LLC. https://doi.org/10.18632/oncotarget.17184

Kaipainen, A., Korhonen, J., Mustonen, T., Van Hinsbergh, V. W. M., Fang, G. H., Dumont, D., Breitman, M., & Alitalo, K. (1995). Expression of the fms-like tyrosine kinase 4 gene becomes restricted to lymphatic endothelium during development. *Proceedings of the National Academy of Sciences of the United States of America*, *92*(8), 3566–3570. https://doi.org/10.1073/pnas.92.8.3566

Karayiannakis, A. J., Zbar, A., Polychronidis, A., & Simopoulos, C. (2003). Serum and

drainage fluid vascular endothelial growth factor levels in early surgical wounds. *European Surgical Research*, *35*(6), 492–496. https://doi.org/10.1159/000073388

Kargozar, S., Lotfibakhshaiesh, N., Ai, J., Samadikuchaksaraie, A., Hill, R. G., Shah, P. A., Milan, P. B., Mozafari, M., Fathi, M., & Joghataei, M. T. (2016). Synthesis, physico-chemical and biological characterization of strontium and cobalt substituted bioactive glasses for bone tissue engineering. *Journal of Non-Crystalline Solids*, *449*, 133–140. https://doi.org/10.1016/j.jnoncrysol.2016.07.025

Katz, A. (2011). *Physiology of the Heart (fifth edition)* (5th ed.). Lippincott Williams & Wilkins.

Khodadoust, M. S., Verhaegen, M., Kappes, F., Riveiro-Falkenbach, E., Cigudosa, J. C., Kim, D. S. L., Chinnaiyan, A. M., Markovitz, D. M., & Soengas, M. S. (2009). Melanoma proliferation and chemoresistance controlled by the DEK oncogene. *Cancer Research*, *69*(16), 6405–6413. https://doi.org/10.1158/0008-5472.CAN-09-1063

Kim, K. J., Li, B., Winer, J., Armanini, M., Gillett, N., Phillips, H. S., & Ferrara, N. (1993). Inhibition of vascular endothelial growth factor-induced angiogenesis suppresses tumour growth in vivo. *Nature*, *362*(6423), 841–844. https://doi.org/10.1038/362841a0

Komutrattananont, P., Mahakkanukrauh, P., & Das, S. (2019). Morphology of the human aorta and age-related changes: Anatomical facts. In *Anatomy and Cell Biology* (Vol. 52, Issue 2, pp. 109–114). Korean Association of Anatomists. https://doi.org/10.5115/acb.2019.52.2.109

Kuhn, V., Diederich, L., Keller, T. C. S., Kramer, C. M., Lückstädt, W., Panknin, C., Suvorava, T., Isakson, B. E., Kelm, M., & Cortese-Krott, M. M. (2017). Red Blood Cell Function and Dysfunction: Redox Regulation, Nitric Oxide Metabolism, Anemia. *Antioxidants and Redox Signaling*, *26*(13), 718–742. https://doi.org/10.1089/ars.2016.6954

Kumar, P., Kumar, S., Udupa, E. P., Kumar, U., Rao, P., & Honnegowda, T. (2015). Role of angiogenesis and angiogenic factors in acute and chronic wound healing. *Plastic and Aesthetic Research*, *2*(5), 243. https://doi.org/10.4103/2347-9264.165438

LAPLANTE, A. F., GERMAIN, L., AUGER, F. A., & MOULIN, V. (2001). Mechanisms

of wound reepithelialization: hints from a tissue-engineered reconstructed skin to long-standing questions. *The FASEB Journal*, *15*(13), 2377–2389. https://doi.org/10.1096/fj.01-0250com

Lee, J. H., Parthiban, P., Jin, G. Z., Knowles, J. C., & Kim, H. W. (2020). Materials roles for promoting angiogenesis in tissue regeneration. In *Progress in Materials Science* (p. 100732). Elsevier Ltd. https://doi.org/10.1016/j.pmatsci.2020.100732

Lee, S., Jilan, S. M., Nikolova, G. V., Carpizo, D., & Luisa Iruela-Arispe, M. (2005). Processing of VEGF-A by matrix metalloproteinases regulates bioavailability and vascular patterning in tumors. *Journal of Cell Biology*, *169*(4), 681–691. https://doi.org/10.1083/jcb.200409115

Lever, M. J. (2005). The cardiovascular system. In *Biomaterials, Artificial Organs and Tissue Engineering* (pp. 90–96). Elsevier Inc. https://doi.org/10.1533/9781845690861.2.90

Liang, X., Li, H., Coussy, F., Callens, C., & Lerebours, F. (2019). An update on biomarkers of potential benefit with bevacizumab for breast cancer treatment: Do we make progress? *Chinese Journal of Cancer Research*, *31*(4), 586–600. https://doi.org/10.21147/j.issn.1000-9604.2019.04.03

Liao, D., & Johnson, R. S. (2007). Hypoxia: A key regulator of angiogenesis in cancer. In *Cancer and Metastasis Reviews* (Vol. 26, Issue 2, pp. 281–290). Cancer Metastasis Rev. https://doi.org/10.1007/s10555-007-9066-y

Lim, Z. Z. J., Li, J. E. J., Ng, C. T., Yung, L. Y. L., & Bay, B. H. (2011). Gold nanoparticles in cancer therapy. In *Acta Pharmacologica Sinica* (Vol. 32, Issue 8, pp. 983–990). Nature Publishing Group. https://doi.org/10.1038/aps.2011.82

Liu, Gang, Qutub, A. A., Vempati, P., Mac Gabhann, F., & Popel, A. S. (2011). Module-based multiscale simulation of angiogenesis in skeletal muscle. *Theoretical Biology and Medical Modelling*, *8*(1), 1–26. https://doi.org/10.1186/1742-4682-8-6

Liu, GR, & Quek, S. (2013). The finite element method: a practical course. *Butterworth-Heinemann*.

Liu, W., Zhang, G., Wu, J., Zhang, Y., Liu, J., Luo, H., & Shao, L. (2020). Insights into the angiogenic effects of nanomaterials: Mechanisms involved and potential applications. *Journal of Nanobiotechnology*, *18*(1), 1–22.

https://doi.org/10.1186/s12951-019-0570-3

Lobov, I. B., Brooks, P. C., & Lang, R. A. (2002). Angiopoietin-2 displays VEGF-dependent modulation of capillary structure and endothelial cell survival in vivo. *Proceedings of the National Academy of Sciences of the United States of America*, *99*(17), 11205–11210. https://doi.org/10.1073/pnas.172161899

Machado, M. J. C., Watson, M. G., Devlin, A. H., Chaplain, M. A. J., Mcdougall, S. R., & Mitchell, C. A. (2011). Dynamics of Angiogenesis During Wound Healing: A Coupled In Vivo and In Silico Study. *Microcirculation*, *18*(3), 183–197. https://doi.org/10.1111/j.1549-8719.2010.00076.x

Maggelakis, S. A. (2003). A mathematical model of tissue replacement during epidermal wound healing. *Applied Mathematical Modelling*, *27*(3), 189–196. https://doi.org/10.1016/S0307-904X(02)00100-2

Mangir, N., Dikici, S., Claeyssens, F., & Macneil, S. (2019). Using ex Ovo Chick Chorioallantoic Membrane (CAM) Assay to Evaluate the Biocompatibility and Angiogenic Response to Biomaterials. *ACS Biomaterials Science and Engineering*, *5*(7), 3190–3200. https://doi.org/10.1021/acsbiomaterials.9b00172

Mank, V., & Brown, K. (2020). Leukocytosis. In *StatPearls*. StatPearls Publishing. http://www.ncbi.nlm.nih.gov/pubmed/32809717

Marshall, C. D., Hu, M. S., Leavitt, T., Barnes, L. A., Lorenz, H. P., & Longaker, M. T. (2018). Cutaneous Scarring: Basic Science, Current Treatments, and Future Directions. In *Advances in Wound Care* (Vol. 7, Issue 2, pp. 29–45). Mary Ann Liebert Inc. https://doi.org/10.1089/wound.2016.0696

Martino, M. M., & Hubbell, J. A. (2010). The 12th–14th type III repeats of fibronectin function as a highly promiscuous growth factor-binding domain. *The FASEB Journal*, *24*(12), 4711–4721. https://doi.org/10.1096/fj.09-151282

Mastrullo, V., Cathery, W., Velliou, E., Madeddu, P., & Campagnolo, P. (2020). Angiogenesis in Tissue Engineering: As Nature Intended? *Frontiers in Bioengineering and Biotechnology*, *8*(March), 1–13. https://doi.org/10.3389/fbioe.2020.00188

Mathew, J., & Bhimji, S. S. (2018). Physiology, Blood Plasma. In *StatPearls*. StatPearls Publishing. http://www.ncbi.nlm.nih.gov/pubmed/30285399

Matienzo, D., & Bordoni, B. (2020). *Anatomy, Blood Flow*. https://www.ncbi.nlm.nih.gov/books/NBK554457/

McDougall, S. R., Anderson, A. R. A., Chaplain, M. A. J., & Sherratt, J. A. (2002). Mathematical modelling of flow through vascular networks: Implications for tumour-induced angiogenesis and chemotherapy strategies. *Bulletin of Mathematical Biology*, *64*(4), 673–702. https://doi.org/10.1006/bulm.2002.0293

McDougall, Steven R., Anderson, A. R. A., & Chaplain, M. A. J. (2006). Mathematical modelling of dynamic adaptive tumour-induced angiogenesis: Clinical implications and therapeutic targeting strategies. *Journal of Theoretical Biology*, *241*(3), 564–589. https://doi.org/10.1016/j.jtbi.2005.12.022

McGrath, M. H., & Simon, R. H. (1983). Wound geometry and the kinetics of wound contraction. *Plastic and Reconstructive Surgery*, *72*(1), 66–72. https://doi.org/10.1097/00006534-198307000-00015

Merks, R. M. H., Newman, S. A., & Glazier, J. A. (2004). Cell-oriented modeling of in vitro capillary development. *Lecture Notes in Computer Science (Including Subseries Lecture Notes in Artificial Intelligence and Lecture Notes in Bioinformatics)*, *3305*, 425–434. https://doi.org/10.1007/978-3-540-30479-1_44

Milde, F., Bergdorf, M., & Koumoutsakos, P. (2008). A hybrid model for three-dimensional simulations of sprouting angiogenesis. *Biophysical Journal*, *95*(7), 3146–3160. https://doi.org/10.1529/biophysj.107.124511

Moreo, P., García-Aznar, J. M., & Doblaré, M. (2008). Modeling mechanosensing and its effect on the migration and proliferation of adherent cells. *Acta Biomaterialia*, *4*(3), 613–621. https://doi.org/10.1016/j.actbio.2007.10.014

Mukherjee, S. (2018). Recent progress toward antiangiogenesis application of nanomedicine in cancer therapy. In *Future Science OA* (Vol. 4, Issue 7). Future Medicine Ltd. https://doi.org/10.4155/fsoa-2018-0051

N. Thon, J., & E. Italiano, J. (2012). Platelets: Production, Morphology and Ultrastructure. *Handbook of Experimental Pharmacology*, *210*, 3–22. https://doi.org/10.1007/978-3-642-29423-5

Naik, M., Brahma, P., & Dixit, M. (2018). A cost-effective and efficient chick ex-ovo cam assay protocol to assess angiogenesis. *Methods and Protocols*, *1*(2), 1–9.

https://doi.org/10.3390/mps1020019

Nasevicius, A., Larson, J., & Ekker, S. G. (2000). Distinct requirements for zebrafish angiogenesis revealed by a VEGF-A morphant. *Yeast*, *17*(4), 294–301. https://doi.org/10.1002/1097-0061(200012)17:4<294::aid-yea54>3.0.co;2-5

Nguyen, E. H., & Murphy, W. L. (2018). Customizable biomaterials as tools for advanced anti-angiogenic drug discovery. In *Biomaterials* (Vol. 181, pp. 53–66). Elsevier Ltd. https://doi.org/10.1016/j.biomaterials.2018.07.041

Nikolova, M. P., & Chavali, M. S. (2019). Recent advances in biomaterials for 3D scaffolds: A review. *Bioactive Materials*, *4*, 271–292. https://doi.org/10.1016/j.bioactmat.2019.10.005

Nussbaum, S. R., Carter, M. J., Fife, C. E., DaVanzo, J., Haught, R., Nusgart, M., & Cartwright, D. (2018). An Economic Evaluation of the Impact, Cost, and Medicare Policy Implications of Chronic Nonhealing Wounds. *Value in Health*, *21*(1), 27–32. https://doi.org/10.1016/j.jval.2017.07.007

O'Brien, F. J. (2011). Biomaterials & scaffolds for tissue engineering. *Materials Today*, *14*(3), 88–95. https://doi.org/10.1016/S1369-7021(11)70058-X

Olfert, I. M., Baum, O., Hellsten, Y., & Egginton, S. (2016). Advances and challenges in skeletal muscle angiogenesis. *American Journal of Physiology-Heart and Circulatory Physiology*, *310*(3), H326–H336. https://doi.org/10.1152/ajpheart.00635.2015

Olsen, L., Sherrattf, J. A., Maini, P. K., & Arnold, F. (1997). A mathematical model for the capillary endothelial cell-extracellular matrix interactions in wound-healing angiogenesis. In *IMA Journal of Mathematics Applied in Medicine & Biology* (Vol. 14).

Otsu, K., Das, S., Houser, S. D., Quadri, S. K., Bhattacharya, S., & Bhattacharya, J. (2009). Concentration-dependent inhibition of angiogenesis by mesenchymal stem cells. *Blood*, *113*(18), 4197–4205. https://doi.org/10.1182/blood-2008-09-176198

Pàez-Ribes, M., Allen, E., Hudock, J., Takeda, T., Okuyama, H., Viñals, F., Inoue, M., Bergers, G., Hanahan, D., & Casanovas, O. (2009). Antiangiogenic Therapy Elicits Malignant Progression of Tumors to Increased Local Invasion and Distant Metastasis. *Cancer Cell*, *15*(3), 220–231. https://doi.org/10.1016/j.ccr.2009.01.027

Pallone, T. L., & Silldorff, E. P. (2001). Pericyte regulation of renal medullary blood flow. In *Experimental Nephrology* (Vol. 9, Issue 3, pp. 165–170). S. Karger AG. https://doi.org/10.1159/000052608

Pasqua, L., Leggio, A., Sisci, D., Andò, S., & Morelli, C. (2016). Mesoporous Silica Nanoparticles in Cancer Therapy: Relevance of the Targeting Function. *Mini-Reviews in Medicinal Chemistry*, *16*(9), 743–753. https://doi.org/10.2174/1389557516666160321113620

Pastar, I., Stojadinovic, O., Yin, N. C., Ramirez, H., Nusbaum, A. G., Sawaya, A., Patel, S. B., Khalid, L., Isseroff, R. R., & Tomic-Canic, M. (2014). Epithelialization in Wound Healing: A Comprehensive Review. *Advances in Wound Care*, *3*(7), 445–464. https://doi.org/10.1089/wound.2013.0473

Patel, V., Chivukala, I., Roy, S., Khanna, S., He, G., Ojha, N., Mehrotra, A., Dias, L. M., Hunt, T. K., & Sen, C. K. (2005). Oxygen: From the benefits of inducing VEGF expression to managing the risk of hyperbaric stress. *Antioxidants and Redox Signaling*, *7*(9–10), 1377–1387. https://doi.org/10.1089/ars.2005.7.1377

Paweletz, N., & Knierim, M. (1989). Tumor-related angiogenesis. *Critical Reviews in Oncology and Hematology*, *9*(3), 197–242. https://doi.org/10.1016/S1040-8428(89)80002-2

Peirce, S. M. (2008). Computational and mathematical modeling of angiogenesis. In *Microcirculation* (Vol. 15, Issue 8, pp. 739–751). NIH Public Access. https://doi.org/10.1080/10739680802220331

Peirce, S. M., Van Gieson, E. J., & Skalak, T. C. (2004). Multicellular simulation predicts microvascular patterning and in silico tissue assembly. *The FASEB Journal : Official Publication of the Federation of American Societies for Experimental Biology*, *18*(6), 731–733. https://doi.org/10.1096/fj.03-0933fje

Pellet-Many, C. (2015). Chemotactic migration of endothelial cells towards VEGF-A165. *Methods in Molecular Biology*, *1332*, 151–157. https://doi.org/10.1007/978-1-4939-2917-7_11

Pettet, G., Byrne, H. M., Mcelwain, D. L. S., & Norbury, J. (1996a). A model of wound-healing angiogenesis in soft tissue. *Mathematical Biosciences*, *136*(1), 35–63. https://doi.org/10.1016/0025-5564(96)00044-2

Pettet, G., Chaplain, M. A. J., McElwain, D. L. S., & Byrne, H. M. (1996b). On the role of angiogenesis in wound healing. *Proceedings of the Royal Society B: Biological Sciences*, *263*(1376), 1487–1493. https://doi.org/10.1098/rspb.1996.0217

Peyroteo, M. M. A., Belinha, J., Vinga, S., Dinis, L. M. J. S., & Jorge, R. M. N. (2018). Mechanical bone remodelling : Comparative study of distinct numerical approaches. *Engineering Analysis with Boundary Elements*, *000*(July 2017), 1–15. https://doi.org/10.1016/j.enganabound.2018.01.011

Phillips, C. M., Lima, E. A. B. F., Woodall, R. T., Brock, A., & Yankeelov, T. E. (2020). A hybrid model of tumor growth and angiogenesis: In silico experiments. *PLoS ONE*, *15*(4), e0231137. https://doi.org/10.1371/journal.pone.0231137

Pillay, S., Byrne, H. M., & Maini, P. K. (2017). Modeling angiogenesis: A discrete to continuum description. *Physical Review E*, *95*(1), 012410. https://doi.org/10.1103/PhysRevE.95.012410

Rabczuk, T., & Zhuang, X. (2018). Meshless Discretization Methods. In *Encyclopedia of Continuum Mechanics* (pp. 1–15). Springer Berlin Heidelberg. https://doi.org/10.1007/978-3-662-53605-6_15-1

Reinke, J. M., & Sorg, H. (2012). Wound repair and regeneration. In *European Surgical Research* (Vol. 49, Issue 1, pp. 35–43). Eur Surg Res. https://doi.org/10.1159/000339613

Rens, E. G., & Edelstein-Keshet, L. (2019). From energy to cellular forces in the Cellular Potts Model: An algorithmic approach. *PLoS Computational Biology*, *15*(12). https://doi.org/10.1371/journal.pcbi.1007459

Ribatti, D. (2010a). The inefficacy of antiangiogenic therapies. In *Journal of Angiogenesis Research* (Vol. 2, Issue 1, p. 27). https://doi.org/10.1186/2040-2384-2-27

Ribatti, D. (2010b). Biomarkers of response to angiogenesis inhibitors: An open and unsolved question. In *European Journal of Cancer* (Vol. 46, Issue 1, pp. 6–8). Elsevier Ltd. https://doi.org/10.1016/j.ejca.2009.10.022

Ribatti, D. (2017). Sales for anti-angiogenic drugs. In *Oncotarget* (Vol. 8, Issue 24, pp. 38080–38081). Impact Journals LLC. https://doi.org/10.18632/oncotarget.17373

Ribatti, D., Annese, T., & Tamma, R. (2020). The use of the chick embryo CAM assay

in the study of angiogenic activiy of biomaterials. In *Microvascular Research* (Vol. 131, p. 104026). Academic Press Inc. https://doi.org/10.1016/j.mvr.2020.104026

Ribatti, D., & Crivellato, E. (2012). "Sprouting angiogenesis", a reappraisal. *Developmental Biology*, *372*(2), 157–165. https://doi.org/10.1016/j.ydbio.2012.09.018

Risau, W. (1997). Mechanisms of angiogenesis. In *Nature* (Vol. 386, Issue 6626, pp. 671–674). https://doi.org/10.1038/386671a0

Risau, Werner, & Flamme, I. (1995). Vasculogenesis. In *Annual Review of Cell and Developmental Biology* (Vol. 11, pp. 73–91). Annual Reviews Inc. https://doi.org/10.1146/annurev.cb.11.110195.000445

Rosales, C., & Uribe-Querol, E. (2017). Phagocytosis: A Fundamental Process in Immunity. In *BioMed Research International* (Vol. 2017). Hindawi Limited. https://doi.org/10.1155/2017/9042851

Roy, S., Biswas, S., Khanna, S., Gordillo, G., Bergdall, V., Green, J., Marsh, C. B., Gould, L. J., & Sen, C. K. (2009). Characterization of a preclinical model of chronic ischemic wound. *Physiological Genomics*, *37*(3), 211–224. https://doi.org/10.1152/physiolgenomics.90362.2008

Ruhrberg, C., Gerhardt, H., Golding, M., Watson, R., Ioannidou, S., Fujisawa, H., Betsholtz, C., & Shima, D. T. (2002). Spatially restricted patterning cues provided by heparin-binding VEGF-A control blood vessel branching morphogenesis. *Genes and Development*, *16*(20), 2684–2698. https://doi.org/10.1101/gad.242002

Saberianpour, S., Heidarzadeh, M., Geranmayeh, M. H., Hosseinkhani, H., Rahbarghazi, R., & Nouri, M. (2018). Tissue engineering strategies for the induction of angiogenesis using biomaterials. In *Journal of Biological Engineering* (Vol. 12, Issue 1, p. 36). BioMed Central Ltd. https://doi.org/10.1186/s13036-018-0133-4

Santulli, G. (2013). Angiogenesis: Insights from a systematic overview. In *Angiogenesis: Insights from a Systematic Overview*.

Saravanan, S., Vimalraj, S., Pavani, K., Nikarika, R., & Sumantran, V. N. (2020). Intussusceptive angiogenesis as a key therapeutic target for cancer therapy. In *Life Sciences* (Vol. 252, p. 117670). Elsevier Inc. https://doi.org/10.1016/j.lfs.2020.117670

Schugart, R. C., Friedman, A., Zhao, R., & Sen, C. K. (2008). Wound angiogenesis as a function of tissue oxygen tension: A mathematical model. *Proceedings of the National Academy of Sciences of the United States of America*, *105*(7), 2628–2633. https://doi.org/10.1073/pnas.0711642105

Scianna, M. (2015). An extended Cellular Potts Model analyzing a wound healing assay. *Computers in Biology and Medicine*, *62*, 33–54. https://doi.org/10.1016/j.compbiomed.2015.04.009

Scianna, M., Bassino, E., & Munaron, L. (2015). A cellular Potts model analyzing differentiated cell behavior during in vivo vascularization of a hypoxic tissue. *Computers in Biology and Medicine*, *63*, 143–156. https://doi.org/10.1016/j.compbiomed.2015.05.020

Serbedzija, G. N., Flynn, E., & Willett, C. E. (1999). Zebrafish angiogenesis: A new model for drug screening. *Angiogenesis*, *3*(4), 353–359. https://doi.org/10.1023/A:1026598300052

Serini, G., Valdembri, D., & Bussolino, F. (2006). Integrins and angiogenesis: A sticky business. In *Experimental Cell Research* (Vol. 312, Issue 5, pp. 651–658). Academic Press Inc. https://doi.org/10.1016/j.yexcr.2005.10.020

Setyawati, M. I., & Leong, D. T. (2017). Mesoporous Silica Nanoparticles as an Antitumoral-Angiogenesis Strategy. *ACS Applied Materials and Interfaces*, *9*(8), 6690–6703. https://doi.org/10.1021/acsami.6b12524

Shamloo, A., Ma, N., Poo, M. M., Sohn, L. L., & Heilshorn, S. C. (2008). Endothelial cell polarization and chemotaxis in a microfluidic device. *Lab on a Chip*, *8*(8), 1292–1299. https://doi.org/10.1039/b719788h

Sherratt, J. A., & Murray, J. D. (1990). Models of epidermal wound healing. *Proceedings of the Royal Society B: Biological Sciences*, *241*(1300), 29–36. https://doi.org/10.1098/rspb.1990.0061

Sherratt, J. A., & Murray, J. D. (1991). Mathematical analysis of a basic model for epidermal wound healing. *Journal of Mathematical Biology*, *29*(5), 389–404. https://doi.org/10.1007/BF00160468

Sherwood, L. M., Parris, E. E., & Folkman, J. (1971). Tumor Angiogenesis: Therapeutic Implications. *New England Journal of Medicine*, *285*(21), 1182–1186.

https://doi.org/10.1056/nejm197111182852108

Shi, X., Zhang, W., Yin, L., Chilian, W. M., Krieger, J., & Zhang, P. (2017). Vascular precursor cells in tissue injury repair. *Translational Research*, *184*, 77–100. https://doi.org/10.1016/j.trsl.2017.02.002

Shibuya, M. (2011). Vascular Endothelial Growth Factor (VEGF) and Its Receptor (VEGFR) Signaling in Angiogenesis: A Crucial Target for Anti- and Pro-Angiogenic Therapies. *Genes and Cancer*, *2*(12), 1097–1105. https://doi.org/10.1177/1947601911423031

Shiu, Y. T., Weiss, J. A., Hoying, J. B., Iwamoto, M. N., Joung, I. S., & Quam, C. T. (2005). The role of mechanical stresses in angiogenesis. In *Critical Reviews in Biomedical Engineering* (Vol. 33, Issue 5, pp. 431–510). Crit Rev Biomed Eng. https://doi.org/10.1615/CritRevBiomedEng.v33.i5.10

Siddique, S., & Chow, J. C. L. (2020). Gold Nanoparticles for Drug Delivery and Cancer Therapy. *Applied Sciences*, *10*(11), 3824. https://doi.org/10.3390/app10113824

Singer, A. J., & Clark, R. A. F. (1999). Cutaneous Wound Healing. *New England Journal of Medicine*, *341*(10), 738–746. https://doi.org/10.1056/NEJM199909023411006

Siracusa, M. C., Kim, B. S., Spergel, J. M., & Artis, D. (2013). Basophils and allergic inflammation. In *Journal of Allergy and Clinical Immunology* (Vol. 132, Issue 4, pp. 789–801). Mosby Inc. https://doi.org/10.1016/j.jaci.2013.07.046

Sleeman, B., & Wallis, I. P. (2002). Tumour induced angiogenesis as a reinforced random walk: Modelling capillary network formation without endothelial cell proliferation. *Mathematical and Computer Modelling*, *36*(3), 339–358. https://doi.org/10.1016/S0895-7177(02)00129-2

Song, H., Wang, W., Zhao, P., Qi, Z., & Zhao, S. (2014). Cuprous oxide nanoparticles inhibit angiogenesis via down regulation of VEGFR2 expression. *Nanoscale*, *6*(6), 3206–3216. https://doi.org/10.1039/c3nr04363k

Staton, C. A., Stribbling, S. M., Tazzyman, S., Hughes, R., Brown, N. J., & Lewis, C. E. (2004). Current methods for assaying angiogenesis in vitro and in vivo. In *International Journal of Experimental Pathology* (Vol. 85, Issue 5, pp. 233–248). https://doi.org/10.1111/j.0959-9673.2004.00396.x

Stokes, C. L., Lauffenburger, D. A., & Williams, S. K. (1991). Migration of individual

microvessel endothelial cells: Stochastic model and parameter measurement. *Journal of Cell Science*, *99*(2), 419–430. https://pubmed.ncbi.nlm.nih.gov/1885678/

Stokes, Cynthia L., & Lauffenburger, D. A. (1991). Analysis of the roles of microvessel endothelial cell random motility and chemotaxis in angiogenesis. *Journal of Theoretical Biology*, *152*(3), 377–403. https://doi.org/10.1016/S0022-5193(05)80201-2

Sundberg, C., Nagy, J. A., Brown, L. F., Feng, D., Eckelhoefer, I. A., Manseau, E. J., Dvorak, A. M., & Dvorak, H. F. (2001). Animal Model: Glomeruloid microvascular proliferation follows adenoviral vascular permeability factor/vascular endothelial growth factor-164 gene delivery. *American Journal of Pathology*, *158*(3), 1145–1160. https://doi.org/10.1016/S0002-9440(10)64062-X

Tal, T., Kilty, C., Smith, A., LaLone, C., Kennedy, B., Tennant, A., McCollum, C. W., Bondesson, M., Knudsen, T., Padilla, S., & Kleinstreuer, N. (2017). Screening for angiogenic inhibitors in zebrafish to evaluate a predictive model for developmental vascular toxicity. *Reproductive Toxicology*, *70*, 70–81. https://doi.org/10.1016/j.reprotox.2016.12.004

Tammela, T., Zarkada, G., Wallgard, E., Murtomäki, A., Suchting, S., Wirzenius, M., Waltari, M., Hellström, M., Schomber, T., Peltonen, R., Freitas, C., Duarte, A., Isoniemi, H., Laakkonen, P., Christofori, G., Ylä-Herttuala, S., Shibuya, M., Pytowski, B., Eichmann, A., … Alitalo, K. (2008). Blocking VEGFR-3 suppresses angiogenic sprouting and vascular network formation. *Nature*, *454*(7204), 656–660. https://doi.org/10.1038/nature07083

Tigner, A., Ibrahim, S. A., & Murray, I. (2020). Histology, White Blood Cell. In *StatPearls*. StatPearls Publishing. http://www.ncbi.nlm.nih.gov/pubmed/33085295

Tissue Engineering Market Size, Industry Analysis Report. (2020). https://www.bccresearch.com/market-research/healthcare/tissue-regeneration-techs-markets-report.html

Tober, J., Koniski, A., McGrath, K. E., Vemishetti, R., Emerson, R., De Mesy-Bentley, K. K. L., Waugh, R., & Palis, J. (2007). The megakaryocyte lineage originates from hemangioblast precursors and is an integral component both of primitive and of definitive hematopoiesis. *Blood*, *109*(4), 1433–1441. https://doi.org/10.1182/blood-2006-06-031898

Travasso, R. D. M., Poiré, E. C., Castro, M., Rodrguez-Manzaneque, J. C., & Hernández-Machado, A. (2011). Tumor angiogenesis and vascular patterning: A mathematical model. *PLoS ONE*, *6*(5), e19989. https://doi.org/10.1371/journal.pone.0019989

Valero, C., Javierre, E., García-Aznar, J. M., & Gómez-Benito, M. J. (2013). Numerical modelling of the angiogenesis process in wound contraction. *Biomechanics and Modeling in Mechanobiology*, *12*(2), 349–360. https://doi.org/10.1007/s10237-012-0403-x

Van Hinsbergh, V. W. M., & Koolwijk, P. (2008). Endothelial sprouting and angiogenesis: Matrix metalloproteinases in the lead. In *Cardiovascular Research* (Vol. 78, Issue 2, pp. 203–212). Cardiovasc Res. https://doi.org/10.1093/cvr/cvm102

Vascular Endothelial Growth Factor (VEGF) Inhibitors Market Size Worth $10.2 Billion by 2023 - Technavio | Business Wire. (n.d.). Retrieved January 30, 2021, from https://www.businesswire.com/news/home/20190708005077/en/Vascular-Endothelial-Growth-Factor-VEGF-Inhibitors-Market-Size-Worth-10.2-Billion-by-2023---Technavio

Vermolen, F. J., & Javierre, E. (2012). A finite-element model for healing of cutaneous wounds combining contraction, angiogenesis and closure. *Journal of Mathematical Biology*, *65*(5), 967–996. https://doi.org/10.1007/s00285-011-0487-4

Vilanova, G., Burés, M., Colominas, I., & Gomez, H. (2018). Computational modelling suggests complex interactions between interstitial flow and tumour angiogenesis. *Journal of the Royal Society Interface*, *15*(146). https://doi.org/10.1098/rsif.2018.0415

Vilanova, G., Colominas, I., & Gomez, H. (2014). Coupling of discrete random walks and continuous modeling for three-dimensional tumor-induced angiogenesis. *Computational Mechanics*, *53*(3), 449–464. https://doi.org/10.1007/s00466-013-0958-0

Vilanova, G., Colominas, I., & Gomez, H. (2017a). A mathematical model of tumour angiogenesis: Growth, regression and regrowth. *Journal of the Royal Society Interface*, *14*(126). https://doi.org/10.1098/rsif.2016.0918

Vilanova, G., Colominas, I., & Gomez, H. (2017b). Computational Modeling of Tumor-

Induced Angiogenesis. *Archives of Computational Methods in Engineering*, *24*(4), 1071–1102. https://doi.org/10.1007/s11831-016-9199-7

Vines, J. B., Yoon, J. H., Ryu, N. E., Lim, D. J., & Park, H. (2019). Gold nanoparticles for photothermal cancer therapy. In *Frontiers in Chemistry* (Vol. 7, Issue APR, p. 167). Frontiers Media S.A. https://doi.org/10.3389/fchem.2019.00167

Vlăsceanu, G. M., Marin, Ş., Ţiplea, R. E., Bucur, I. R., Lemnaru, M., Marin, M. M., Grumezescu, A. M., & Andronescu, E. (2016). Silver nanoparticles in cancer therapy. In *Nanobiomaterials in Cancer Therapy: Applications of Nanobiomaterials* (pp. 29–56). Elsevier Inc. https://doi.org/10.1016/B978-0-323-42863-7.00002-5

Wallace, H. A., & Zito, P. M. (2019). Wound Healing Phases. In *StatPearls*. StatPearls Publishing. http://www.ncbi.nlm.nih.gov/pubmed/29262065

Wang, H., Yang, Z., Jiang, Y., Flannery, J., Hammond, S., Kafri, T., Vemuri, S. K., Jones, B., & Hartnett, M. E. (2014). Quantitative analyses of retinal vascular area and density after different methods to reduce VEGF in a rat model of retinopathy of prematurity. *Investigative Ophthalmology and Visual Science*, *55*(2), 737–744. https://doi.org/10.1167/iovs.13-13429

Wang, J. G., & Liu, G. R. (2002). A point interpolation meshless method based on radial basis functions. *International Journal for Numerical Methods in Engineering*, *54*(11), 1623–1648. https://doi.org/10.1002/nme.489

Wang, J., Zhang, L., Jing, C., Ye, G., Wu, H., Miao, H., Wu, Y., & Zhou, X. (2013). Multi-scale agent-based modeling on melanoma and its related angiogenesis analysis. *Theoretical Biology and Medical Modelling*, *10*(1). https://doi.org/10.1186/1742-4682-10-41

Wang, Yangyang, Guerrero-Juarez, C. F., Qiu, Y., Du, H., Chen, W., Figueroa, S., Plikus, M. V., & Nie, Q. (2019). A multiscale hybrid mathematical model of epidermal-dermal interactions during skin wound healing. *Experimental Dermatology*, *28*(4), 493–502. https://doi.org/10.1111/exd.13909

Wang, Yu, Chen, C. L., & Iijima, M. (2011). Signaling mechanisms for chemotaxis. In *Development Growth and Differentiation* (Vol. 53, Issue 4, pp. 495–502). NIH Public Access. https://doi.org/10.1111/j.1440-169X.2011.01265.x

Watari, K., Shibata, T., Fujita, H., Shinoda, A., Murakami, Y., Abe, H., Kawahara, A.,

Ito, H., Akiba, J., Yoshida, S., Kuwano, M., & Ono, M. (2020). NDRG1 activates VEGF-A-induced angiogenesis through PLCγ1/ERK signaling in mouse vascular endothelial cells. *Communications Biology*, *3*(1). https://doi.org/10.1038/s42003-020-0829-0

Xue, C., Friedman, A., & Sen, C. K. (2009). A mathematical model of ischemic cutaneous wounds. *Proceedings of the National Academy of Sciences of the United States of America*, *106*(39), 16782–16787. https://doi.org/10.1073/pnas.0909115106

Yang, J. P., Liu, H. J., & Liu, X. F. (2010). VEGF promotes angiogenesis and functional recovery in stroke rats. *Journal of Investigative Surgery*, *23*(3), 149–155. https://doi.org/10.3109/08941930903469482

Yonekura, K., Basaki, Y., Chikahisa, L., Okabe, S., Hashimoto, A., Miyadera, K., Wierzba, K., & Yamada, Y. (1999). UFT and Its Metabolites Inhibit the Angiogenesis Induced by Murine Renal Cell Carcinoma, as Determined by a Dorsal Air Sac Assay in Mice. *Clinical Cancer Research*, *5*(8).

Yoshida, A., Anand-Apte, B., & Zetter, B. R. (1996). Differential Endothelial Migration Proliferation to Basic Fibroblast Growth Factor and Vascular Endothelial Growth Factor. *Growth Factors*, *13*(1–2), 57–64. https://doi.org/10.3109/08977199609034566

Zhang, Y., Li, M., Gao, X., Chen, Y., & Liu, T. (2019). Nanotechnology in cancer diagnosis: Progress, challenges and opportunities. In *Journal of Hematology and Oncology* (Vol. 12, Issue 1, p. 137). BioMed Central Ltd. https://doi.org/10.1186/s13045-019-0833-3